IMAGING MICROSEISMIC EVENTS AND SEISMIC ANISOTROPY FROM SHEAR-WAVE SPLITTING ANALYSIS

A Dissertation Presented to

The Faculty of the Department of Earth and Atmospheric Sciences

University of Houston

In Partial Fulfillment

of the Requirements for the Degree

Doctor of Philosophy

By

Duo Yuan

May 2016

IMAGING MICROSEISMIC EVENTS AND SEISMIC ANISOTROPY FROM SHEAR-WAVE SPLITTING ANALYSIS

Duo Yuan

APPROVED:

Dr. Aibing Li, Supervisor
Department of Earth and Atmospheric Sciences

Dr. Robert Stewart
Department of Earth and Atmospheric Sciences

Dr. Yingcai Zheng
Department of Earth and Atmospheric Sciences

Dr. Rongmao Zhou
BHP Billiton

Dean, College of Natural Sciences and Mathematics

ACKNOWLEDGEMENTS

My special thanks go to my advisor, Dr. Aibing Li, for her guidance, caring and support throughout my Ph.D. study and research. Without her continuous support, I would not have been able to complete this dissertation. I also want to thank Dr. Robert Stewart, Dr. Yingcai Zheng, and Dr. Rongmao Zhou for their useful comments and suggestions.

We thank Hess Corporation for allowing us to use very valuable data in the Bakken formation. We are grateful to Michele Simon and other people from the Bakken team in Hess Corporation for their useful comments, suggestions and encouragements.

Finally, I thank my friend, Zhao Li, for providing me numerous very useful technical suggestions. And most importantly, I thank my wife, and my parents for their support during my Ph.D. study.

IMAGING MICROSEISMIC EVENTS AND SEISMIC ANISOTROPY FROM SHEAR-WAVE SPLITTING ANALYSIS

An Abstract of a Dissertation

Presented to

the Faculty of the Department of Earth and Atmospheric Sciences

University of Houston

In Partial Fulfillment

of the Requirements for the Degree

Doctor of Philosophy

By

Duo Yuan

May 2016

ABSTRACT

Microseismic imaging has become a useful tool in monitoring and analyzing fractures generated by hydraulic-fracturing stimulation in unconventional reservoirs. Although this technology has become more mature, there are still challenges in the processing of downhole microseismic data. First, intrinsic anisotropic reservoir rock-like-shale stacked with man-made fractures resulted in more complicated anisotropy than seen in more commonly used vertical transverse isotropy (VTI). However, a more accurate low-symmetry anisotropic model cannot be constrained from conventional P and fast S-wave travel times alone due to relatively sparse ray coverage. Second, for single monitoring well, event azimuths, which are obtained by a P-wave hodogram, must be added to data to determine event locations. However, typical weak P-wave arrivals usually cause heavy azimuth measurement uncertainties. To address these issues, we introduced new data, full S-wave-splitting parameters (delay time of the slow S-wave and fast S-wave polarization direction), to improve velocity models and microseismic locations.

To solve the first problem, instead of assuming a higher-symmetry anisotropic model, we attempted to add S-wave splitting data, which is very helpful to constrain anisotropy. A Genetic Algorithm (GA) inversion was adopted to simultaneously determine event locations and stiffness coefficients of anisotropic media. We applied this approach to synthetic waveforms and successfully recovered the input event locations and velocity model. The effectiveness of this method is further demonstrated from real microseismic data acquired in the Bakken shale reservoir. The determined microseismic events are

aligned in E15N direction, which agrees with the azimuth of the fast symmetric axis in the resulting anisotropic model in the area.

Another study in this dissertation is the development of a new method of determining microseismic event azimuths using S-wave splitting analysis. This approach is based the positive correlation between the effectiveness of S-wave splitting measurements and the accuracy of the event azimuth. We applied a grid search to find the optimal azimuth. The obtained event azimuths agree well with the input ones in the synthetic experiments and with those determined from clear P wave particle motions in the field data tests.

In summary, S-wave splitting data contain valuable information about seismic anisotropy and were significantly useful in resolving the velocity model and locating microseismic events. To the best of our knowledge, this dissertation is the first study using full S-wave splitting parameters in microseismic imaging. We have demonstrated the success of our new methods using synthetic and field data and envision their broad application in the future.

CONTENTS

LIST of TABLES

LIST of FIGURES

1 Chapter 1

Introduction

1.1 Background

Hydraulic fracturing is a standard technique for unconventional reservoir exploitation to achieve economical hydrocarbon production. High-pressure fluid injection helps generate fracture networks and enhances permeability. Specific engineering questions about the geometry of generated fractures, including fracture orientation and height and length away from the well in each direction, need to be answered to validate and optimize hydraulic fracturing design, well-completion, and well-design. More importantly, stimulated-rock volume (SRV), a reliable parameter for evaluating hydraulic fracturing and predicting production rates for an unconventional reservoir, is required to understand fracture networks in detail. Microseismic imaging is critical for obtaining essential fracture geometry information and SRV.

When high-pressure fluid is injected into a reservoir, the increased pore-pressure reduces the effective stress across a preexisting fault and causes the friction resistance to decrease and the slips triggered on these faults can cause tiny earthquakes with magnitudes from -3 to -1, named microseismic events. Microseismic studies mainly rely on the locations and source mechanisms of microseismic events to understand how a formation is fractured. Hydraulic fracturing is a continuous process that usually lasts several days and microseismic data acquisition usually involves continuous passive

seismic monitoring. Seismometers or geophones are deployed either in vertical observation wells (downhole data) or on the surface (surface data) (Figure 1.1). Downhole data exhibit better signal-to-noise ratios (SNR) and narrow seismic ray-coverage while surface data are characterized by better seismic ray-coverage and lower SNR.

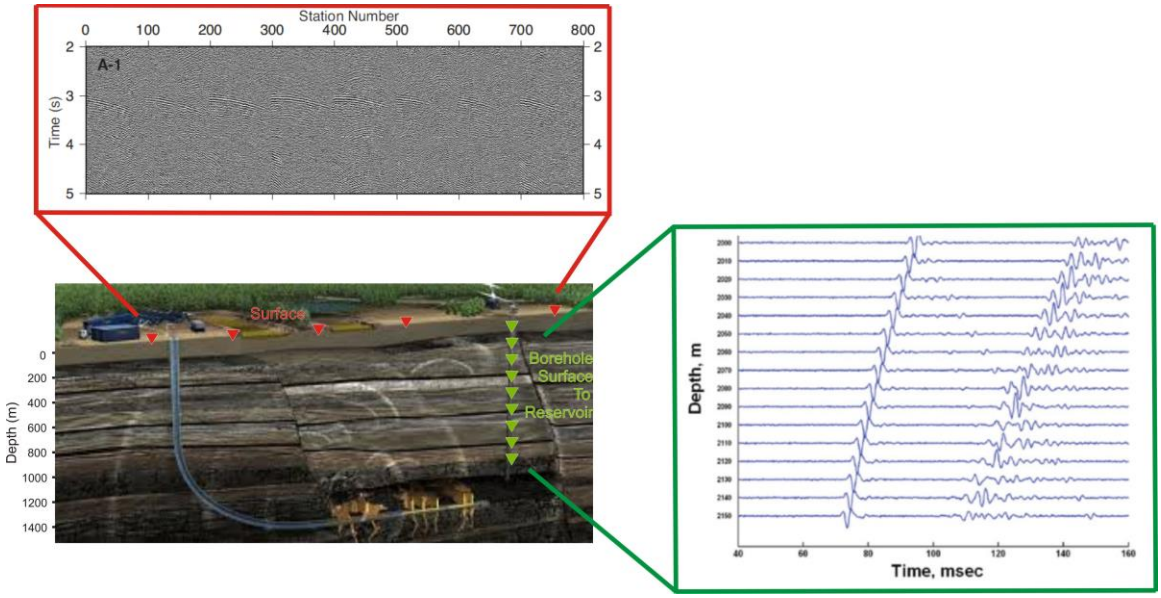

Figure 1.1: Example of various arrays used in microseismic studies. Microseismic event signals can be recorded either by a vertical array in a borehole (green box on right) or by surface array (red box at top) (Maxwell *et al*., 2012).

Locating microseismic events is the primary task in microseismic monitoring because the locations are used to infer the shapes and orientations of hydraulic fractures. Numerous studies have discussed various techniques for determining event locations. Generally, the methods can be grouped in two categories. One approach is locating events from travel times of identified seismic arrivals based on ray theory (e.g. Geiger, 1912; Waldhauser and Ellsworth, 2000; Gambino *et al*., 2004; Chambers *et al*., 2010); the other is obtaining event locations though migration of recoded waveforms (e.g. Gajewski and Tessmer, 2005; Gharti *et al*., 2010; Haldorsen *et al*., 2013). The results from these different methods generally agree for a given velocity model. The error of the velocity model is the most elusive contributor to the uncertainty of event locations.

Obtaining an accurate velocity model remains challenging. Most unconventional oil reservoirs are in shale rocks, which exhibit intrinsic seismic anisotropy (Vernik and Liu, 1997). In-situ anisotropic medium superimposed by man-made fractures makes the most common VTI (transversely isotropic with a vertical symmetry axis) medium is unsuitable for microseismic studies (Grechka *et al*., 2014). A low-symmetry anisotropic velocity model is needed to describe fractured formations. Time-lapse variations of the velocity model (Eisner *et al*., 2011; Grechka *et al*., 2011a), which can be explained by multi-stages hydraulic fracturing generates man-made fractures resulting in altered anisotropic properties of reservoir rock between different stages. This complex anisotropy, if not accounted for in the velocity model, can strongly affect the accuracy of event locations.

1.2 Motivation

A routine approach of velocity model building from microseismic data is through the inversion of travel times from perforation shots (e.g. Warpinski *et al*., 2005; Pei *et al*., 2009). In this case, the locations of sources and receivers are known. So the forward problem is the classic two-point ray tracing (e.g. Wesson, 1971; Kim and Baag, 2002), and travel time data can be directly inverted to obtain velocity model using either the least-squares inversion or an optimization method (Figure 1.2). One of the major limitations of using perforation shots is that ray coverage is typically narrow. Energy emitted from microseismic events usually does not pass through regions illuminated by perforation shots. Such a narrow ray aperture is incapable of fully constraining seismic anisotropy (Grechka and Duchkov, 2011). In addition, as mentioned above, that velocity will change after perforation shots due to newly induced fractures. Ideally, the velocity model should be continuously calibrated during the fracturing simulation.

Mainly two groups of approaches are used to account for velocity effects on microseismic event locations. The first group is relative locating of microseismicity (e.g. Waldhauser and Ellsworth, 2000; Waldhauser, 2001; Got and Okubo, 2003; Grechka *et al*., 2015). This approach aims to reduce the influence of velocity models by finding event locations relative to the perforation shots and previously located events. The other group, which is more popular for downhole data, utilizes microseismic events as the source of information for refining a velocity model (e.g. Zhang *et al*., 2009; Jansky *et al*., 2010; Zhou *et al*., 2010; Grechka *et al.*, 2011; Grechka and Yaskevich, 2013, 2014; Li *et*

al., 2013, 2014). This group aims to obtain low symmetry anisotropic velocity models based on wide ray apertures provided by microseismic events. Then, event locations will be updated using the refined velocity model.

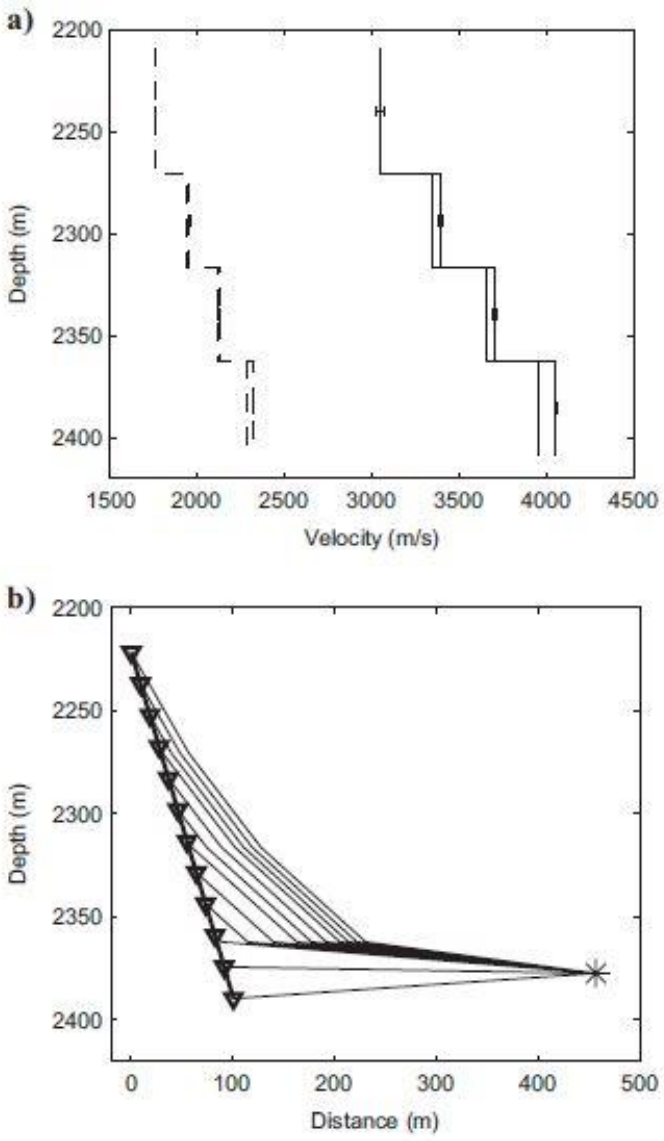

Figure 1.2: Example of velocity calibration for microseismic monitoring. (a) Inverted velocity model (solid, thin lines for P-wave; dashed for S-wave) against the true synthetic models. (b) Geometry of the source, receivers, and ray paths (Pei *et al*., 2009).

In the second type of approach, velocities are considered as model parameters instead of *a priori* knowledge assumed by conventional methods. This inverse problem is solved by linearized least-squares inversion in previous studies. The number of model parameters depends on the symmetry of anisotropy. The difficulty of this method lies in the calculation of Frechet derivative matrix

$$\mathbf{F} = \{\frac{\partial t_i}{\partial C_{ij}}, \frac{\partial t_i}{\partial \boldsymbol{x}_n}, \frac{\partial t_i}{\partial \boldsymbol{y}_n}, \frac{\partial t_i}{\partial \boldsymbol{z}_n}, \frac{\partial t_i}{\partial \boldsymbol{\tau}_n}\} \tag{1.1}$$

Here t_i is available P-wave and/or S-wave travel times, C_{ij} is stiffness coefficients, $\boldsymbol{x}_n$, $\boldsymbol{y}_n$ and $\boldsymbol{z}_n$ represent event locations, and $\boldsymbol{\tau}_n$ is the origin time. This matrix was solved by Grechka and Duchkov (2011) analytically (Appendix A).

It is still difficult to constrain the large number of stiffness coefficients for low-symmetry anisotropy even many microseismic data are included due to the common narrow ray coverage in downhole monitoring. For example, if we expand the linearized non-linear inversion with the form $\Delta d = G\Delta m$ with a VTI type medium (Equation 1.2), where G is the Frechet matrix and i and n represent the number of travel time data and events, respectively. If ray coverage mainly focuses on East-West direction, only $\frac{\partial t_i}{\partial c_{11}}$ and $\frac{\partial t_i}{\partial c_{66}}$ have large values and the variation of other Δm except ΔC_{11} and ΔC_{66} will not affect Δd. Consequently, only C_{11} and C_{66} can be constrained in this case.

$$\begin{vmatrix} \Delta t_1 \\ \cdot \\ \cdot \\ \cdot \\ \Delta t_i \end{vmatrix} = \begin{vmatrix} \frac{\partial t_1}{\partial C_{11}} & \frac{\partial t_1}{\partial C_{13}} & \frac{\partial t_1}{\partial C_{33}} & \frac{\partial t_1}{\partial C_{44}} & \frac{\partial t_1}{\partial C_{66}} & \frac{\partial t_1}{\partial x_n} & \frac{\partial t_1}{\partial y_n} & \frac{\partial t_1}{\partial z_n} & \frac{\partial t_1}{\partial \tau_n} \\ & & & & \cdot & & & & \\ & & & & \cdot & & & & \\ & & & & \cdot & & & & \\ \frac{\partial t_i}{\partial C_{11}} & \frac{\partial t_i}{\partial C_{13}} & \frac{\partial t_i}{\partial C_{33}} & \frac{\partial t_i}{\partial C_{44}} & \frac{\partial t_i}{\partial C_{66}} & \frac{\partial t_i}{\partial x_n} & \frac{\partial t_i}{\partial y_n} & \frac{\partial t_i}{\partial z_n} & \frac{\partial t_i}{\partial \tau_n} \end{vmatrix} \begin{vmatrix} \Delta C_{11} \\ \Delta C_{13} \\ \Delta C_{33} \\ \Delta C_{44} \\ \Delta C_{66} \\ \Delta x_n \\ \Delta y_n \\ \Delta z_n \\ \Delta \tau_n \end{vmatrix} \quad (1.2)$$

Grechka and Yaskevich (2013) addressed this problem by singular value decomposition (SVD) analysis of the Frechet matrix (Figure 1.3)

$$\mathbf{F} = \mathbf{usw}^T \quad (1.3)$$

where **u** is a column-orthogonal matrix, **s** is a diagonal matrix whose elements are the singular values, and $\mathbf{w}^T$ is the transpose of an orthogonal eigenvector matrix. A condition number

$$k = \frac{\max s}{\min s} \quad (1.4)$$

is used to gain a quick insight into whether a given data set can constrain all model parameters. If low symmetry anisotropic media such as triclinic cannot be recovered, a higher symmetry has to be assumed. However, this simplified velocity model will increase data misfits and decrease the accuracy of event locations.

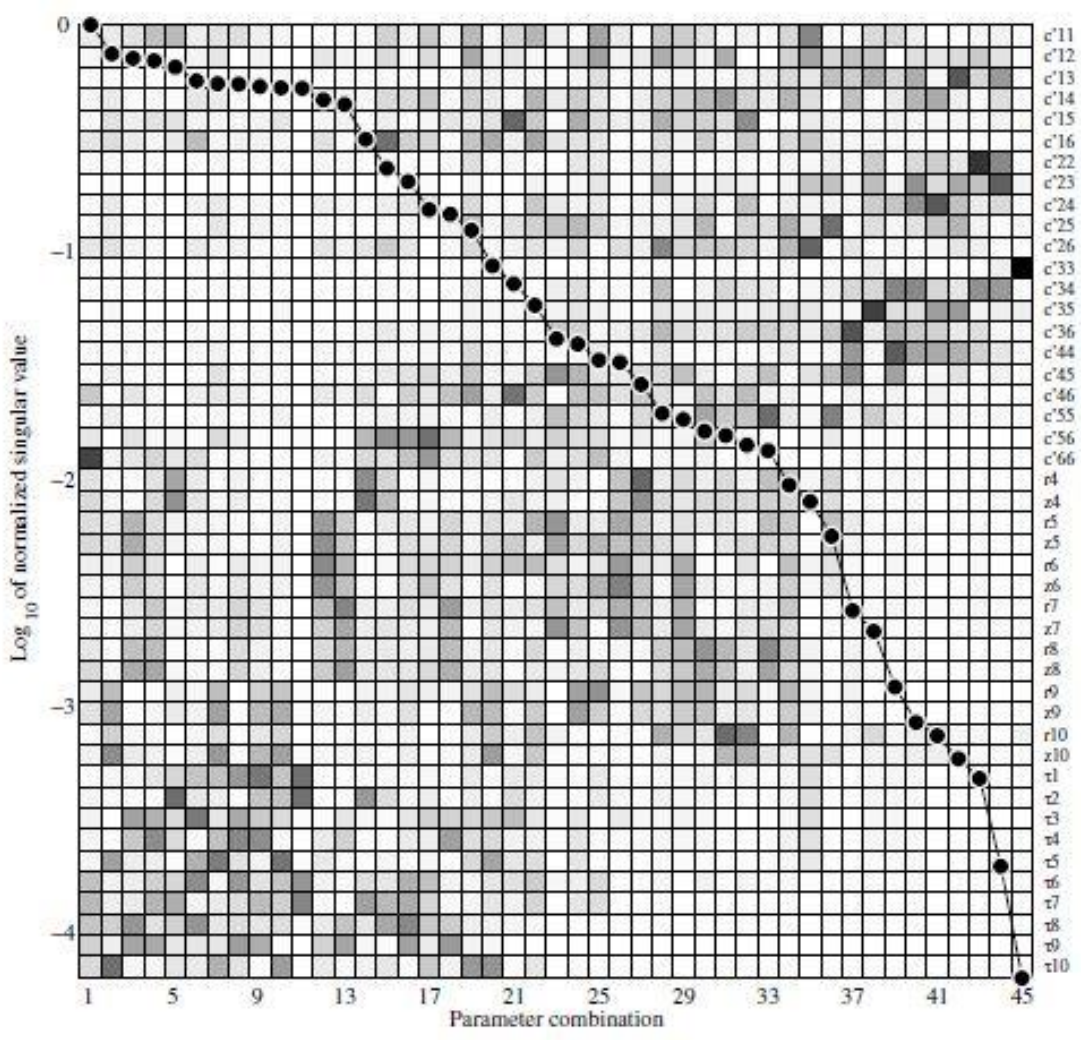

Figure 1.3: Example of SVD analysis of the Frechet matrix. Logarithms of normalized singular values, s, (dots) of the Frechet matrix overlaying the absolute values of elements of the eigenvector matrix, **w,** (gray squares) (Grechka *et al*., 2011).

Besides velocity model, event azimuth determination also affects the locations of microseismic events especially for one-well monitoring. In this case, event locations cannot be fully determined by travel times of direct arrivals. P-wave polarization information is typically used to estimate event azimuths to pinpoint the locations (Grechka *et al.*, 2011). P-wave polarization analysis, also named as P-wave hodogram, is

susceptible to signal strength and noise level. Weak P-Wave signals, which are very common in microseismic data due to fracturing mechanism (Maxwell *et al*., 2010), bring large uncertainties to event azimuths determination. These ill-determined azimuths can cause significant bias and mislocations of microseismic events.

1.3 Objectives and outline

This dissertation aims to address the challenges in velocity model building and event azimuth determination from a new perspective. The main strategy is adopting a new type of data, S-wave splitting parameters (delay time of slow S-wave and fast S-wave polarization direction) from microseismic data. S-wave splitting is a direct indication for seismic anisotropy and the splitting parameters help to constrain anisotropic velocity models. In addition, the effectiveness of S-wave splitting measurements correlates with the accuracy of event azimuths, and this correlation can be used to find the best event azimuth.

In Chapter 2, we introduced full S-wave splitting parameters to the traditional data set of P- and S-wave arrivals to determine anisotropic velocity models. A Genetic Algorithm (GA) inversion is adopted to solve the locations of events and the stiffness tensor of the anisotropic medium simultaneously. We applied this method to synthetic waveforms from numerical modeling and successfully recovered the input locations and velocity model.

In Chapter 3, we further demonstrated the effectiveness of this method from real microseismic data acquired in the Bakken shale reservoir. Compared with the inversion with an isotropic velocity model, event locations from an anisotropic model become well aligned with natural fractures in the Bakken formation. Our experiments have shown that adding full S-wave splitting parameters makes a significant improvement in constraining a low-symmetry anisotropic model from downhole microseismic data.

In Chapter 4, we present a new method for determining event azimuths using S-wave splitting in microseismic data. This method utilizes the positive correlation between the accuracy of event azimuth and the effectiveness of S-wave splitting measurements. The success of this method is demonstrated through synthetic data.

In Chapter 5, we applied S-wave event azimuth determination method to real microseismic data in the Bakken reservoir. The azimuths from this method are consistent with those form reliable P-wave hodograms and those from more advanced methods. This application suggests that the S-wave method is reliable in determining event azimuths. This method is extremely useful when P-wave data are too weak or noisy to use and helps to improve the number of locatable microseismic events.

2 Chapter 2

Joint inversion for anisotropic velocity model and event locations using S-wave splitting measurements from downhole microseismic data – Methodology and synthetic Test

2.1 Introduction

Hydraulic fracturing is routinely conducted to produce oil and gas from unconventional reservoirs. Microseismic imaging is a powerful tool used to understand generated fracture networks and estimate the stimulated reservoir volume (SRV). The primary task of a microseismic survey is to obtain the locations of microseismic events. Velocity model is a key factor that affects the accuracy of locating events. In conventional practice, a velocity model is usually obtained first from well-logging data and calibrated using perforation-shots (e.g., Maxwell *et al*., 2006; Pei *et al*., 2009). Then the constructed model is used without modification in locating microseismic events. Although this method is routinely used in microseismic imaging, it can be improved because fracturing intrinsic anisotropic rock like shale (e.g., Vernik and Liu, 1997) would generate man-made crack-induced azimuthal anisotropy (Tsvankin and Grechka, 2011). However, narrow ray-path coverage from perforation-shots usually prevents fully constraining a low-symmetry anisotropic model (Grechka and Duchkov, 2011). One important approach to handling this issue is refining the velocity model using wider ray coverage provided by microseismic events.

A few studies have been conducted to derive anisotropic velocity models from microseismic data. Li *et al*. (2013, 2014) extended the double differences method (Waldhauser and Ellsworth, 2000) and conducted a joint inversion of microseismic location and VTI anisotropy. Grechka *et al*. (2011) and Grechka and Yaskevich (2013) used P-wave and fast S-wave travel times to estimate triclinic anisotropy of a medium while determining microseismic locations simultaneously based on Geiger's method (Geiger, 1921). Their studies showed that the anisotropic parameters and event locations can be characterized by conventional P-wave and fast S-wave travel times. However, to resolve a low-symmetry anisotropic model, they emphasized that sufficient polar- and azimuthal-ray coverage is required, which is usually difficult to achieve from downhole microseismic surveys. When ray coverage is not sufficient to constrain low-symmetry triclinic anisotropy, high-symmetry anisotropy has to be considered to reduce model parameters, which could cause location errors. Therefore, the ability to constrain low-symmetry anisotropic models from relatively sparse ray coverage remains a considerable challenge in microseismic studies.

S-wave splitting is a strong indicator of seismic anisotropy. When an S-wave propagates into an anisotropic medium, it splits into two orthogonally polarized waves with different velocities. Anisotropy can be characterized by S-wave splitting parameters, the polarization of the fast S-wave (Φ) and the delay time (δt) between the fast and slow S-wave. The splitting parameters are often determined from an eigenvalue minimization method by Silver and Chan (1991), which has been widely applied in global seismology to study azimuthal anisotropy caused by lithospheric fabric and mantle flow (Li and

Detrick, 2003; Li and Chen, 2006; Fu *et al*., 2013). S-wave splitting analysis was also conducted by Harrison (1992) from surface-seismic data to improve multi-component converted wave processing. In microseismic studies, Teanby *et al*. (2004) showed that full S-wave-splitting parameters could be measured successfully from microseismic data. Verdon *et al*. (2009) and Verdon and Kendall (2011) used measured S-wave-splitting parameters and rock-physics modeling to interpret fractures sets. To our knowledge, measured S-wave-splitting parameters (Φ, δt) have not been used in microseismic velocity model building although Grechka *et al*. (2014) included picked fast and slow S-wave arrival times in their study. They concluded that adding slow S-wave arrival times is essential in determining low-symmetry anisotropy.

In this chapter, we measured full S-wave-splitting parameters from microseismic data and used P-wave, split S-waves arrivals and Φ in a joint inversion for an effective anisotropic-velocity model and event locations. A Genetic Algorithm optimization method is adopted to solve event locations and effective anisotropic medium simultaneously. Experiments from synthetic microseismic data show that adding slow S-wave arrivals and Φ can better constrain low-symmetry anisotropic models.

2.2 Data analysis and preparation

Data used in this study include picked P-wave, fast S-wave-arrival times, and measured S-wave-splitting parameters (Φ and δt). Since splitting parameters are new addition to traditional microseismic data, details on how they are measured are described below.

S-wave-splitting parameters are measured following the eigenvalue minimization method proposed by Silver and Chan (1991). This method is originally designed for global seismology and uses the two horizontal components in constraining the splitting parameters for a near-vertical ray path beneath a receiver. However, S-wave ray paths of downhole microseismic data usually present strong inclinations. In this case, the fast-polarized S-wave is not dominantly on the horizontal components, which are not effective in finding the splitting parameters. Therefore, the original north (N), east (E), and vertical (Z) components in the geographical coordinate system have to be rotated to the components in a ray-frame coordinate system (Figure 2.1), in which three axes consist of the P-wave polarization (L), transverse (T), and radial direction (Q) (Wuestefeld *et al.*, 2010). Φ is defined as the angle between the fast direction and Q direction in the ray-frame coordinates (Figure 2.1). The rotation uses the following transformation matrix to change geographical coordinates to ray-frame coordinates (Plesinger *et al.*, 1986).

$$M_{3D} = \begin{bmatrix} \cos(I) & -\sin(I)\sin(\theta) & -\sin(I)\cos(\theta) \\ \sin(I) & \cos(I)\sin(\theta) & \cos(I)\cos(\theta) \\ 0 & -\cos(\theta) & \sin(\theta) \end{bmatrix} \tag{2.1}$$

Where I is the incidence angle of the ray and θ is the backazimuth of the event. These angles are obtained from P-wave hodogram analysis (Verdon *et al*., 2009). Then the windowed traces of Z, E, and N components are rotated to three components in L, Q, and, T in the ray frame using Equation 2.2.

$$\begin{bmatrix} L \\ Q \\ T \end{bmatrix} = M_{3D} \begin{bmatrix} Z \\ E \\ N \end{bmatrix} \tag{2.2}$$

S-wave-splitting parameters can be measured from the Q and T components following the method of Silver and Chan (1991). A grid search is used to find the optimal splitting parameters. For each pair of (Φ, δt), a cross correlation matrix from Q and T components (Equation 2.3) is obtained from S waveforms and two eigenvalues of the matrix are calculated.

$$\begin{bmatrix} C_{QQ} & C_{QT} \\ C_{TQ} & C_{TT} \end{bmatrix} \tag{2.3}$$

At the true value of (Φ, δt), the cross-correlation matrix resembles an isotropic case, in which the matrix has one zero eigenvalue and is defined as singular. Due to the existence of noise, the pair of Φ and δt that can minimize the second eigenvalue λ_2 of the cross-correlation matrix is considered to be the optimized result. The variation of λ_2 can be

used to estimate the standard errors of the splitting parameters (Φ, δt), which are important in forming the objective function of inversions as described in next section.

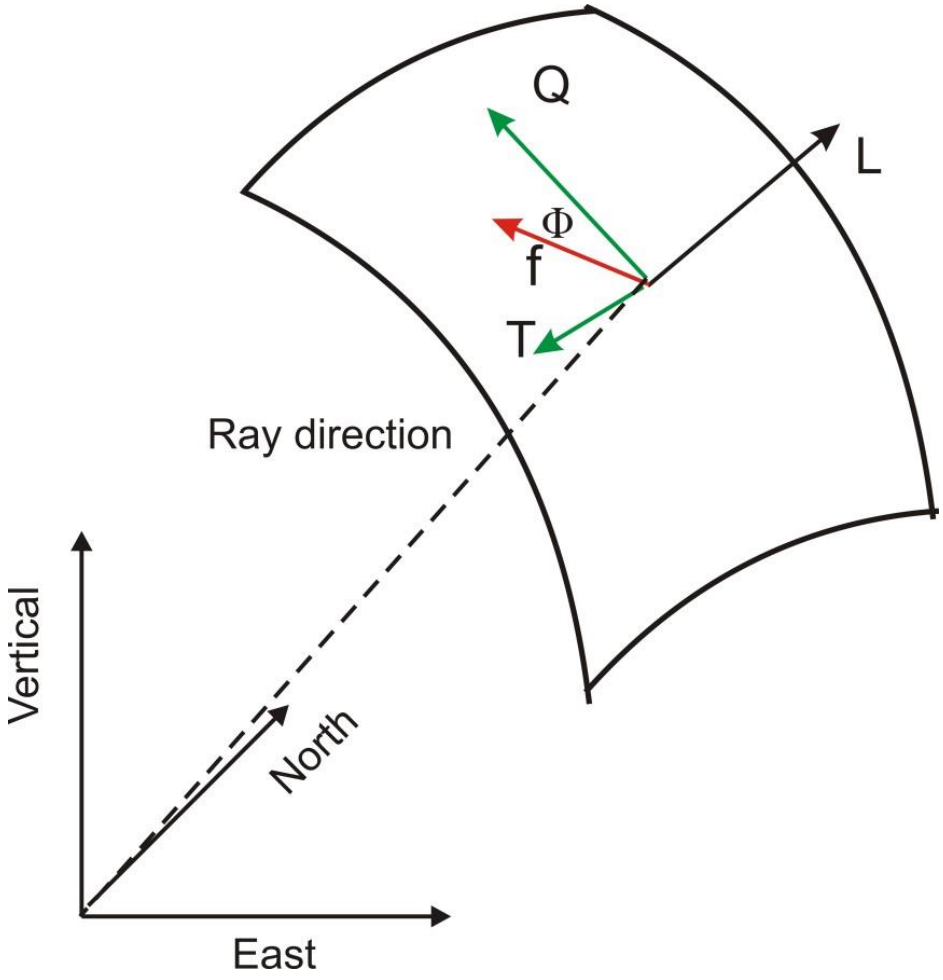

Figure 2.1: Geometry of geographical coordinates and ray coordinates. Three positive axes in the ray-coordinate system are the wavefront normal (L), transverse (T), and radial (Q) direction. The red lines represents fast S-wave polarization in the T-Q plane. ϕ is the angle of fast direction, which is measured relative to the radial direction (Q).

2.3 Method

All data used in the study can be expressed as

$$\mathbf{d} = [t_e(\boldsymbol{x}_g), \Phi_e(\boldsymbol{x}_g)] \tag{2.4}$$

where t_e is arrival times of three kinds of waves (P-wave, fast S-wave, and slow S-wave) and Φ_e is the fast S-wave polarization angle from the e-th event (e=1, 2, …N_e). Slow S-wave arrivals are computed from the picked fast S-wave arrivals and delay times (δt) from S-wave splitting parameters. $\boldsymbol{x}_g$ is the location of the g-th receivers ($g = 1,\ldots, N_g$). The size of d is usually much smaller than $4N_eN_g$ due to the noise contamination.

The models parameters are

$$\mathbf{m} = [\boldsymbol{C}_{ijkl}, \boldsymbol{\xi}_e] \tag{2.5}$$

where $\boldsymbol{C}_{ijkl}$ is density normalized stiffness coefficients that describes the effective anisotropic model and $\boldsymbol{x}_e$ (e=1,…, N_e) are event locations. Numerous ray tracing techniques are available to forward model $\mathbf{d}$ under given $\mathbf{m}$ (e.g. Thurber and Ellsworth, 1980; Kim and Baag, 2002), this study modifies Sharma's ray-tracing method (Sharma, 2002) for forward calculations.

The inversion from polarization data to an anisotropic model and event locations is significantly non-linear. Considering the challenge of calculating Frechet derivatives $[\partial\Phi / \partial\mathbf{m}]$ analytically, we adopt a global optimization method, the Genetic Algorithm

(GA) inversion, to find the best-fitting model parameters. Genetic Algorithms are a direct, parallel, stochastic method for global optimization, which imitates the evolution of living beings. This method has been used successfully to solve inverse problems in the area of exploration geophysics (Padhi and Mallick, 2013). The optimal model parameters are obtained by minimizing the following objective function.

$$obj(\mathbf{m}) = \frac{1}{M}\sum_{i=1}^{M}\left(\frac{\tau_i - \bar{\tau}_i^{cal}}{\sigma_{ti}}\right)^2 + \frac{1}{N}\sum_{j=1}^{N}\left(\frac{\Phi_j - \Phi_j^{cal}}{\sigma_{\Phi j}}\right)^2 \quad (2.6)$$

where M is the total number of available arrivals of different phases (P wave, fast S wave, and slow S wave), N is the number of measured fast S-wave polarization angles, Φ_j. Φ_j^{cal} is calculated from the given model parameters. The calculated origin time is $\tau_i = t_i - t_i^{cal}$, where t_i is picked i-th arrival time of all phases and t_i^{cal} is the corresponding predicted travel time. If the location is correct, the calculated origin time from all phases should be the same and $\tau_i - \bar{\tau}_i^{cal}$, where $\bar{\tau}_i^{cal}$ is the mean value of all τ_i, should be minimized. Because the inversion uses two completely different types of data, they should be normalized in the objective function. σ_{ti} is the uncertainty for arrival picking, and $\sigma_{\Phi j}$ is the uncertainty of fast S-wave polarization angle.

The Genetic Algorithm inversion requires inputting lower and upper bounds of model parameters but not the initial values. Model parameters are selected randomly between the bounds in each simulation. Reasonable bounds can successfully reduce the chance to converge at a local minimum and increase the efficiency of the inversion.

Constraints from well logging, core samples, and seismic models from reflection and refraction data are helpful in choosing the bounds on the velocity model.

Figure 2.2 shows the steps of the Genetic Algorithm inversion. Frist, the initial parent generation is produced with a population number. Each individual is one set of all model parameters $\mathbf{m}$ with values randomly chosen between the upper and lower bounds. Second, the fitness of each individual is evaluated based on the resulting objection function. Third, the children generation is produced via selection, crossover, mutation, and adoption. Selection uses stochastic universal sampling to choose parents for the next generation. Crossover uses a scattered method to combines two individuals for children. Mutation is to produce children by randomly changing some parameters of the parents. Fourth, fitness of all individuals from parents and children are sorted by the values of an objective function. Last, the best population numbers of individuals are selected for the next generation. Once the new generation is formed, it will go through the above process again until the stopping criterion is reached. The stopping criterion could be a certain generation number or a number indicating no improvement in the objective function.

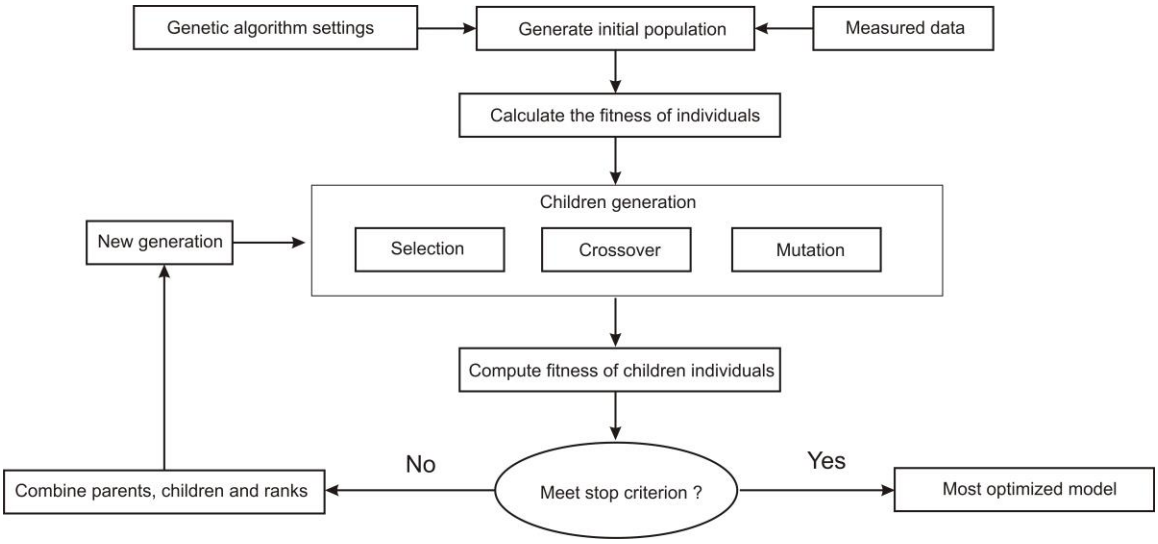

Figure 2.2: Flowchart of the Generic Algorithm inversion.

2.4 Synthetic tests with an effective homogeneous model

We first applied the above method to synthetic examples to determine its feasibility. The acquisition geometry of the experiment includes two vertical arrays with 10 receivers (N_g = 20) between x_3 = 750 m and x_3 = 930 m with an interval distance of 20 m (Figure 2.3). The surface locations of the two arrays are at x_1 = 130 m, x_2 = 315 m and x_1 = 290 m, x_2 = 220 m, respectively. Here x_1, x_2 and x_3 represent east, north and vertical direction. We modeled 5 microseismic events (N_e = 5), which are represented by blue dots in Figure 2.3. The design of this configuration geometry aims to simulate the common narrow ray coverage of microseismic data. An effective homogenous orthorhombic medium is assumed in the model. It allows an azimuth α of the crystallographic plane [x_1, x_3] from north to east and a dip angle β of the plane [x_1, x_2]. Bond transformation is applied to convert the medium to a stiffness tensor in Voigt notation c with components

$c_{IJ}(I, J = 1,...,6)$. This effective anisotropic model can be described by 11 independent parameters. We computed synthetic waveforms using the pseudo-spectral approach by Hung and Forsyth (1998). All five events had a double-couple source with a vertical fault plane that strikes in 60° from east to north. The size of **m** in this test is 26, including 15 for event locations ξ_e and 11 for the orthorhombic anisotropy medium.

Synthetic seismograms from one event recorded at two wells are shown in Figure 2.4. We picked P-wave and fast S wave arrivals from all seismograms. Waveforms of S wave are windowed with ending times marked by black crosses and are processed for splitting parameters. Figure 2.6 shows an example of S-wave splitting results at one receiver. The error surface (Figure 2.6[a]) has a well-constrained solution. The fast and slow S waves align well and the particle motion becomes linear after correcting the splitting effect (Figure 2.6[b]). All these characterizations suggest that S-wave-splitting measurements are reliable (Teanby *et al.*, 2004).

We first solved the problem using only P-wave and fast S-wave arrivals following the approach by Grechka and Duchkov (2011). The Frechet-derivative matrix is calculated analytically using the true-model parameters. Singular-value decomposition (SVD) is applied to the Frechet-derivative matrix. A condition number is defined as $c = \frac{\max s}{\min s}$, where s, the singular value, is obtained from the matrix. The smaller a condition number is, the more robust estimation of model parameters can be achieved (Grechka and Yaskevich, 2013). The calculated condition number is 1448 in this case. According to the rule of thumb given by Grechka and Yaskevich (2013), this number

indicates an ill-conditioned inverse problem and the model parameters cannot be robustly determined. Model parameters α and β are the main contributor to the eigenvectors that are characterized by small singular values, implying they are much less sensitive to travel times than other model parameters and more difficult to be resolved in this case.

To reveal how newly added full S-wave splitting data improve constraining α and β, we gave a perturbation from -1° to 1° for α and β with an interval 0.1°, and calculated normalized misfits for P-wave and fast S-wave travel times and for S-wave splitting data for each interval, respectively. The misfits at all intervals are summed together (Figure 2.5). Uncertainties for σ_{ti} and $\sigma_{\Phi j}$ in the calculation were given as 0.5 ms and 5° according to Verdon *et al*. (2009). σ_{ti} for picking arrivals was also set to 0.5 ms, which equals to the sample rate. The misfit for S-wave splitting parameters equals to 2.0 for α and 5.1 for β, which are much larger than the misfit for travel times (0.75 for α and 1.8 for β). This indicates that α and β are much more sensitive to S-wave splitting data. Therefore, adding splitting parameters proved to be helpful in constraining low-symmetry anisotropy in the velocity model.

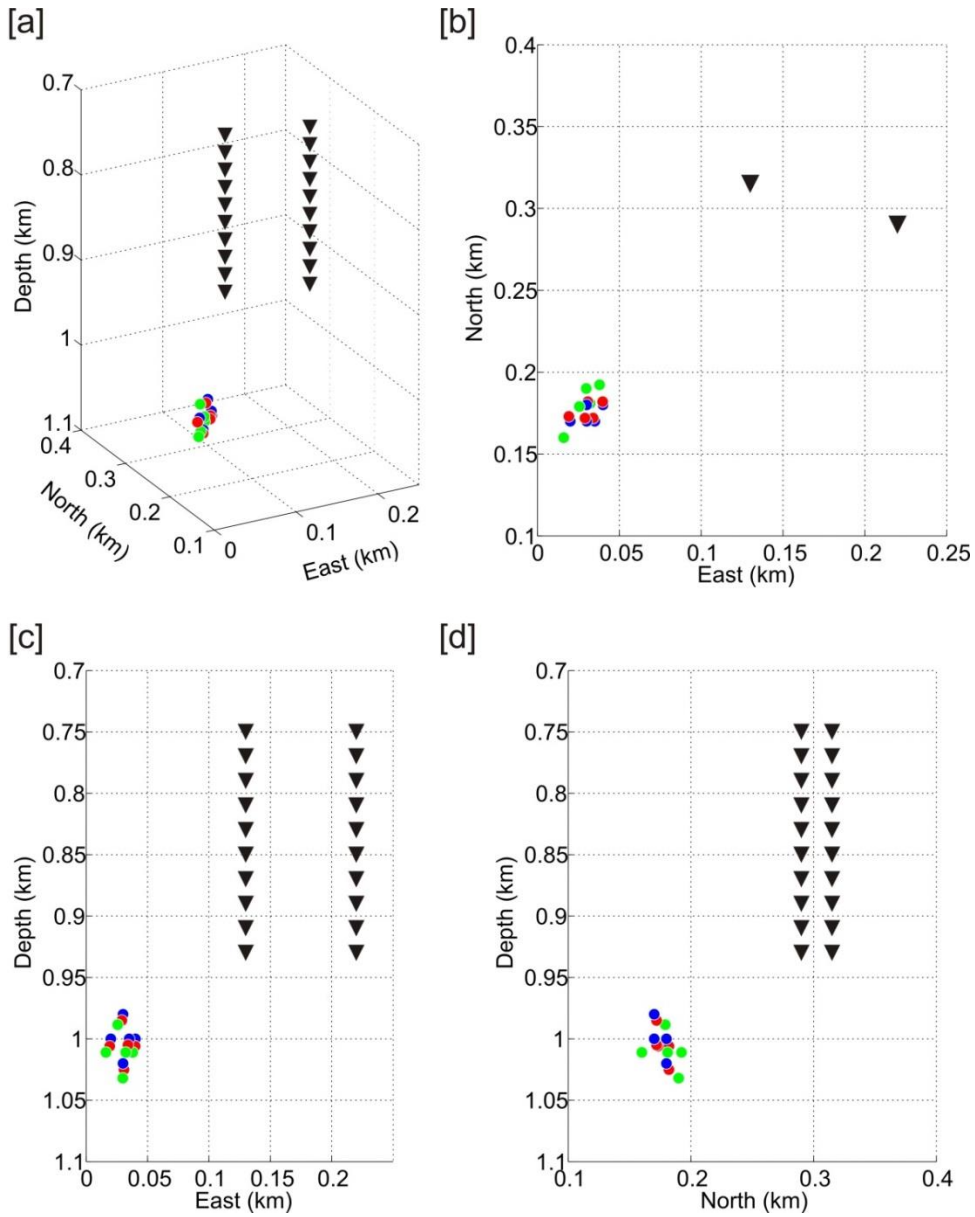

Figure 2.3: Comparison of true (blue dots) and determined event locations (red and green) in 3D [a], East-North [b], East-Depth [c], and North-Depth [d] views. Red dots represent results from an orthorhombic medium and green dots represent results from a VTI medium.

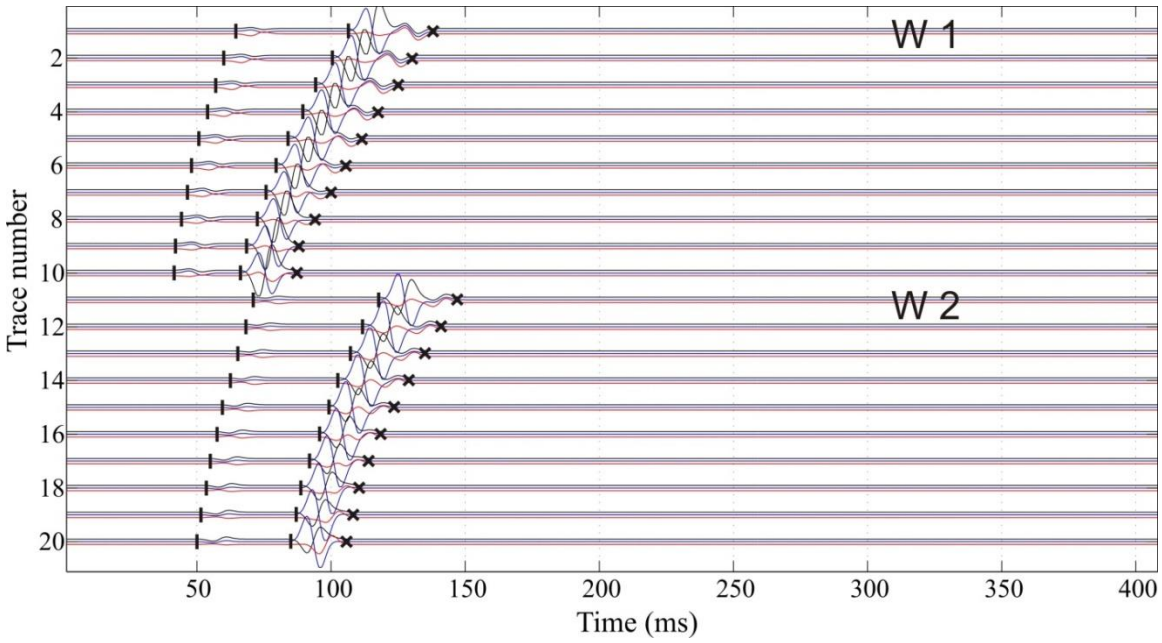

Figure 2.4: Synthetic waveforms recorded at downhole arrays from one microseismic event. Blue, black, and red waveforms represent east, north and vertical components, respectively. Black bars mark the picked arrival times of the P-wave and fast S-wave. Black crosses mark the ends-of-time windows used for S-wave splitting analysis.

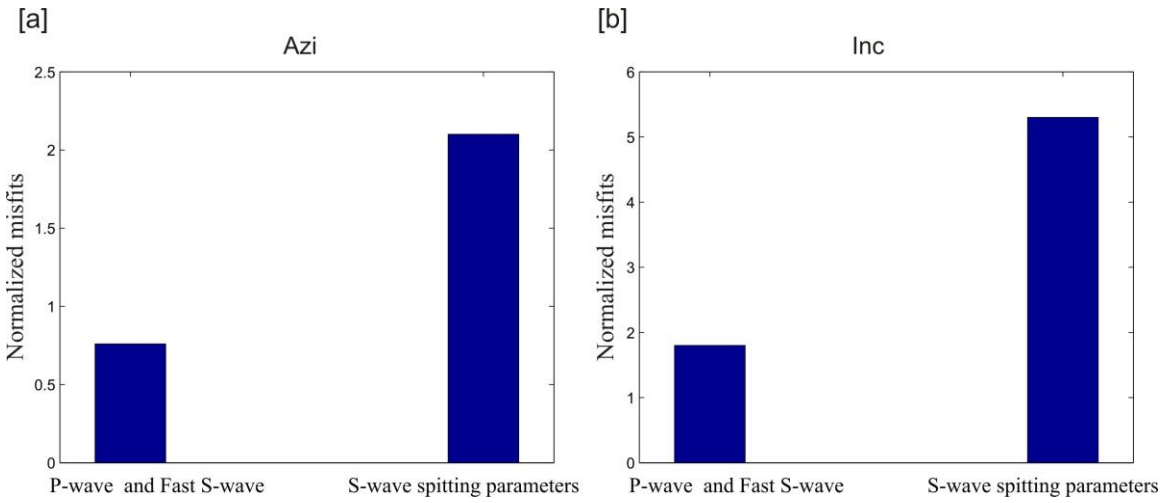

Figure 2.5: Comparison of the sensitivity between conventional arrival times and S-wave splitting parameters to symmetry, azimuth, and inclination angle of orthorhombic media.

We applied the GA inversion method to the synthetic data. The initial locations for all five events were the same point, which is the average from all true locations. 100 m perturbations were allowed in each direction for the upper and lower bounds for event locations. The upper and lower bounds for c_{IJ} were obtained from 20% perturbation of the true model (Table 2.1). We limited the population size to 2000 individuals and set the maximum generation as 200. The fitness of each individual was determined by Equation 2.6. If the solution does not change in three continuous generations, the GA inversion will stop and give the best solution.

The inverted elastic coefficients are listed in Table 1 and the event locations are shown in Figure 2.3 (red dots). All parameters of the velocity model are tightly constrained (Table 2.1) with the errors from 0% for c_{33} to 4% for c_{22}. The mean event location error ($\left|\xi_e^{cal} - \xi_e\right|$) is 2.3 m. It is important to point out that α and β, which cannot be constrained using conventional arrival times, were well recovered in this inversion. This synthetic test demonstrates the feasibility of our method in solving low-symmetry anisotropic media and event locations.

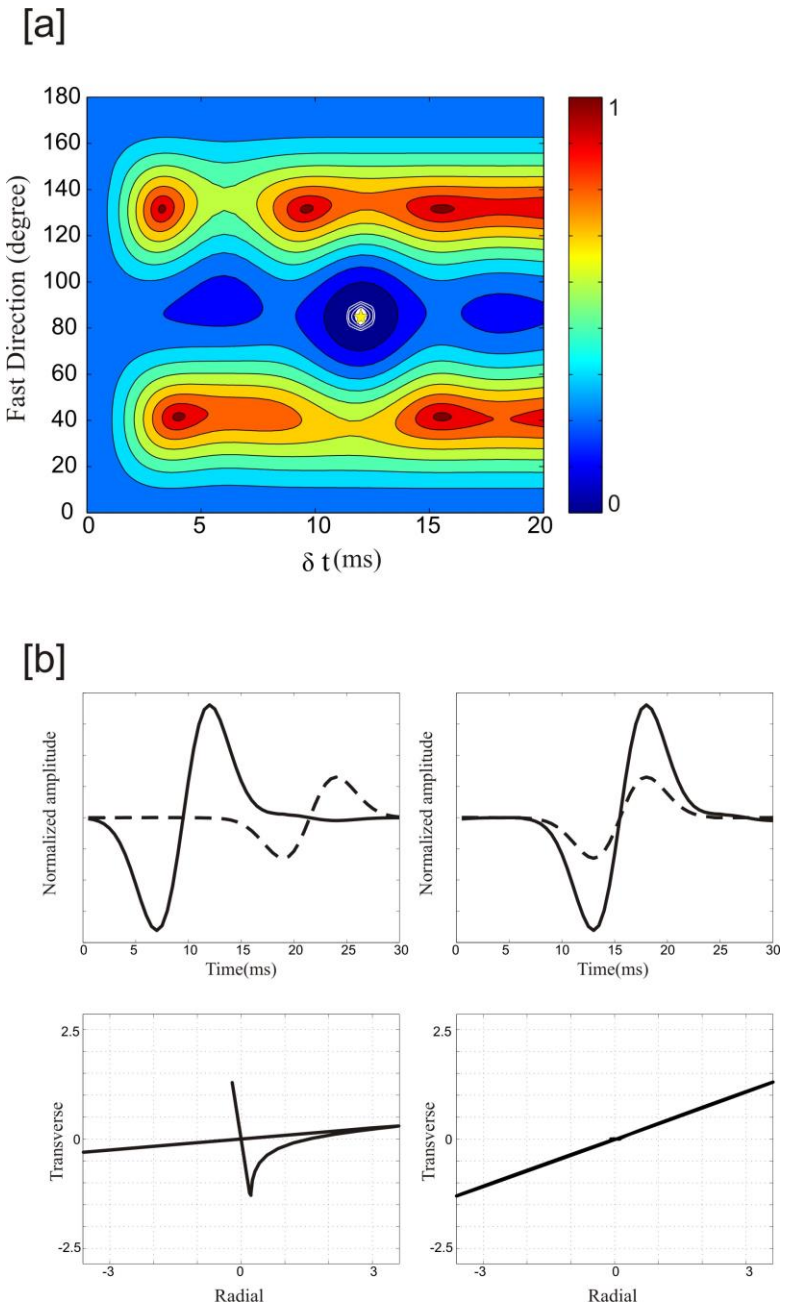

Figure 2.6: Example of S-wave splitting measurements of trace 18 at well H2. [a] The yellow star indicates the most optimal delay time and fast direction. White line represents the 2σ (95% confidence level) of the measurements. [b] Waveforms (top) and particle motions (bottom) before (left) and after (right) S-wave splitting correction. Solid line is for the fast S-wave and dashed line for the slow S-wave. Color here represents $\lambda_2 / \min(\lambda_2)$.

Table 2.1: True-model parameters, search bounds, inverted results, and errors from the synthetic data.

	True model	Lower bound	Upper bound	Inverted value	Errors
C_{11} (km^2/s^2)	21.5	17.2	25.8	21.9	0.4
C_{12} (km^2/s^2)	8.6	6.9	10.3	8.9	0.3
C_{13} (km^2/s^2)	8.8	7.0	10.6	9.0	0.2
C_{22} (km^2/s^2)	26.2	21.0	31.4	27.4	1.2
C_{23} (km^2/s^2)	9.2	7.4	11.0	9.1	0.1
C_{33} (km^2/s^2)	19.3	15.4	23.2	19.3	0
C_{44} (km^2/s^2)	7.3	5.8	8.8	7.4	0.1
C_{55} (km^2/s^2)	6.7	5.4	8.0	6.8	0.1
C_{66} (km^2/s^2)	7.8	6.3	9.4	7.7	0.1
α (degree)	60	0	180	58.3	1.7
β (degree)	10	0	90	9.5	0.5

We further solved the problem assuming a VTI medium to understand how the locations are affected by a simplified model. The upper and lower bounds for five stiffness coefficients c_{IJ} were obtained from 30% perturbation of the true model in this time and the GA inversion settings were kept the same as the previous test. We have found that the most optimized misfit increased three times, indicating a worse fit to the data, as shown by greens dots in Figure 2.3. An average location error was about 25 m in this case, much larger than that (2.3 m) obtained from an orthorhombic model. These errors are mainly caused by the assumption of a simplified anisotropy medium.

2.5 Synthetic tests with a heterogeneous model

The success of inversion in effective media described in previous section suggests the possibility of extending this method to more realistic heterogeneous models. We investigate the possibility using a two-layer model as shown in Figure (2.7). The first layer is an isotropic layer with P-wave velocity 4.5 km/s and S-wave velocity 2.6 km/s. The bottom layer is an orthorhombic layer that is described by density normalized stiffness matrix (in km^2/s^2)

$$\begin{bmatrix} 19.8 & 8.6 & 9 & 0 & 0 & 0 \\ 8.6 & 25.8 & 9.1 & 0 & 0 & 0 \\ 9 & 9.1 & 20.7 & 0 & 0 & 0 \\ 0 & 0 & 0 & 7.2 & 0 & 0 \\ 0 & 0 & 0 & 0 & 8.1 & 0 \\ 0 & 0 & 0 & 0 & 0 & 6.5 \end{bmatrix} \tag{2.7}$$

The locations of events and receivers are the same as in the previous synthetic test (Figure 2.7). Following the same procedures, we first generate synthetic waveforms (Figure 2.8). Then we pick arrival times of P-wave and fast S-wave. Model parameters include 9 stiffness coefficients, 2 isotropic velocities and 15 components of event locations. Azimuth and dipping of symmetry planes were not included in this inversion for simplicity. In this case, forward prediction for travel times and splitting parameters cannot be derived analytically as in the effective media. Ray tracing is needed in the forward calculations, which significantly increased the computing time.

The calculated-condition number as defined before is 660 in this case, indicating a mild ill-conditioned inverse problem and the model parameters cannot be robustly determined. Next, we measured S-wave-splitting parameters (Figure 2.9) and applied our inversion method to the problem using S-wave-splitting data in addition to P-wave and fast S-wave travel times. The initial locations for all five events are the same as in the last test. We still gave 100 m perturbation range for each direction for the upper and lower bounds. The upper and lower bounds for stiffness coefficients were obtained from 20% perturbation of the true model (Table 2.2). We limited our population size to 1000 individuals and set the maximum generation to 100. If the solution does not change in five continuous generations, the GA inversion will stop and give the best solution.

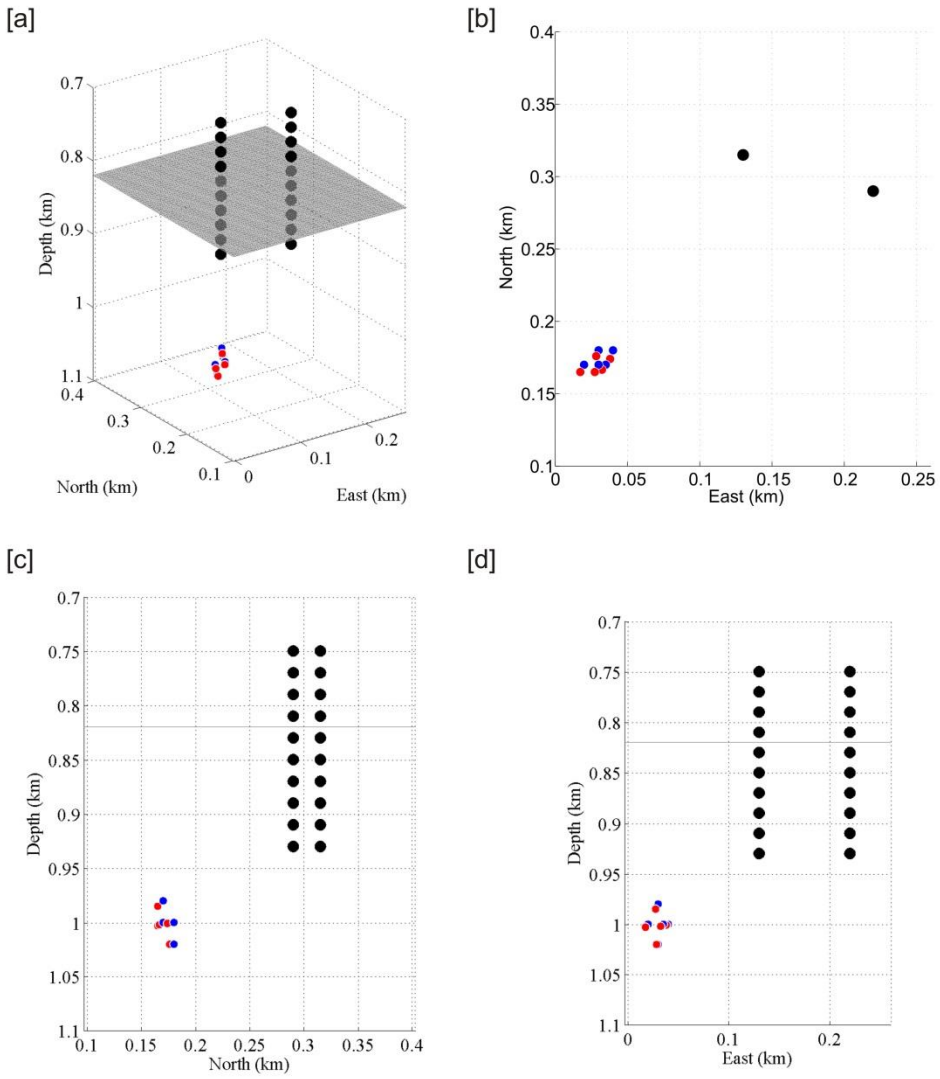

Figure 2.7: Comparison of true (blue dots) and determined event locations (red dots) in 3D [a], East-North [b], North-Depth [c], and East-Depth [d] views. Black solid dots represent receivers. The gray plane in [a] is the interface between the two layers.

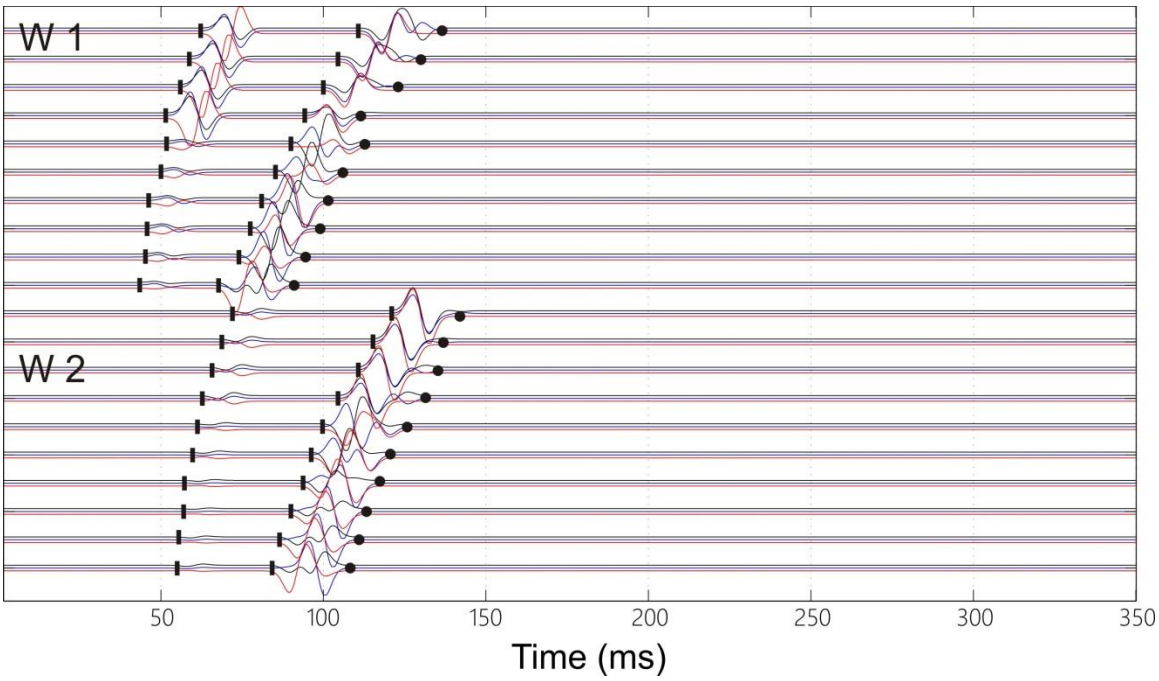

Figure 2.8: Synthetic waveforms recorded at downhole arrays from one microseismic event. Blue, black, and red waveforms are for east, north, and vertical components, respectively. Black bars mark the picked arrival times of the P wave and fast S wave. Black crosses mark the ends-of-time windows used for S-wave splitting analysis.

As mentioned before, dense ray coverage is the key for a successful inversion result. Figure 2.10 shows P-wave, fast, and slow S-wave ray paths in this heterogeneous media. We can see clearly ray bending at the interface. In addition, Figure 2.10 also shows that ray-coverage changes significantly in different layers.

[a]

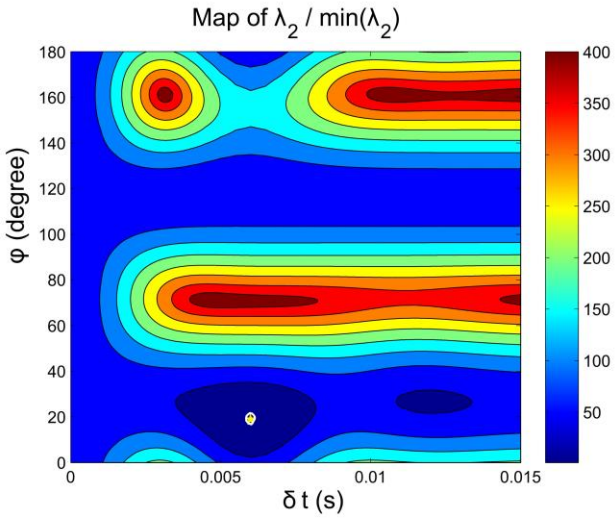

[b]

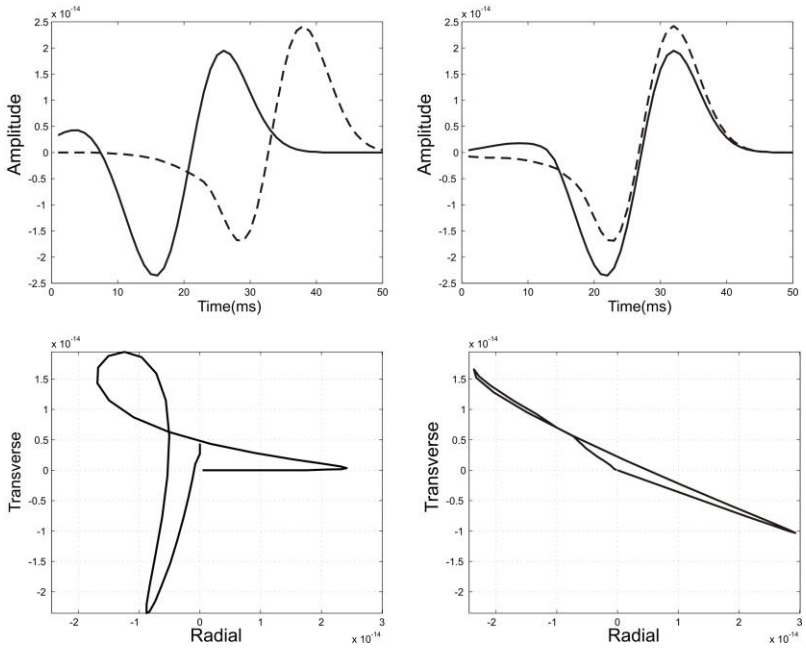

Figure 2.9: Example of S-wave splitting measurements of trace 18 at well 2. [a] The yellow star indicates the most optimal delay time and fast direction. White line represents the 2σ (95% confidence level) of the measurements. [b] Waveforms (top) and particle motions (bottom), before (left), and after (right) S-wave-splitting correction. Solid line is for the fast S-wave and dashed line for the slow S-wave.

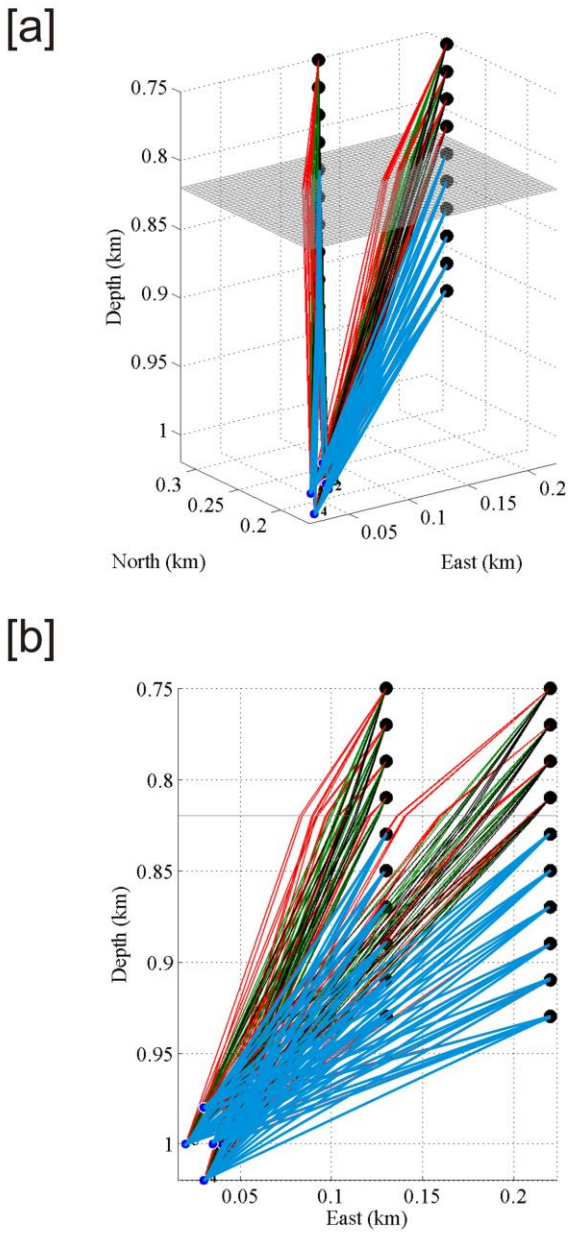

Figure 2.10: The ray paths of P-wave (black lines), fast S-wave (green lines) and slow S-wave (red lines) of five microseismic events in the 3D view [a], side view [b]. The blue dots represent events and big black dots represent the receivers.

Table 2.2: True-model parameters, search bounds, and inverted results from synthetic data.

	True model	Lower bound	Upper bound	Inverted value
C_{11} (km^2/s^2)	19.8	15.8	23.7	21.2
C_{12} (km^2/s^2)	8.6	6.9	10.3	8.9
C_{13} (km^2/s^2)	9.0	7.2	10.8	8.8
C_{22} (km^2/s^2)	25.8	20.6	30.0	26.9
C_{23} (km^2/s^2)	9.1	7.3	11.0	9.2
C_{33} (km^2/s^2)	20.7	16.6	24.2	20.6
C_{44} (km^2/s^2)	7.2	5.8	8.6	7.3
C_{55} (km^2/s^2)	8.1	6.5	9.7	8.3
C_{66} (km^2/s^2)	6.5	5.2	7.8	6.5
Vp (km/s)	4.6	3.7	5.5	4.5
Vs (km/s)	2.6	2.1	3.1	2.5

As shown in Figure 2.7, the inverted locations (red dots) are generally close to the true locations (blue dots). In the horizontal directions, the located events are shifted slightly with an average error of 6 m. The error in the vertical direction is 1.8 m owing to the vertical distribution of receivers. The lack of horizontal variations in receiver locations is the cause for the relatively large error in the horizontal plane.

Due to different ray-angel coverage, the velocities of the two layers are recovered with varying degrees of success. The first layer is an isotropic layer, only two parameters, Vp and Vs, were used to describe the elastic property. Ray coverage (Figure 2.10) is dense enough to recover Vp and Vs with an error of 0.1 km/s (Table 2.2). Layer two is orthorhombic and needs 9 parameters to describe. Some parameters such as C_{11} and C_{22} have slightly larger errors. The rest of stiffness coefficients are well-resolved. This

synthetic test demonstrates the feasibility of extending our method from an effective homogeneous medium to a heterogeneous medium for event locations and velocity model building. Extending the model to more anisotropic layers is possible but will involve more model parameters.

However, when a media is composed of several strong azimuthal anisotropic layers, this method needs be tested for different scenarios.

2.6 Discussion

Low-symmetry anisotropic velocity model building using only P-wave and fast S-wave arrival times requires sufficient ray coverage to constrain model parameters (Grechka and Yaskevich, 2013). However, ray coverage for downhole acquisition during hydraulic fracturing is significantly poor for retrieving low-symmetry anisotropy using the conventional methods. A common practice is to assume a high-symmetry anisotropy. This assumption certainly brings errors in event locations as demonstrated in our synthetic test. Instead of reducing model parameters for a stable inversion, we added new parameters, S-wave splitting, to solve this problem. As demonstrated in the synthetic tests, anisotropy parameters, like α and β, cannot be resolved using P- and fast S-wave arrival times. By including the S-wave-splitting parameters in the data, anisotropy can be better constrained even for relatively sparse ray coverage, which is common for microseismic data. We have carried out a number of tests to investigate the effects of arrival times and

fast directions on the obtained velocity model and found these parameters could change case by case with ray numbers and directions.

As to our knowledge, this paper is the first attempt to include full S-wave splitting measurements in microseismic velocity model building. Grechka *et al*. (2014) included both fast and slow S-wave arrivals in the procedures of event locating and velocity model building. They picked travel times of slow S-waves in the vertical component. A basic prerequisite for this picking of slow S-wave arrivals is that the medium does not present strong azimuth anisotropy. Otherwise, fast S wave would polarize from the horizontal direction and can also present in the vertical component. Therefore, fast and slow S waves interfere with each other, which makes it difficult to identify and pick slow S-wave arrivals. This phenomenon is clearly evidenced in synthetic microseismic data at receivers 11-16 in Figure 2.4. In this case, it is difficult to pick slow S-wave arrival times manually. However, we have demonstrated that S-wave splitting parameters (Φ, δt) can be obtained from a grid search method, which not only improves the accuracy of slow S-wave arrivals but also adds a new type of data for anisotropic velocity model building.

There are several advantages of S-wave splitting analysis that we introduced in this study. First, the method of Silver and Chan (1991) utilizes full waveform information and gives reliable splitting parameters. Second, using the delay times for S-wave splitting avoids the manual judgment in picking slow S-wave arrivals, which could be contaminated by fast S-waves when azimuthal anisotropy is present. Third, this method can obtain fast S-wave polarization, which has important constraints on some model parameters. Fourth, the uncertainties of splitting parameters are also calculated, which is

critical in normalizing different types of data in the inversion. It is worth noting that measuring S-wave splitting from microseismic waveforms needs a rotation of the coordinate system according to P-wave polarization, whose determination requires high-quality P wave data.

It is important to use well-constrained S-wave-splitting measurements and exclude those with large uncertainties and null measurements, which means that S-wave splitting is not detected. The observations of nulls from all directions indicate the medium is largely isotropic. This situation is impossible to investigate using microseismic data due to limited azimuth coverage of ray paths. Null measurements can also be caused when an S-wave travels through the singularity direction of a medium. S-wave wavefronts are complex in a low-symmetry anisotropic medium and have a large chance of hitting the singularities (Grechka, 2015). It is also possible that the small amplitude of slow S-waves caused by certain focal mechanisms is masked by noise. Although the success rate of S-wave-splitting parameter measurements for real data may not be high for some datasets (Teanby, *et al*., 2004), relatively high-quality measurements from some events can still be obtained from certain traces, such as our real data examples. Even adding a small number of S-wave-splitting parameters would provide valuable information for constraining the low-symmetry anisotropic velocity model. If no S-wave splitting is present in microseismic data, this method will be equivalent to conventional inversion methods using P- and fast S-wave travel times.

Theoretically, S-wave emitted by a microseismic event splits into fast S wave that polarizes near horizontally and slow S-wave that polarizes near vertically in a VTI

anisotropic medium. As the wavefield enters another VTI media, the polarization directions of split S-waves will not change that much which means the number of S-wave phases recorded are still two. In this case, this method works well. However, if the wavefield enters an anisotropic layer with a strongly tilted symmetry axis, the fast and slow S-waves should split again and form four phases (Fu *et al*., 2012). This situation could cause some troubles for this method if all split S waves are well separated because it will be difficult to determine the correct fast and slow S waves for splitting measurements from many phases. This case is possible when the media have strong anisotropy and the delay times among all split phases are larger the given period. However, from real data observations, this is seldom the case. The fast and slow waves are the integral results of the multi-split S waves. The splitting parameters can be measured as shown in real data. Synthetic tests are needed to figure out how the delay time is represented from forward calculations, between the fastest and slowest waves or some combination of multi-split waves. Grechka (2015) emphasized the difficulties of handling multiple split S-waves in layered media by ray tracing theory. A full extension of this joint inversion method from an effective homogeneous medium to heterogeneous media is possible but should be carefully tested using synthetic data for a model with multiple strong azimuthal anisotropic layers.

We also want to point out the low efficiency of GA inversion if the bounds of event locations are large. Several ways help to get around this problem. One way is to locate the selected events using a linear inversion method before applying the GA inversion. Another approach is to locate the selected events for velocity-model building from an

isotropic model and regard the results as initial guesses in the next-round inversion. We have found that the efficiency of GA inversion dramatically increases when the bounds of event locations are reduced. After the anisotropy model is built from the GA inversion, other conventional methods can be used to locate other events subsequently.

Besides using the difference between the input and inverted model parameters to understand the model resolution, the uncertainties of model parameters could be estimated from probability density functions in the GA inversion. To do that, all models selected during the inversion should be recorded. Then a probability density function can be obtained for each model parameter. The standard deviations can be estimated, which will help to estimate which model parameters are well constrained. The actual errors depend on many factors including ray coverage and uncertainties in arrival picking and splitting measurements.

2.7 Conclusion

S-wave splitting parameters are fully considered in building anisotropic velocity models from microseismic data. The delay time of slow S-wave and polarization of fast S-wave can be measured from microseismic data in a ray coordinate system. Our experiments using two synthetic tests from effective homogeneous and heterogeneous media lead to the following conclusions.

(1) Instead of assuming a high-symmetry anisotropic model that results in relatively large locating errors, adding S-wave-splitting parameters to the traditional P- and

fast S-wave arrival dataset significantly improves the determination of a low-symmetry anisotropic model and the accuracy of event locations.

(2) The method of measuring S-wave-splitting parameters from waveforms is not only suitable to medium with strong azimuthal anisotropy, from which manually picking the slow S-wave arrival time is difficult, but also adds to the uncertainty of each measurement critical to form an objective function of subsequent GA inversion.

(3) The inversion is more efficient when the bounds of event locations are well assessed based on the locations obtained from an isotropic model using a conventional method based on travel times.

3 Chapter 3

Joint inversion for anisotropic velocity model and event locations using S-wave splitting measurements from downhole microseismic data – Implementation with Field Data

3.1 Introduction

In chapter 2, we presented the methodology and synthetic tests of joint inversion for an anisotropic-velocity model and microseismic-event locations using S-wave splitting measurements. In this chapter, we applied this method to the field data acquired from the Bakken reservoir.

The Bakken Formation is located in the Williston Basin in North Dakota, Montana, and up into southern Saskatchewan, Canada. The formation consists of three layers: an upper shale layer, a middle dolomite layer, and a lower layer of shale. The Bakken formation is underlain by the Upper Devonian Three Forks Formation and overlain by the Lodgepole Formation and Mission Canyon Formation. Organic-rich shales in the Bakken are excellent source rocks for petroleum (Meissner, 1991).

To maximize production by finding an optimal completion, Hess Corporation launched a microseismic project in the Bakken reservoir. There were two treatment wells, H3 and H2 wells, which horizontally penetrated through the Bakken reservoir. The stimulation was conducted first in the H3 well by 29 stages and followed in the H2 well

by 38 stages between September 26, 2011, and October 16, 2011. These locations are shown in Figure 3.1. Apex, a company of Sigma Cube, used six deep, vertical observation wells (OB) to record the stimulated induced microseismicity. Schematics of the site, the two treatment wells and the six observation wells are seen in Figure 3.2 and Figure 3.3. Figure 3.2 also includes the locations of each stage and Figure 3.3 shows stratigraphic tops supplied by Hess Corporation (Mission Canyon is also named with Rival). The main objective of this chapter is to obtain a low-symmetry velocity model and improve event locations utilizing S-wave spitting parameters.

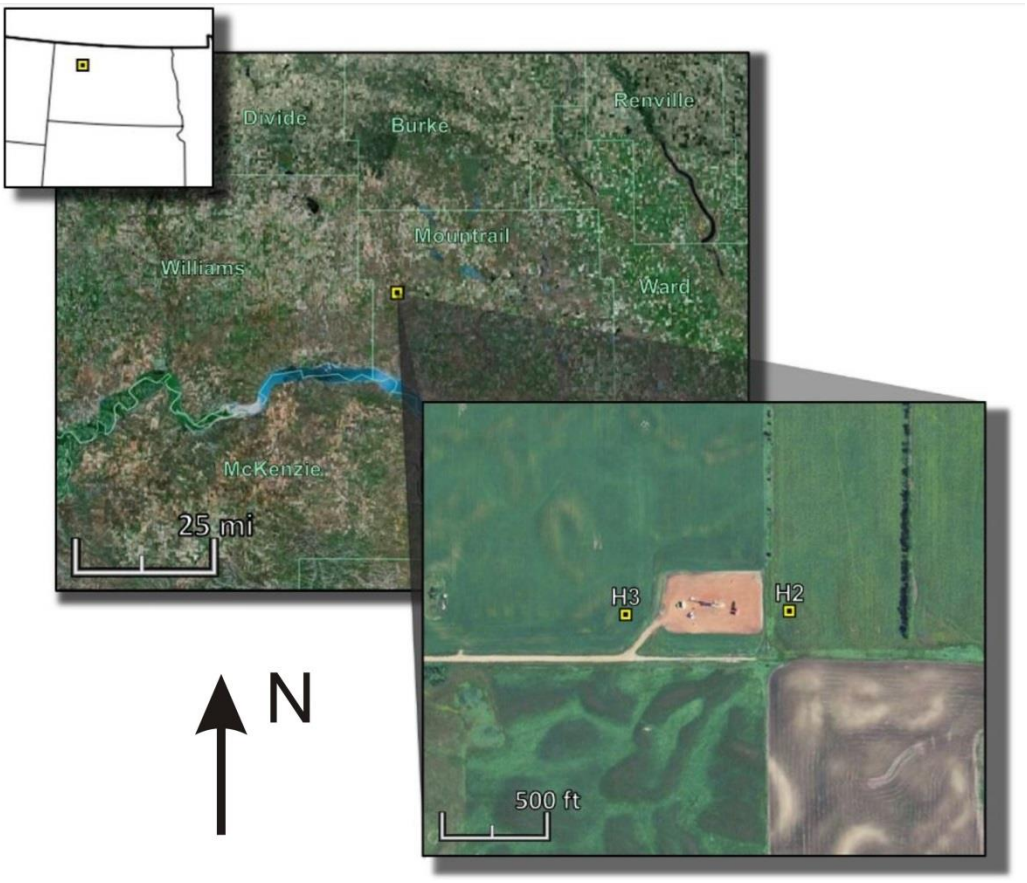

Figure 3.1: Locations of EN Person 156-94-1102-H2 and H3 wellheads (Apex Report).

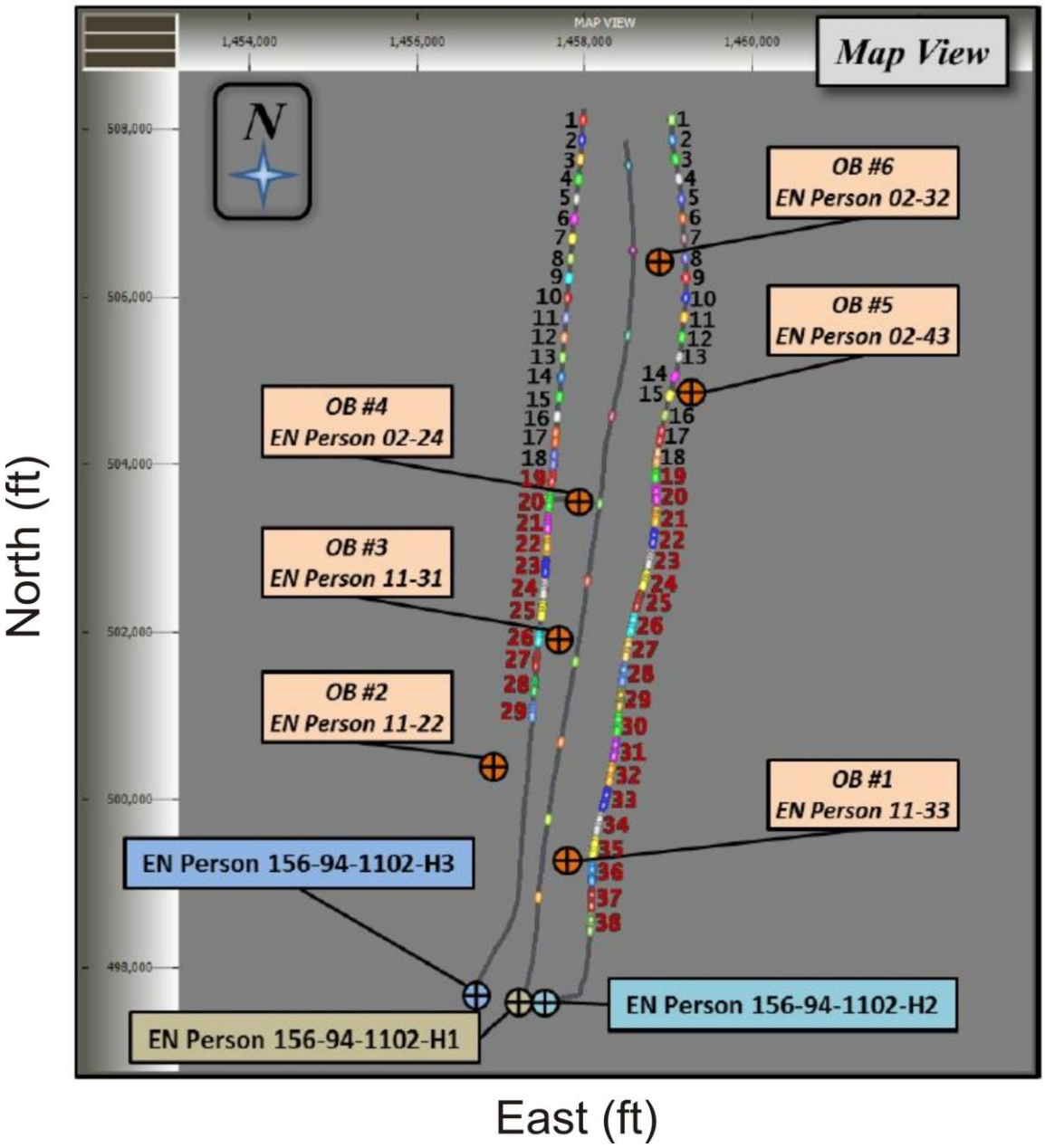

Figure 3.2: Map view of the fracturing and monitoring site showing the H3 and H2 treatment wells with the stages color-coded and numbered. H1 is a previously-completed, producing well; six observation wells are the EN Person 11-33, 11-22, 11-31, 02-24, 02-43, and 02-32. Stages labeled with black numbers used ball-actuated, sliding sleeves; Stage labeled with red numbers used pump-down plug-and-perforation guns (Apex report).

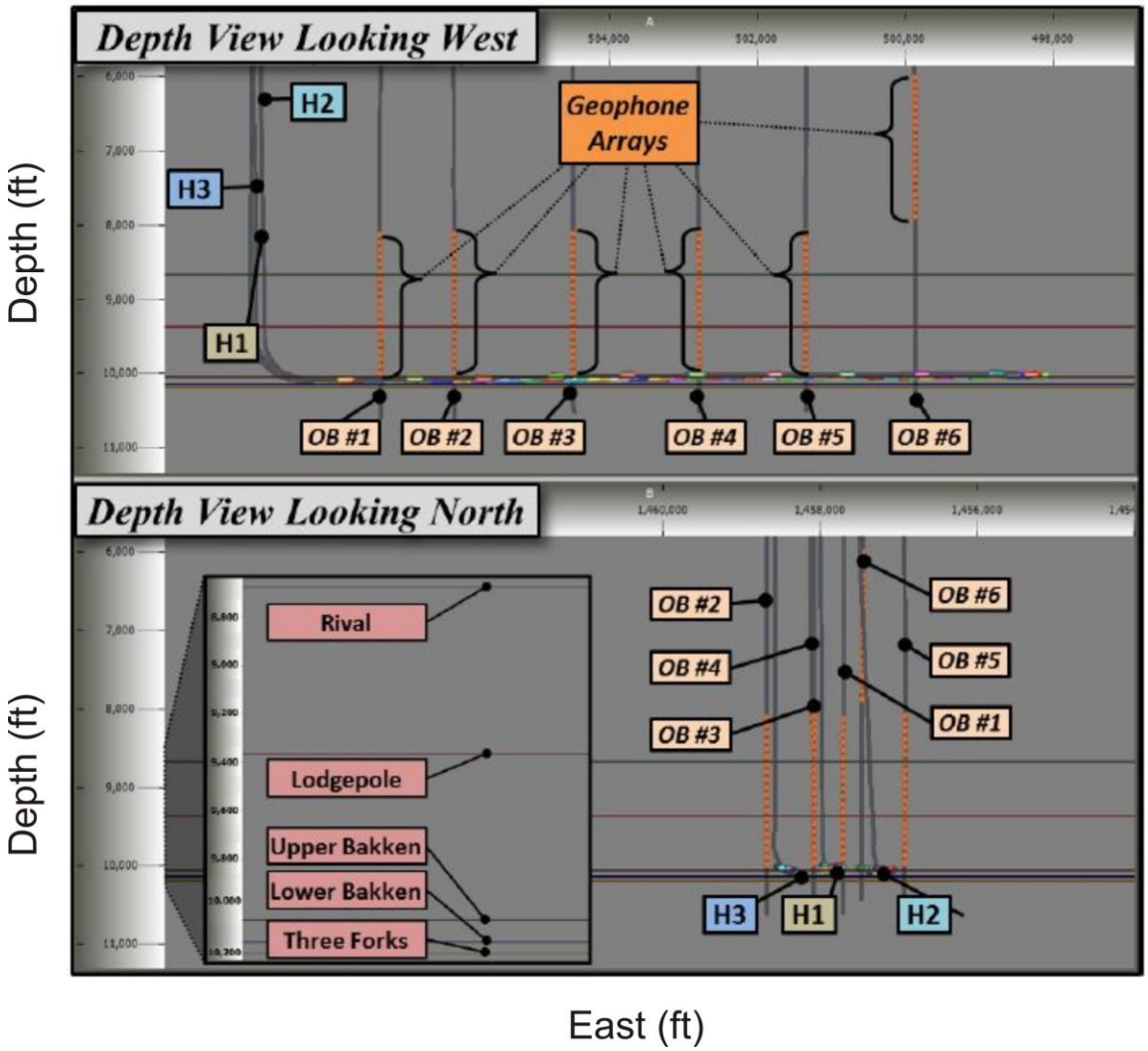

Figure 3.3: Depth views of the treatment wells, H3 and H2, the H1 well, the geophone arrays in the observation wells and annotated formation tops (Apex report).

3.2 Joint inversion

The raw data provided by Apex have been digitized with 10s length Segd files (Figure 3.4). Such signal lengths may cause some difficulties in data processing. We began processing by further cutting raw data with a 1 second length. Next, we ran a 75-340 Hz bandpass filter to remove some ambient noises. Considering limited computational power, only data from stages 22-23 of treatment well H2 is utilized in this test. After events triggering, 49 microseismic events with clear P-wave and split S-wave arrivals were selected to do the joint inversion. To simulate the case that is characterized by relative less dense ray coverage, we used 2 monitoring wells, Ob2 (EN Person 11-22) and Ob3 (EN Person 11-31), where S-wave splitting is well recognized. After a 3C geophone has been lowered into a vertical borehole, the geographic directions of its horizontal geophones are not known. However, to use S-wave-spitting measurements, the directions of the geophones must be known. Therefore, horizontal geophone orientations were determined first. As shown in Figure 3.5, we compared calculated azimuths using perforation shots with measured azimuths and obtained the rotation matrix for each receiver. Then we mathematically rotated horizontal geophones to geographic directions. After rotation, we pick arrival times of P-wave and fast S-wave manually (Figure 3.6).

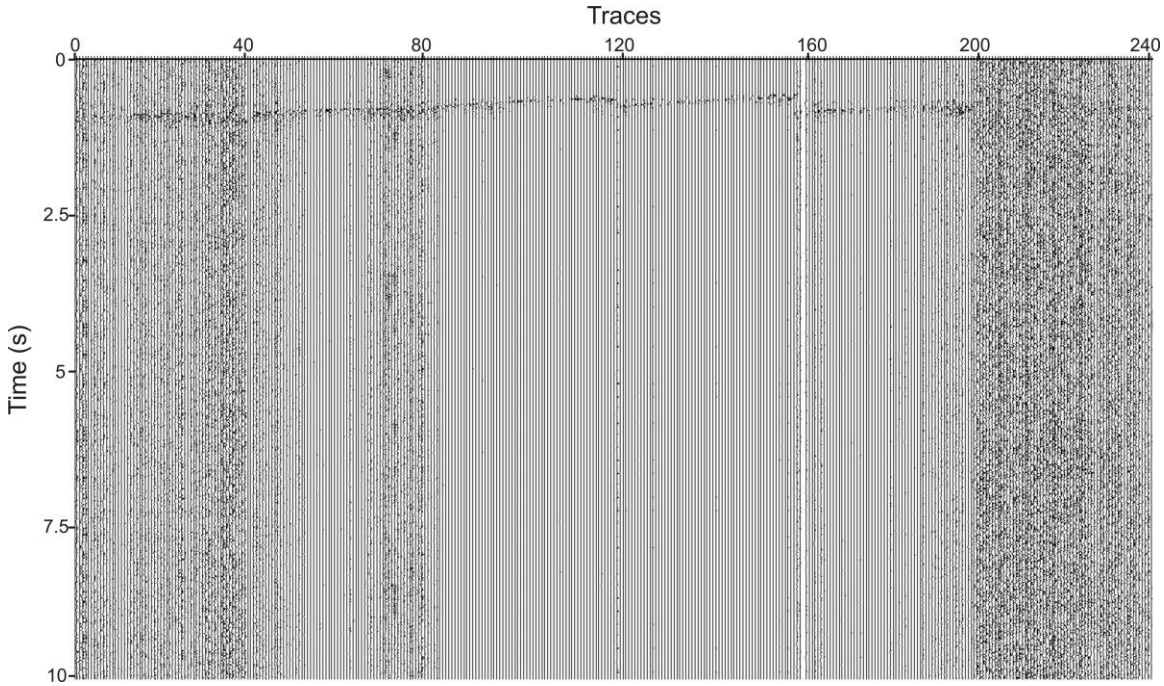

Figure 3.4: An example of a raw Segd file of raw microseismic data.

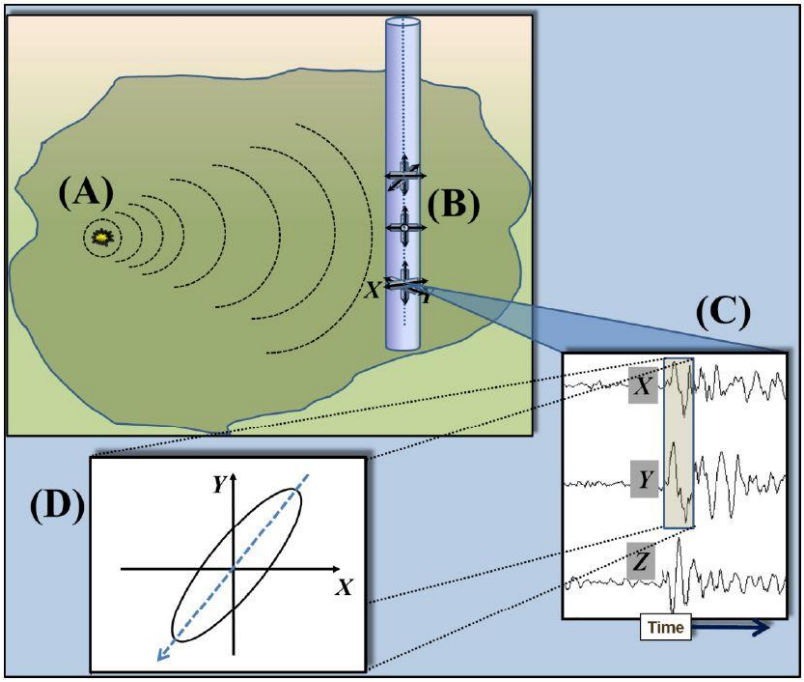

Figure 3.5: Schematic of determining the orientation of the horizontal geophones of a 3-component geophone array using (A) a known, controlled seismic source (perforation shot) radiating wave energy, (B) the geophone array recording the wave energy, (C) the 3 components of recorded signals, and (D) the hodogram of the signals (Apex report).

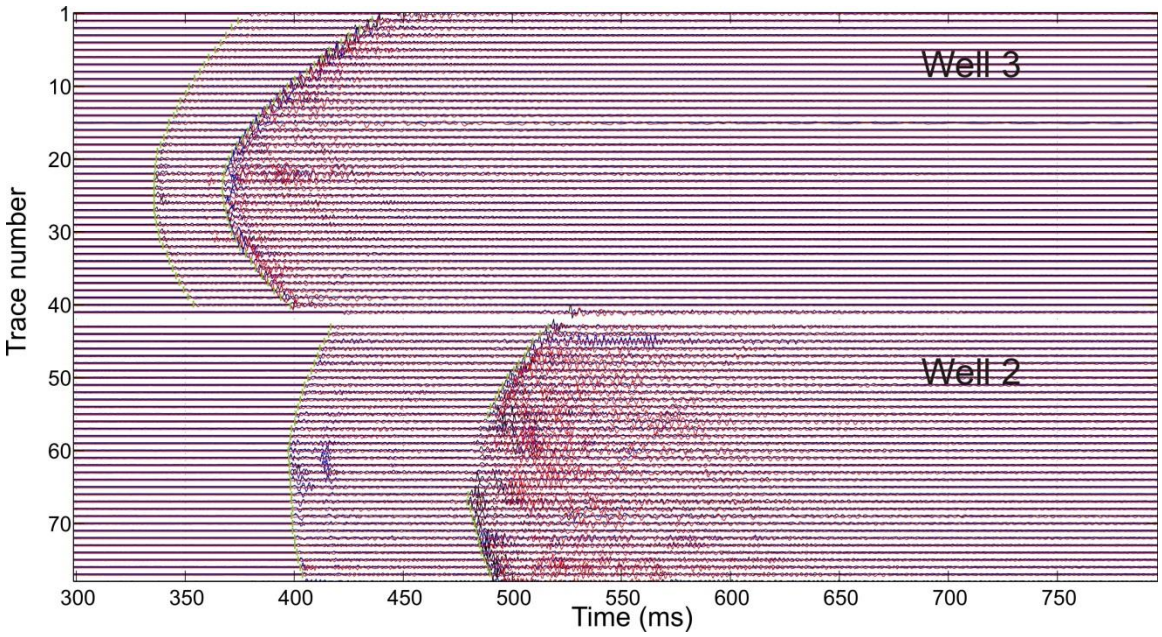

Figure 3.6: Waveforms recorded at well 2 and well 3 from one microseismic event occurring above the treatment wells. Blue, black and red waveforms are for east, north and vertical components, respectively. Green bars mark the picked arrival times of P-wave and fast S-wave.

Then we performed S-wave splitting analysis and obtained more than 200 high-quality splitting parameters. One example of S-wave-splitting measurement is given in Figure 3.7. We used a signal-noise ratio (SNR) 4 as a threshold in selecting reliable S-wave-splitting data for high-quality splitting measurements. The SNR here is defined by $A(sig)/A(noi)$, where $A(sig)$ and $A(noi)$ are the norm of signal and noise amplitude vector divided by each vector length, respectively. For noisy traces that do not have reliable splitting parameters, we picked slow S-wave on the vertical component (Figure 3.8) if they can be recognized as suggested by Grechka and Yaskevich (2014).

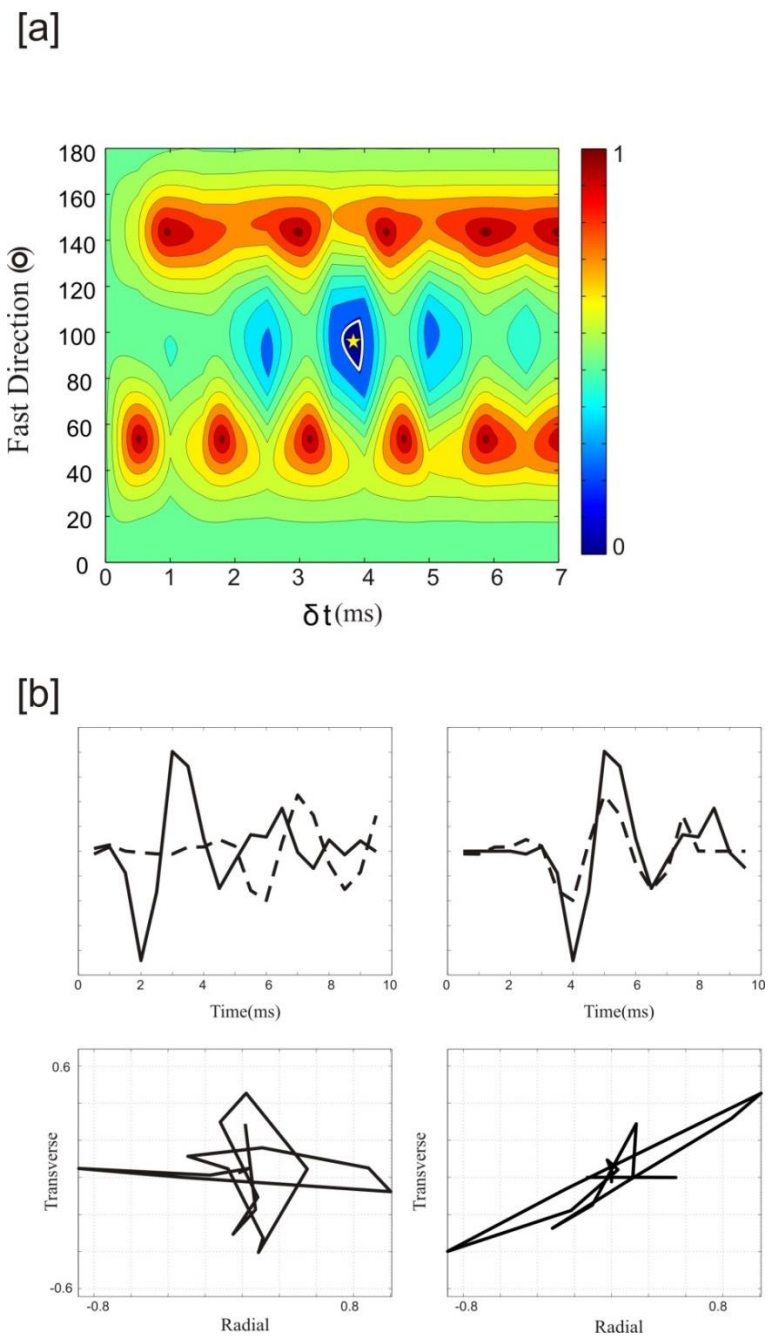

Figure 3.7: Example of S-wave splitting measurements of one trace. [a] The yellow star indicates the most optimal delay time and fast direction. White line represents the 2σ (95% confidence level) of the measurements. [b] Waveforms (top) and particle motions (bottom) before (left) and after (right) S-wave splitting correction. Solid line is for the fast S-wave and dashed line for the slow S-wave. Color here represents $\lambda_2 / \min(\lambda_2)$.

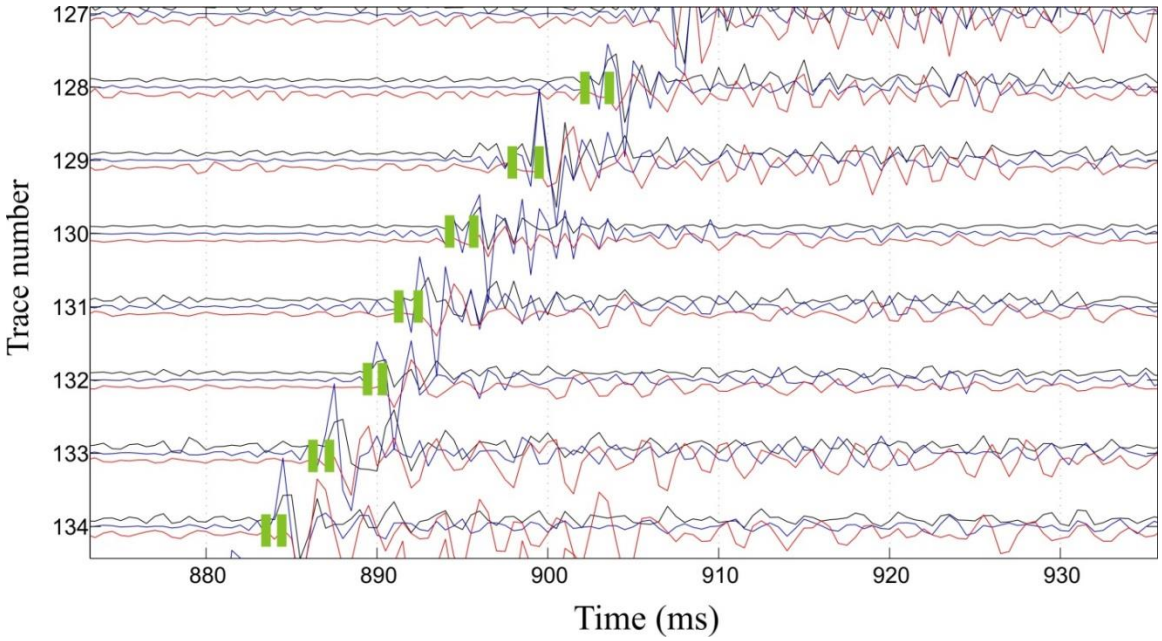

Figure 3.8: Example of microseismic data from the Bakken shale. Blue, black, and red are for east, north, and vertical components. Slow S waves dominate the vertical component (red line). Green bars are identified arrival times of the fast and slow S waves.

From Figure 3.2, the very thin Bakken reservoir is overlain by the thick Lodgepole formation and Rival or Mission Canyon formation (Li *et al*., 2014). As shown in the blocked sonic logs of Ob 3 (Figure 3.9), considering the similarity of elastic properties in the two formations, we considered them as one effective homogeneous layer named LP (Figure 3.9). According to the interpreted layer depth from well-logging data, all layers were set to be horizontal because the structure dip is less than 2°.

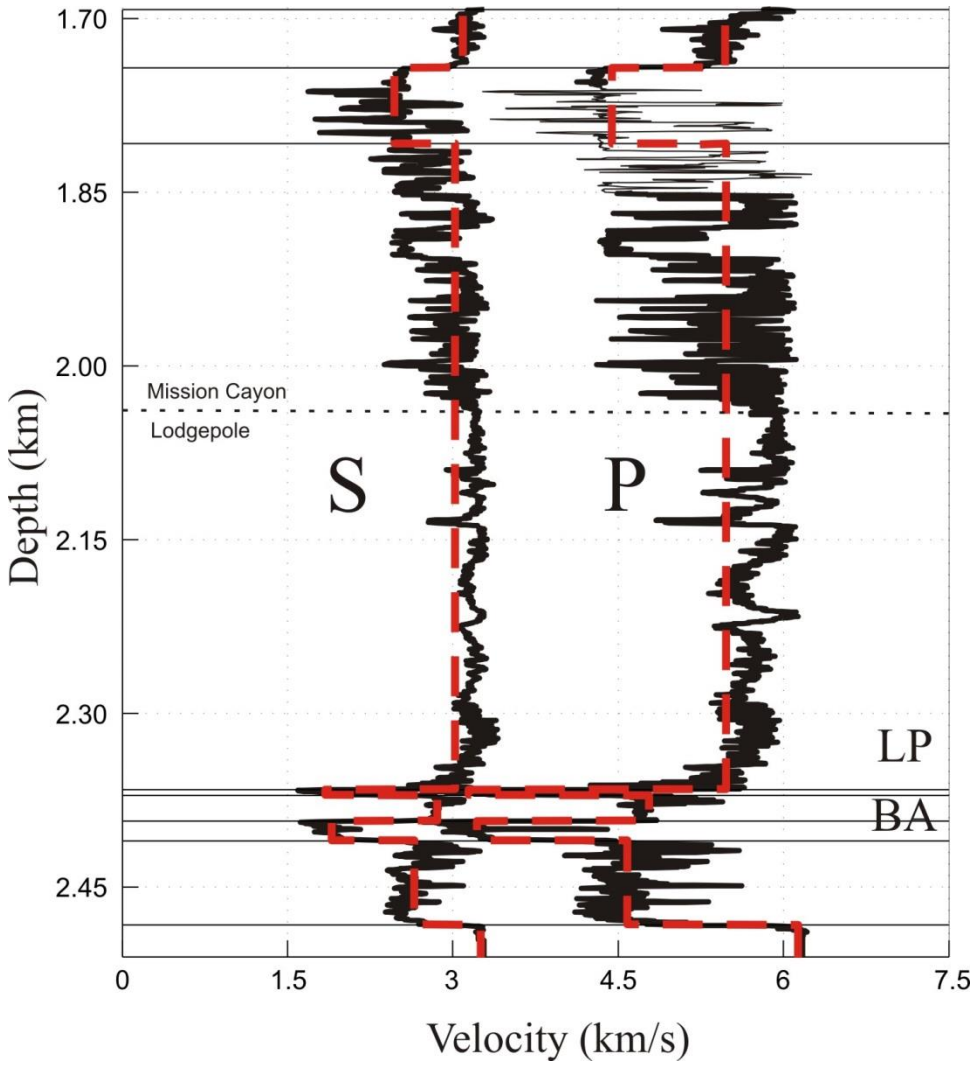

Figure 3.9: Sonic logs (solid line) and blocked isotropic velocity models (red dashed line) of P- and S-waves. LP is for the effective medium of the Mission Canyon formation and the Lodgepole formation, BA is for the Bakken formation. Black dashed line is the boundary between the Mission Canyon formation and the Lodgepole formation.

After having the data ready, we first used an isotropic model obtained from the blocked sonic log (Figure 3.9) to locate the selected events. All events were located within the LP formation and around 250 m shallower than the Bakken formation and treatment wells (Figure 3.10). These unusual locations probably indicate that these events occurred on pre-existing natural cracks. The majority of ray paths therefore concentrate in the LP formation. We considered an effective orthorhombic anisotropic velocity model for the LP layer in the inversion. Previous studies in the same reservoir (Table 2 in Grechka and Yaskevich (2014)) reveal that the LP formation is not characterized by strong anisotropy, which helps to assess the search range in event locations in our anisotropic inversion. We added 150 m perturbations to the locations from the isotropic inversion as the searching bounds. The initial velocity model was constructed mainly from sonic logs. We allowed 30% perturbations to the generated stiffness coefficients for the lower and upper bounds. Azimuth (α) and inclination (β) bounds, which represent the angle of the plane$[x_1, x_3]$ from east to north and the angle of the plane $[x_1, x_2]$ from the horizontal plane were set from 0° to 180° and 0° to 45°, respectively. We used a population number of 2000 and a generation number of 200 in the GA inversion. The inverted density normalized stiffness tensor ($\mathrm{kft}^2/\mathrm{s}^2$) is

$$\begin{bmatrix} 386.2 & 158.3 & 160.7 & -2.9 & -16.2 & 5.7 \\ 158.3 & 370.1 & 142.4 & -0.5 & -6.9 & 1.4 \\ 160.7 & 142.4 & 324.5 & -1.1 & -10.6 & 5.1 \\ -2.9 & -0.5 & -1.1 & 99.6 & -0.6 & -3.2 \\ -16.2 & -6.9 & -10.6 & -0.6 & 96.5 & -0.8 \\ 5.7 & 1.4 & 5.1 & -3.2 & -0.8 & 106.9 \end{bmatrix}.$$

Or with the unit km^2/s^2

$$\begin{bmatrix} 36.8 & 15.1 & 15.3 & -0.3 & -1.5 & 0.5 \\ 15.1 & 35.2 & 13.5 & -0.04 & -0.6 & 0.1 \\ 15.3 & 13.5 & 30.9 & -0.1 & -1 & 0.5 \\ -0.3 & -0.04 & -0.1 & 9.5 & -0.05 & -0.3 \\ -1.5 & -0.6 & -1 & -0.05 & 9.2 & -0.07 \\ 0.5 & 0.1 & 0.5 & -0.3 & -0.07 & 10.2 \end{bmatrix}$$

And the inverted locations are shown in Figure 3.10.

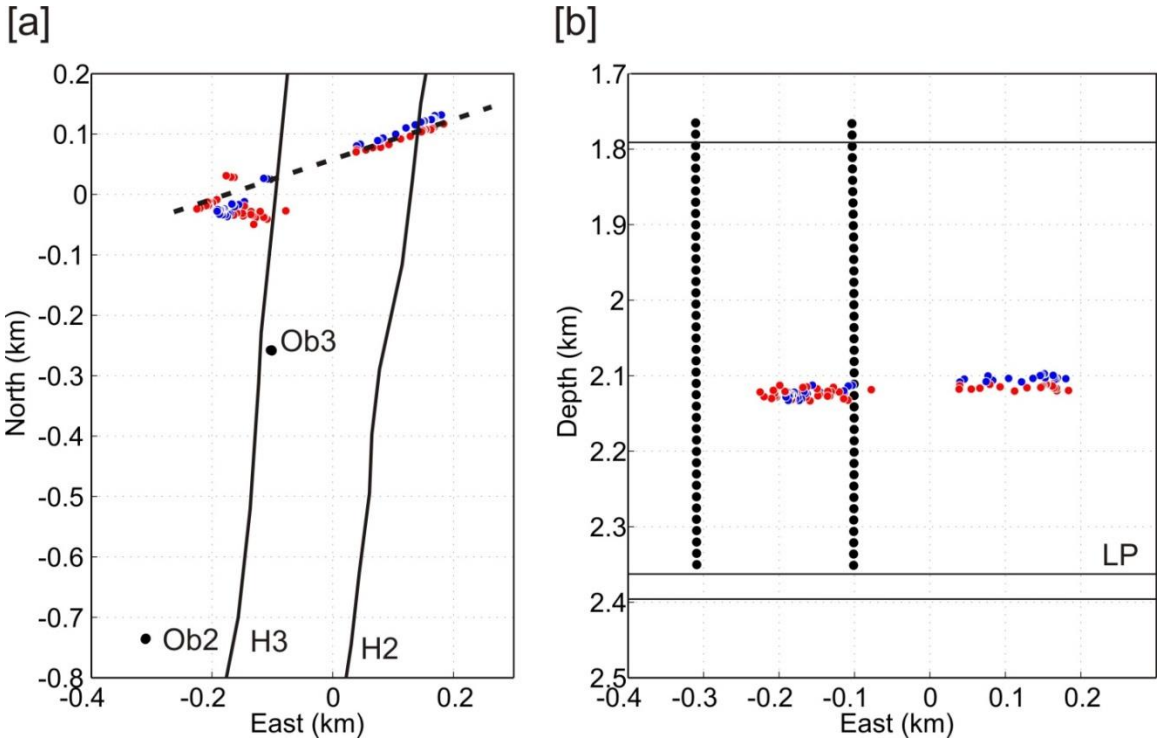

Figure 3.10: Comparison of the inverted results (blue dots) from an orthorhombic model and the locations that are located using an isotropic model (red dots) in map [a] and east-depth [b] views. The black dashed line represents the fast direction of azimuthal anisotropy from the inversion. Black solid lines in [a] indicate horizontal treatment wells (H2 and H3). Black dots in [a] are two observations wells (Ob2 and Ob3). LP stands for the effective formation that combines the Mission Canyon and Lodgepole formations. Black dots in [b] are receivers at two vertical arrays.

3.3 Discussion

The event locations from the anisotropic inversion are shifted relative to those from the isotropic inversion (Figure 3.10). After including a low-symmetry anisotropy model, the events' cloud becomes more concentrated and linear in map view (Figure 3.10 [a]). The west part of the cloud shifts slightly northward while the east part of the cloud moves southward. In depth view (Figure 3.10 [b]), the east part of the cloud becomes slightly shallower. The average change of event locations is 31 m relative to those from the isotropic inversion. The different results between the west and east clouds could indicate lateral variations in the anisotropic velocity structure. The west part is close to treatment well H3 where fracturing simulation was done before at well H2. Newly triggered fractures near H3 probably cause the structure in the west part more anisotropic, which explains the large differences of event locations between the isotropic and anisotropic inversion. The linearity of the new event cloud suggests that the anisotropic velocity model is more realistic than the isotropic model, especially in the west part. The results are also more meaningful in geology because the ENE-WSW alignment of microseismic events agrees with the pre-existing natural fractures in the area (Yang and Zoback, 2014). The azimuth of the fast axis (α) is 18° from east to north, consistent with the striking direction of the fractures. The dipping angle of the horizontal symmetry plane (β) is 15°. Although the core data (Figure 3.11) do not indicate dipping layers (Grechka and Yaskevich, 2014), they do show low-angle fractures and dikes. In addition, the dipping angle from the inversion could be caused by 3-D heterogeneous anisotropic structure.

According to the inverted stiffness matrix of LP formation, we found C_{11} and C_{44} are very close to C_{22} and C_{55}, respectively, which means that the LP is close to a VTI medium. In general, anisotropy can be caused by layering, fractures, or mineral alignment (Wuestefeld *et al*., 2010). The anisotropy in the LP is probably caused by numerous near vertical fractures in this formation, as suggested by Grechka and Yaskevich (2014). The trend of dominant faults interpreted from event locations in this study is E21°N, which is highly consistent with the azimuth of the fast axis α (E18°N) from our inversion. This agreement confirms that weak azimuthal anisotropy in the LP formation is caused by the presence of abundant natural cracks.

We also performed another inversion by assuming the LP is an effective VTI layer. In this case, only five independent elastic coefficients are needed to represent the medium. The data and the GA inversion setup are the same as the inversion with the orthorhombic anisotropy model. The inverted model can be expressed by anisotropy parameters: $V_p = 5.7km/s$, $V_s = 2.8km/s$, $\varepsilon = 0.048$, $\delta = -0.060$, and $\gamma = 0.146$. We compared this VTI model with that constrained using P-wave data through VSP analysis (Huang, 2016) (Table 2). Huang (2016) obtained the parameters in the Mission Canyon and Lodgepole formation separately, which cannot be directly compared with our effective model for the two layers. If we simply average out the parameters in the two layers given by Huang (2016), the anisotropic parameters are $V_p = 5.8km/s$, $\varepsilon = 0.048$ and $\delta = -0.050$. Considering the differences in data, methods, and the actual areas sampled by the data, the results from the two studies are amazingly consistent. The average event movement is

only 9 m from those obtained from an orthorhombic model, confirming that the LP is a near VTI medium.

Figure 3.11: Core Sample of Lodgepole formation. Clear low-angle fractures can be observed (Grechka and Yaskevich, 2014).

Table 3.1: P-wave velocity and Thomsen parameters of the effective LP layer from this study and those in the Mission Canyon and Lodgepole layers from Huang (2016) using VSP data.

	LP	Mission Canyon	Lodgepole
$V_p\,(km/s)$	5.70	5.85	5.67
ε	0.048	0.009	0.087
δ	-0.060	-0.085	-0.014

There is another interesting finding in this data analysis. We recognized mainly two types of events from the used stages in this test. They first type of events occur above the treatment well. Their depths correspond roughly to the middle of the monitoring wells (Figure 3.10). Abundant S-wave-splitting data are from these events. The other events occurred at or near the depth of the treatment wells. An example of waveforms from one of these events is shown in Figure 3.12. These earliest arriving traces are at or below the deepest geophones in each array. No obvious S-wave-splitting is observed from these events (Vertical component signals arrival later than horizontal signals in this case). This could be caused by multi-split S-waves. In this case, because the majority of ray paths penetrate only an effective near VTI medium, seismic waves of these events largely propagate along the near vertical symmetry axis of this medium and therefore do not produce S-wave splitting.

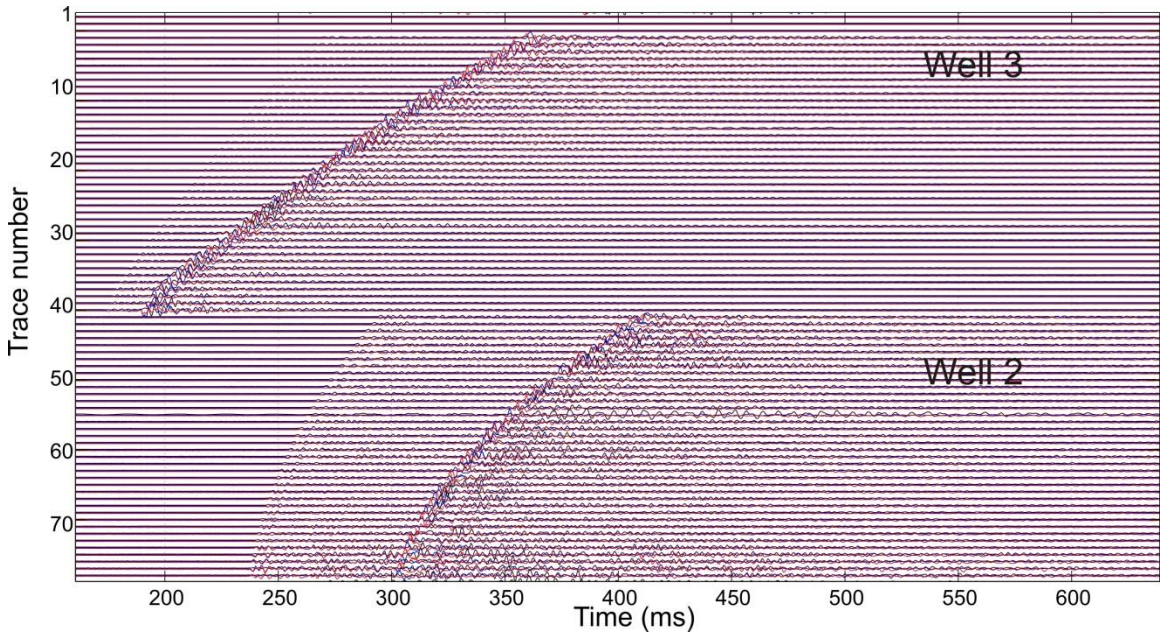

Figure 3.12: Waveforms recorded at well 2 and well 3 from one microseismic event occurring at or near the treatment wells.

3.4 Conclusion

In this chapter, we apply the joint inversion method using S-wave splitting data to real microseismic data from the Bakken Shale provided by Hess Corporation. The most important findings are the following:

(1) Full S-wave-splitting parameters are measured and utilized in this chapter. Adding S-wave-splitting parameters is helpful to constrain low-symmetry anisotropic velocity model. We successfully inverted an anisotropic velocity model of the Lodgepole formation using two monitoring wells and 49 events.

(2) The inverted velocity model of the Lodgepole formation is a near VTI medium. The obtained azimuth anisotropy and the alignment of microseismic events agree with the extension of the natural fractures in the formation.

(3) Events at or near the treatment wells do not present obvious S-wave splitting. This is probably caused by near-vertical ray paths that are largely parallel to the symmetry axis.

4 Chapter 4

Determination of Microseismic Event Azimuth from S-Wave Splitting Analysis - Methodology and synthetic Test

4.1 Introduction

Hydraulic fracturing is one of the most important techniques to enhance oil and gas production, especially for unconventional reservoirs. This process generates fractures and microseismic events. Microseismic monitoring is an effective tool that images the spatial and temporal variations of fractures by locating microseismic events. It is well known that event locations are heavily influenced by many elements, including data acquisition geometry (Maxwell *et al*., 2010), velocity model building (e.g. Gajewski *et al*., 2009; Grechka *et al*., 2011; Grechka and Yaskevich, 2013; Li *et al*., 2013, 2014), and the quality of arrival-time picking (Juan and Danilo, 2013). Event azimuth determination, which also affects event locations especially for single-well monitoring survey, has seldom been discussed in microseismic studies.

Many downhole microseismic surveys have deployed sensors in a single well due to a relatively low cost. One issue with single-well monitoring is that event locations cannot be determined by P- and S-wave travel times alone. Additional incoming azimuth information is required to locate microseismic events. Usually, this angle is obtained from a P-wave hodogram. However, a microseismic source often emits much weaker P-wave energy

than S-wave. Weak P-wave arrivals increase the uncertainty of polarization determination and affect location accuracy. On the other hand, S-wave can be much more easily and precisely detected due to its large amplitude. Therefore, it would be tremendously useful if microseismic event azimuths could be determined from S-waves. However, the incoming ray direction, which is perpendicular to the S-wave polarization direction, cannot be uniquely determined from S-wave hodogram analysis because it defines a plane normal to the particle motion instead of a single direction. In addition, the presence of seismic anisotropy, which is common for microseismic surveys (e.g. Vernik and Liu, 1997; Gajewski *et al*., 2009), usually causes elliptical S-wave particle motions in the horizontal plane. Hodogram analysis directly on S-wave phases is usually not considered in routine microseismic data processing.

S-wave-splitting, probably the strongest indicator of seismic anisotropy, has been observed in microseismic data and utilized by some studies to interpret fractures sets (Verdon *et al*., 2009; Verdon and Kendall, 2011) and to do microseismic velocity model building (Grechka *et al*., 2014). In this paper, we use the measurements of full S-wave-splitting parameters (the fast S-wave polarization angle (ϕ) and time lag of the slow S-wave (δt)) from microseismic data to identify event azimuths. The effectiveness of S-wave-splitting measurements depends on the accuracy of coordinate rotation from the geographic system to a ray-based system that is determined by ray azimuth and inclination. After two-dimensional (2D) microseismic locating, ray inclination is obtained at each receiver. Then the coordinate rotation only depends on ray azimuth. A grid search on event azimuth is conducted to find the optimal value that gives the smallest

measurement uncertainty. We applied this method to synthetic waveforms with two different noise levels and successfully recovered the true azimuths in both cases. We further demonstrated the effectiveness of this method using microseismic data from the Bakken field.

4.2 Method

There are two steps for microseismic S-wave splitting data preparation (Wuestefeld *et al*., 2010). The first step is the coordinate rotation, to maximize the S-wave energy in the splitting analysis (Teanby *et al*., 2004). The windowed S-wave traces of north, east, and vertical components in the geographical coordinate system are rotated to the components in a ray-frame coordinate system (Figure 4.1), in which three axes consists of the P-wave polarization (L), transverse (T), and radial direction (Q). The rotation uses the following transformation matrix (Plesinger *et al*., 1986)

$$M_{3D} = \begin{bmatrix} \cos(i) & -\sin(i)\sin(\theta) & -\sin(\theta)\cos(\theta) \\ \sin(i) & \cos(i)\sin(\theta) & \cos(i)\cos(\theta) \\ 0 & -\cos(\theta) & \sin(\theta) \end{bmatrix} \tag{4.1}$$

where i is the inclination angle of the ray and θ is the back-azimuth of the event. Then a grid search method is performed to find the splitting parameters. For each pair of (ϕ, δt), T and Q are rotated by ϕ and one component is lagged by δt. The rotated components are used to form a cross correlation matrix

$$\begin{bmatrix} C_{QQ} & C_{QT} \\ C_{TQ} & C_{TT} \end{bmatrix} \tag{4.2}$$

At the true value of (ϕ , δt), the cross correlation matrix resembles an isotropic case and has one zero eigenvalue, which is defined as singular. Due to the existence of noise, the pair of ϕ and δt that can minimize the second eigenvalue λ_2 of the corresponding cross correlation matrix, is considered to be the optimized measurement. An *F*-test is used to contour a 95% confidence region that satisfies

$$\frac{\lambda_2}{\min(\lambda_2)} \leq 1 + \frac{k}{v-k} f_{k,k-v}(1-\beta) \tag{4.3}$$

where β = 0.05, k = 2, and v is calculated according to the noise level and the number of samples of the windowed traces (Silver and Chan, 1991). The range of this confidence region defines two times of standard errors of S-wave splitting parameters (E_ϕ and $E_{\delta t}$).

Besides noise level (Silver and Chan, 1991) and window length (Teanby *et al*. 2004), for microseismic data, we have found that the errors of S-wave-splitting measurements also relate heavily to the coordinate rotation. Ray inclination can be determined by 2D event locating using travel time data even when P-wave polarization is not reliable. Then ray azimuth becomes the only unknown parameter that affects the coordinate rotation. Figure 4.2 shows that a wrong azimuth can affect energy distribution in Q and T components. This energy redistribution changes the effectiveness of the S-wave-splitting measurements. The more accurate the event azimuth is, the smaller the measurement uncertainties (E_ϕ and $E_{\delta t}$). We will return to demonstrate this in the next section.

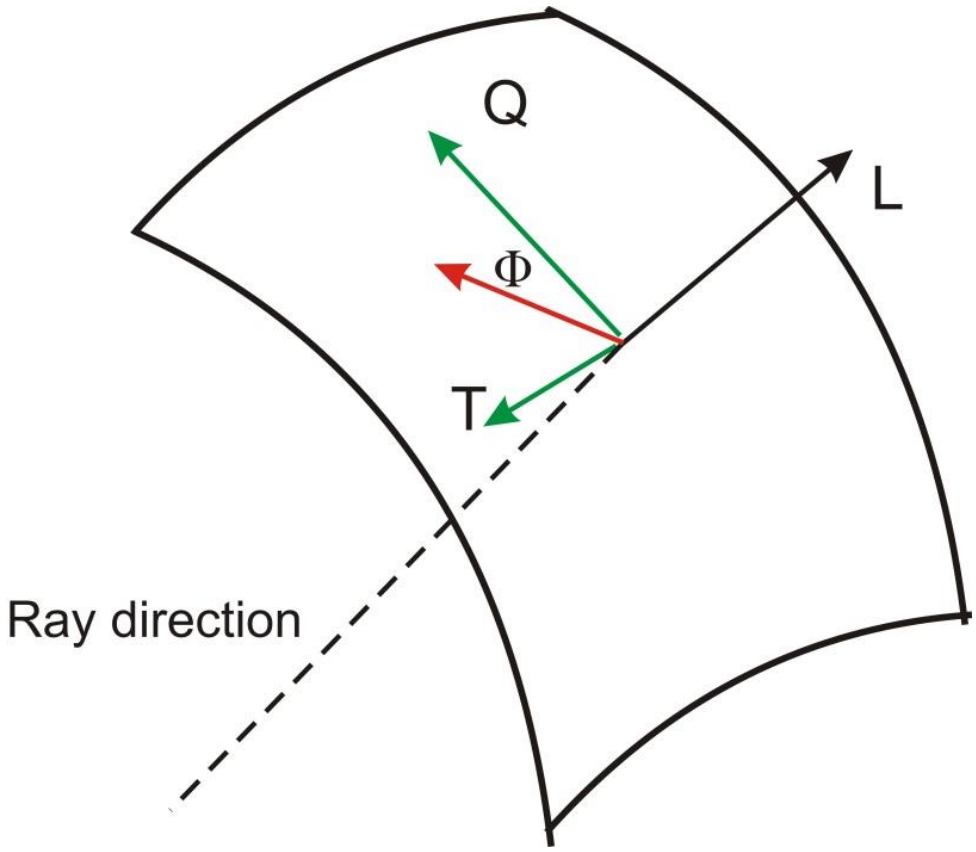

Figure 4.1: Map of a ray coordinate system. Three positive axes are the wave front (L), transverse (T), and radial (Q) direction. Red lines represent fast S-wave polarization in the T-Q plane. The fast S-wave polarization angle, Φ, is relative to radial direction Q.

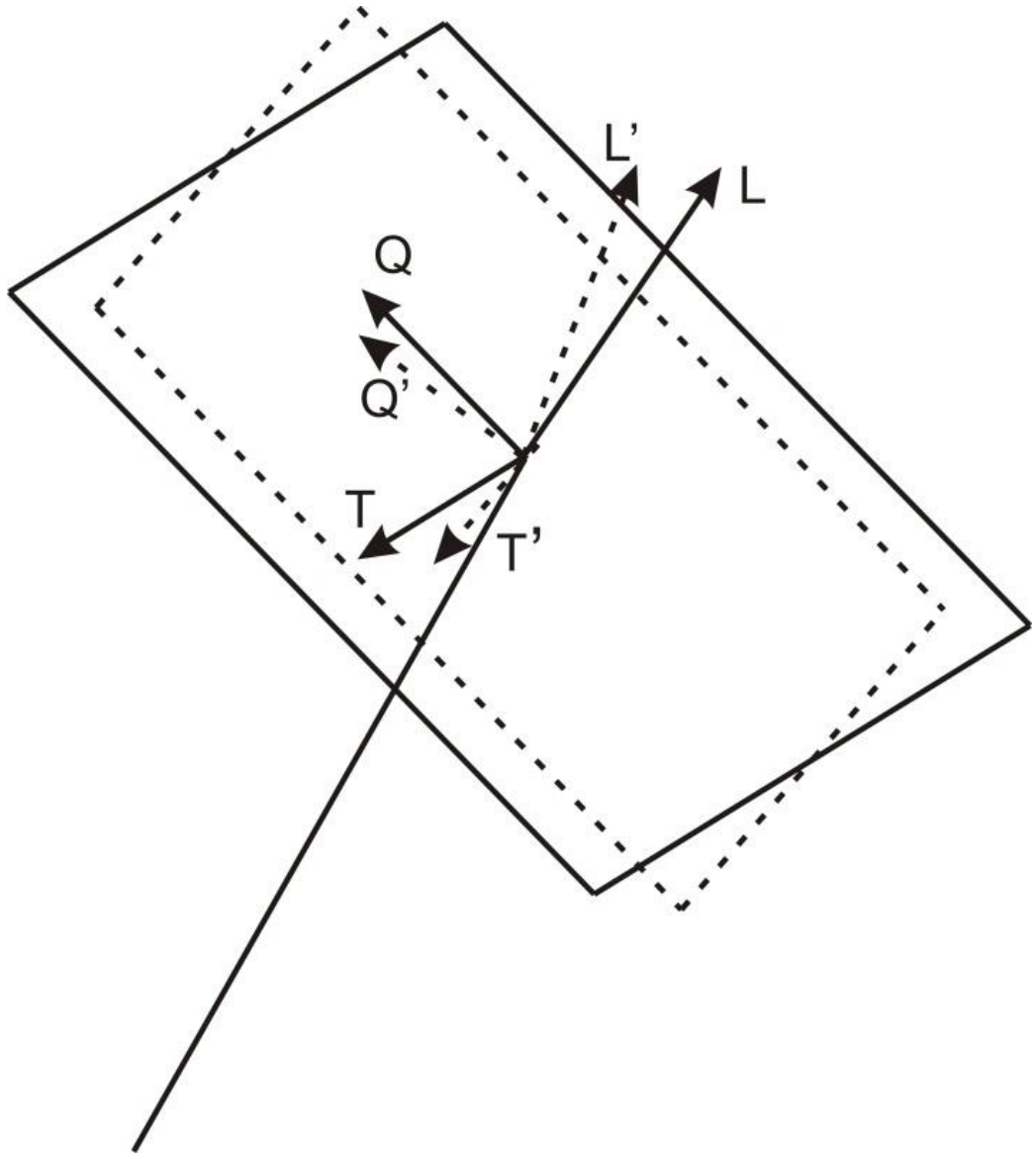

Figure 4.2: Example of ray-frame coordinates. L is the true ray direction; Q and T are radial and transverse components, respectively. L' is the ray direction for a wrong event azimuth and Q' and T' are corresponding radial and transverse components, respectively.

Once understood, we now can utilize S-wave splitting analysis to determine event azimuths. First, we locate a microseismic event in a 2D domain using S-wave and/or P-wave travel times. Numerous techniques are available to do 2D microseismic locating (e.g. Bardainne *et al*., 2009; Fuller *et al*., 2007; Geiger 1912). We apply a typical grid search method in this study. The calculated travel times and chosen arrival times of P-waves and fast S-waves are represented by t_i^j and T_i^j, respectively. We search for radial distances and the depths of events that can minimize the objective function below:

$$Obj = \sigma(t_i^j - T_i^j) \tag{4.4}$$

Where i is event index, j is receiver index, and σ represents the standard deviation of the function. This objective function avoids the need to consider the origin time τ_0. At the true event location, the objective function should be a vector with constant value τ_0. This is characterized by the smallest standard deviation. After obtaining the radial distance R and depth of an event Z, the inclinations of the event can be calculated for each receiver. The event azimuth is needed to fully determine the event location that is described by

$$\left[R_i \cos(\alpha_i), R_i \sin(\alpha_i), Z_i\right] \tag{4.5}$$

Second, we determined the event azimuth from S-wave-splitting analysis after finding ray inclinations from the 2D locations. Seismic traces with clear S-wave-splitting were selected and windowed. Following the method described above, we applied a grid search

to find the best event azimuth that gave the smallest measurement errors. The azimuth at each search is defined by

$$\alpha = \alpha_{beg} + (i-1)\Delta\alpha \tag{4.6}$$

where i is the search step and $\Delta\alpha$ is the search interval. For each azimuth, the total errors of all measurements were formed by the summation of the errors of all selected receivers (N)

$$\begin{aligned} E_{\phi}^{\alpha} &= \sum_{n=1}^{N} {}^{n}E_{\phi}^{\alpha} \\ E_{\delta t}^{\alpha} &= \sum_{n=1}^{N} {}^{n}E_{\delta t}^{\alpha} \end{aligned} \tag{4.7}$$

We normalize these two vectors with different units and sum them together to form the objective function as shown below.

$$\begin{aligned} \tilde{E}_{f}^{a} &= \frac{E_{f}^{a} - \min(E_{f}^{a})}{\max(E_{f}^{a}) - \min(E_{f}^{a})} \\ \tilde{E}_{dt}^{a} &= \frac{E_{dt}^{a} - \min(E_{dt}^{a})}{\max(E_{dt}^{a}) - \min(E_{dt}^{a})} \end{aligned} \tag{4.8}$$

$$E^{a} = \tilde{E}_{f}^{a} + \tilde{E}_{dt}^{a} \tag{4.9}$$

$\tilde{E}_{f}^{a}$ and $\tilde{E}_{dt}^{a}$ are normalized ϕ and δt errors for a given azimuth. The azimuth corresponding with the smallest final error (E^{α}) was selected as the most optimized value. However, it is necessary to add additional thresholds to remove poor measurements. When the optimized errors of certain receivers that exceeded this threshold, the measurements from these receivers were considered unreliable and were

not used in calculating the objective function. The number of thresholds should change according to the quality of microseismic data.

4.3 Synthetic test

Before applying this method to real field data, we used synthetic examples to understand it better. The data acquisition geometry is displayed in Figure 4.3. One vertical array consisting of 15 receivers was set at the depths of 400 m to 975 m. Its surface location was at x = 100 m and y = 180 m, where x represents the east and y is north. A synthetic event was located at $x = y = 0$ m with a back-azimuth 29° from north to east. We assigned a magnitude of -2.5 and assumed a double-couple source with a vertical fault plane. A VTI anisotropic medium was used with the following anisotropy parameters V_{p0} = 3 km/s, V_{s0} = 1.8 km/s, ε = 0.12, δ = 0.05, and γ = 0.15. In a VTI medium, the fast S-wave (SH wave) should polarize along T and slow S-wave (SV wave) should polarize along Q (Figure 4.2).

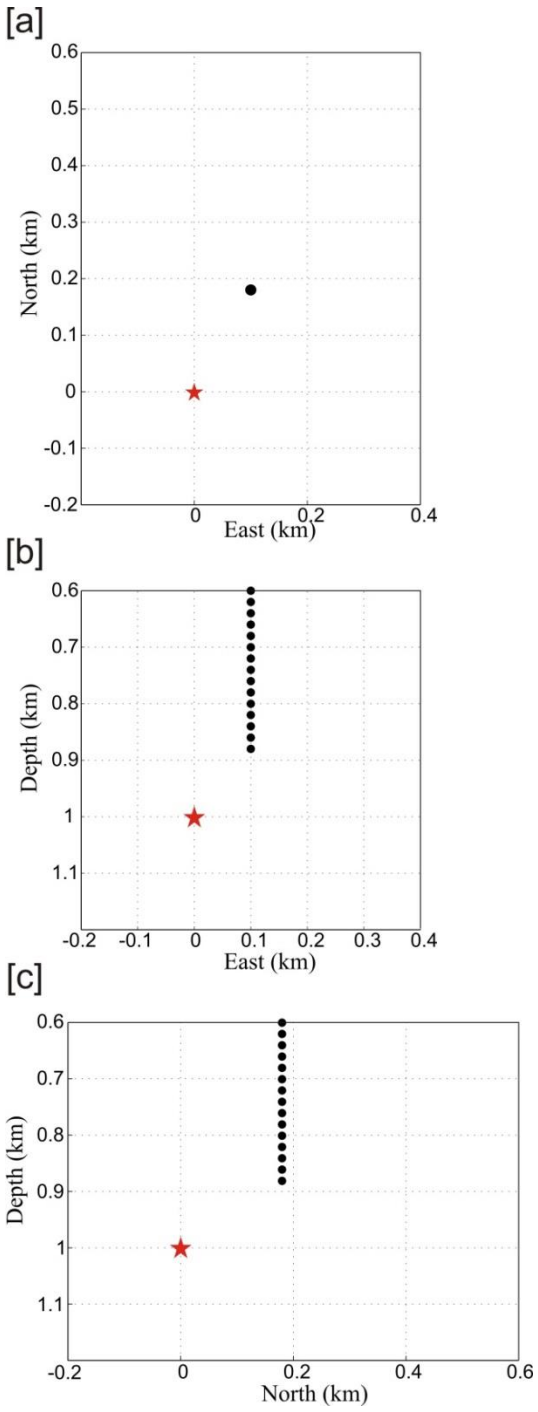

Figure 4.3: Geometry of data acquisition in map view [a] and two depth views [b, c]. Black dots are receivers and the red star is the true event location.

4.3.1 Low Noise Case

Synthetic waveforms were generated using the pseudo-spectral approach described by Hung and Forsyth (1998). To simulate realistic noisy microseismic data, we added random noises (10 dBW) to the synthetic traces (Figure 4.4). P-waves at all receivers are characterized by poor SNR (<3.5) although the trend of P-wave arrivals can be recognized. In contrast, S-wave arrivals are relatively clear due to the double-couple focal mechanism. Only the bottom several receivers present obvious S-wave splitting.

Following the method described above, the first procedure is to locate a microseismic event in the 2D domain. We manually picked clear P-wave and fast S-wave arrival times that are represented by green bars in Figure 4.4. The grid search method was used to minimize the objective function (Equation 4.9) assuming a grid size of 1 m (Figure 4.5). After obtaining the location, the inclination angle was calculated for each receiver. Without knowledge of the event azimuth, the potential event location could be any point on the circle that is centered at the receiver array with a radius determined by the 2D locating (Figure 4.6). It is clear that event azimuth is needed to pinpoint the event location.

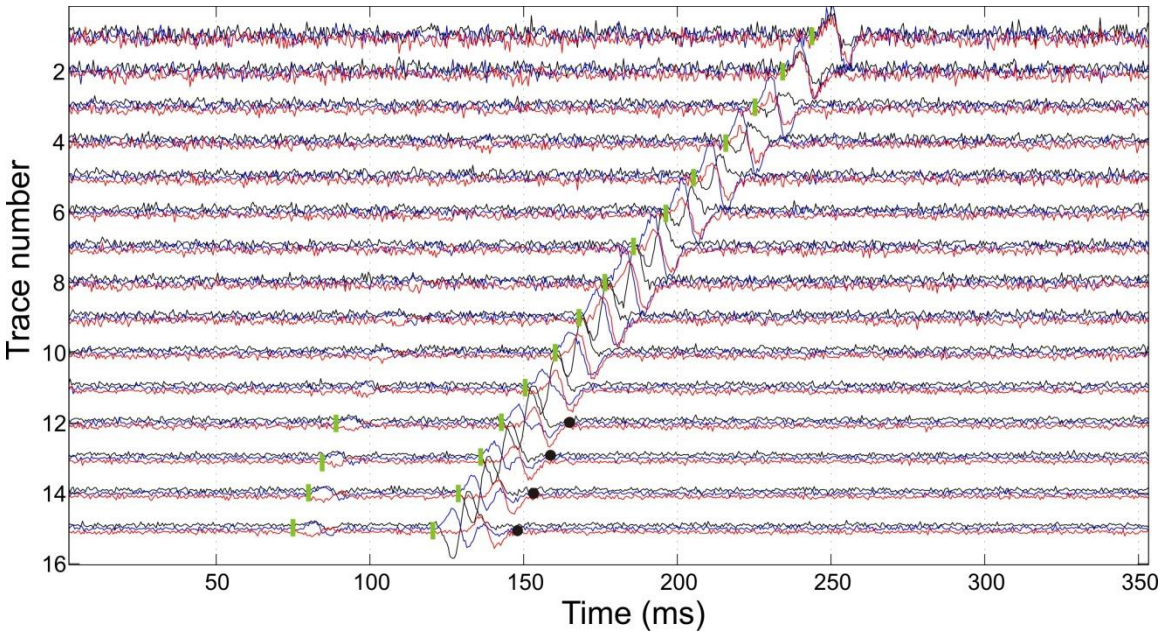

Figure 4.4: Three components of synthetic seismograms with low-level noise. Green bars and black dots are manually picked P-wave and S-wave arrival times. Black dots are manually picked S-wave splitting analysis ending window.

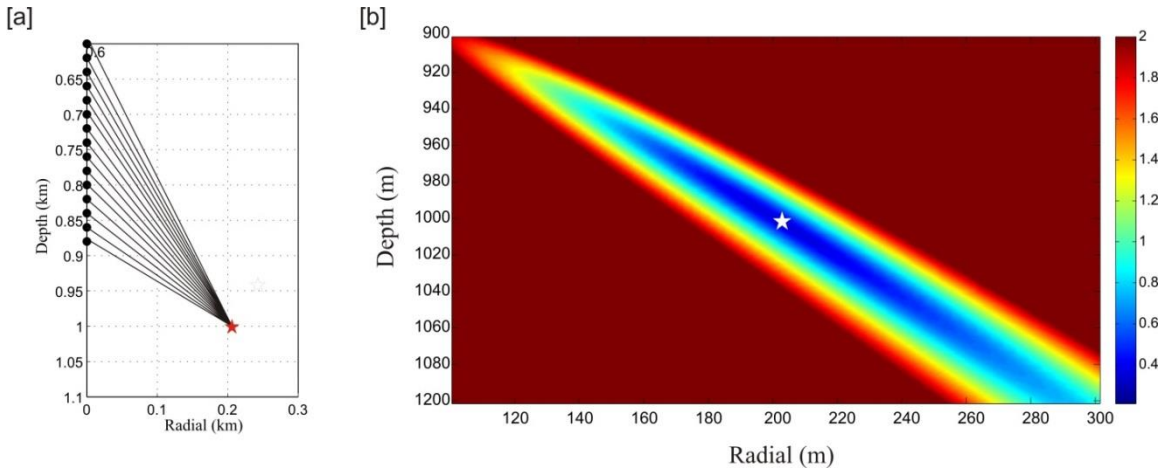

Figure 4.5: Ray paths [a] and residual distribution [b] of 2D locating. White star is the located event. Color here represents the value of objective function (Equation 4.4).

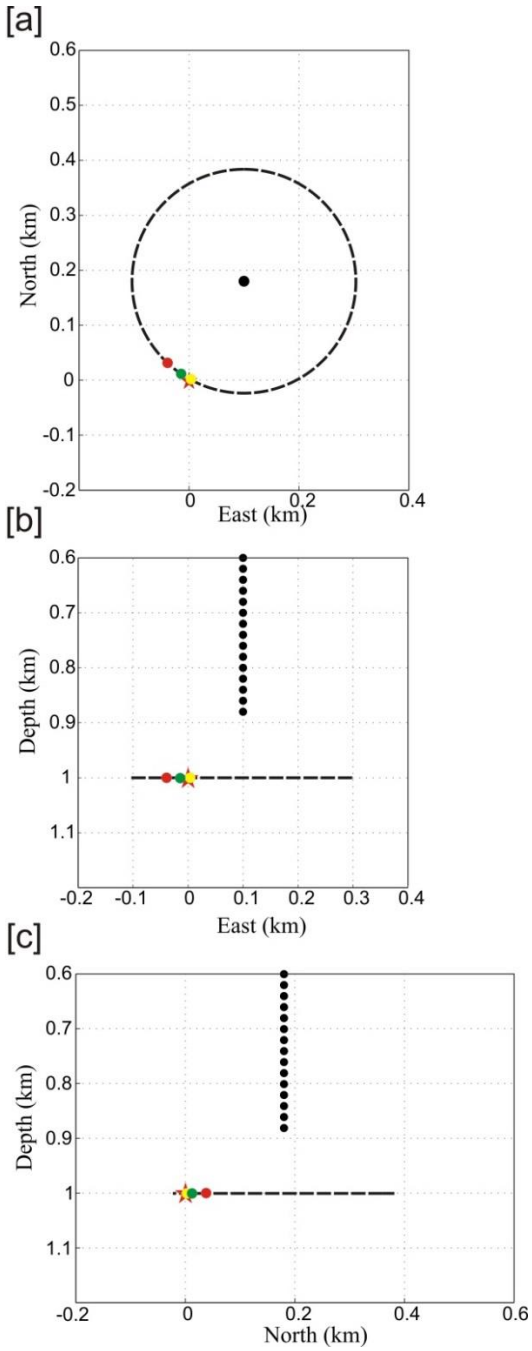

Figure 4.6: Geometry of data acquisition in map view [a] and two depth views [b, c]. Black dots are receivers and the red star is true event location. Dashed lines represent potential locations after 2D locating. Red and yellow dots are locations inverted from low-level noisy data from P-wave polarization method and S-wave-splitting analysis, respectively. Green dot is the location inverted from high-level noisy data from S-wave-splitting data.

Before applying this method, we first tested whether the effectiveness of S-wave splitting measurements is positively correlated with the accuracy of coordinate rotation. We rotated data at receiver 12 to ray coordinates with a true inclination and three azimuths: 30°, 50°, and 70°. Figure 4.7 illustrates how the change in azimuth can affect recorded waveforms in Q and T components. Obviously, when rotation azimuth is 30°, which is almost the true azimuth (29°), T records the fast S wave only, and Q records the slow S-wave (Figure 4.7[a]). When using the other two azimuths, waveforms in Q and T are formed by both fast and slow S-waves (Figure 4.7[b] and [c]). The amplitude in the T component becomes smaller when the rotation azimuth is different from the true value, which makes the splitting measurement less effective as shown below. S-wave-splitting parameters were measured for each rotation. The distributions of the 2nd eigenvalue of the cross-correlation matrix, which is defined by $\lambda_2 / \min(\lambda_2)$ for each pair of (ϕ, δt), are seen in Figure 4.8. Clearly, the energy redistribution in Q and T components (Figure 4.7) significantly affects the λ_2 gradient. The gradient of λ_2 near the minimum value is the largest at the azimuth of 30° and becomes smaller when the azimuth is farther away from the true azimuth. The determination of measurement uncertainty (E_ϕ and $E_{\delta t}$) (Equation 4.3) only relates to the window length and noise level, which are the same for all measurements. As seen in Figure 4.8, the gradient changes caused by coordinate rotation correlate well with the measurement uncertainty. The smallest error was obtained at the azimuth of 30° while the error became larger and larger at 50° and 70°. This result correctly predicts that S-wave-splitting measurements positively correlate with the accuracy of the event azimuth.

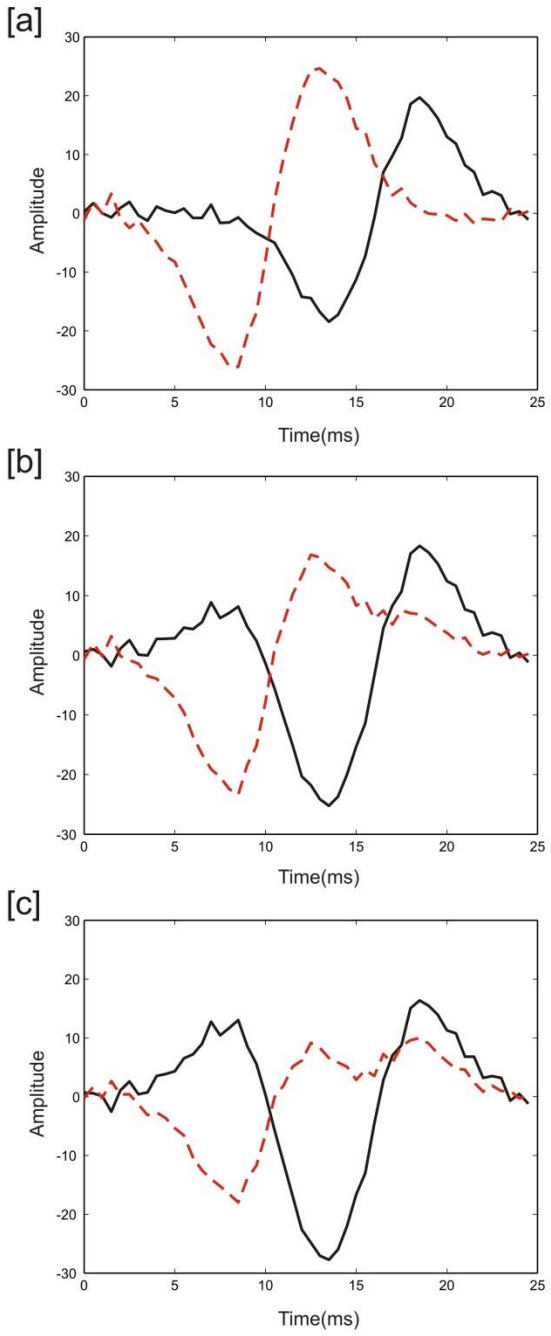

Figure 4.7: Recorded windowed T component seismogram (red dash) and Q component seismogram (black) after coordinate rotation using azimuth 30°[a], 50°[b], and 70°[c].

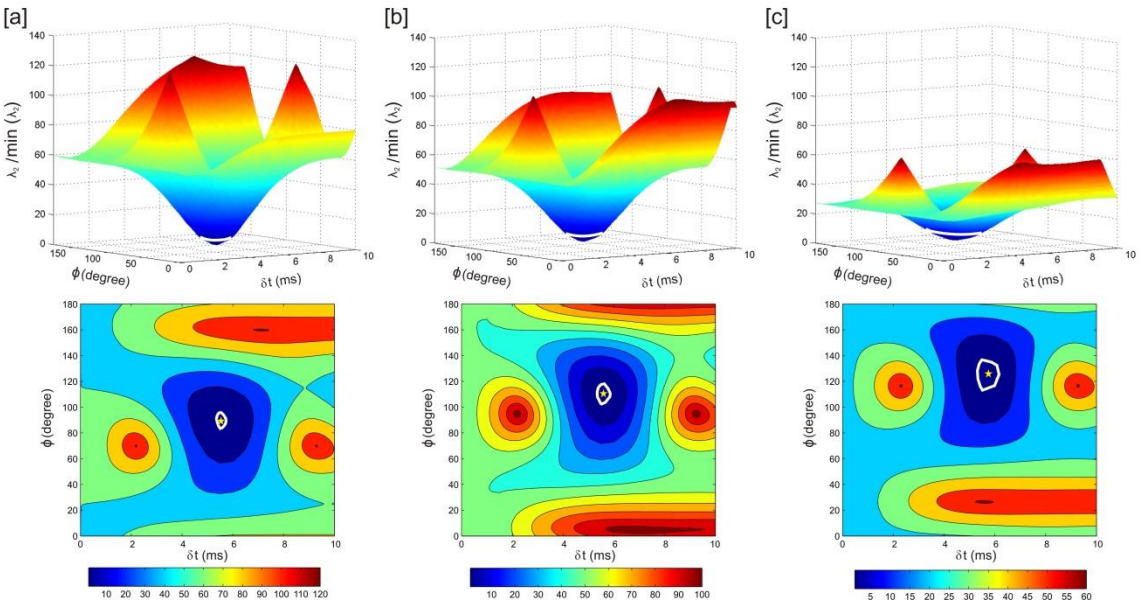

Figure 4.8: S-wave splitting measurement results and uncertainties (E_{ϕ} and $E_{\delta t}$) from rotation azimuth 30[a], 50[b], and 70[c]. Color here represents $\lambda_2 / \min(\lambda_2)$. Blue plane is 95% confidence region (equation 4.3). Thick white contours are measurement uncertainties and yellow stars represent measurement results.

Theoretically, the measured fast polarization direction should be 90° (from Q to T) in the ray coordinate for the given VTI medium. However, we notice that this true value is achieved only when using azimuth 30°, which is almost the true azimuth (29°). With an incorrect rotation azimuth, not only the measurement uncertainty will increase, but the measured S-wave splitting parameters will also be inaccurate. This probably is caused by the distorted waveforms due to incorrect rotation azimuth. For microseismic studies that include S-wave splitting measurements, coordinate rotation should be done carefully to avoid measurement errors.

We applied the proposed method to synthetic data at the four bottom receivers. S-waves are windowed from the arrival time of fast S wave and the end of the slow wave (Figure 4.4). We first chose the search range from -10° to 70° from north to east with an initial interval of 10°. It is inefficient to search the whole azimuth range with a small interval at the first try. The results are illustrated in Figure 4.9[a]. The optimal angle of 30° is characterized by the lowest measurement error, which is indicated as the red point in Figure 4.9[a]. However, the error separation is not significant between 20° and 40°. To refine the azimuth, we then used 2° as the interval for a new search from 20° to 40°. Figure 4.9[b] shows the results and the best-fit angle is 28°, only 1° from the true azimuth (29°), an error that is smaller than the search interval. Using this azimuth, the event was located almost at the true location (yellow dot in Figure 4.6).

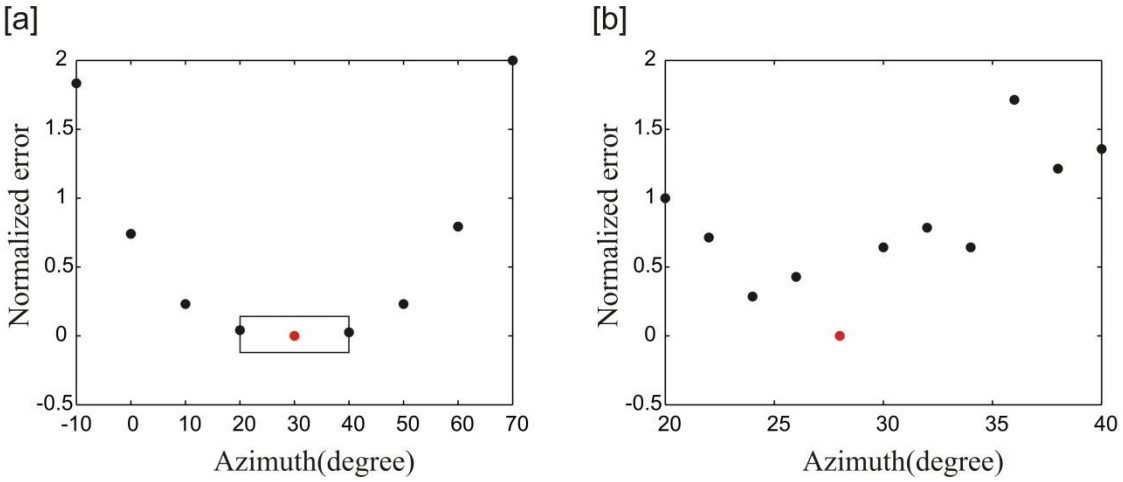

Figure 4.9: The distributions of normalized misfits for low-level-noise data with 10° searching interval [a] and 2° searching interval [b]. Red dots mark the azimuth that gives the smallest misfit.

As seen in Figure 4.10, it is clear that particle motions of P-waves are not as linear as expected due to noise contamination, which is a big obstacle for determining event azimuths from P-wave hodograms. Due to the effect of anisotropic media, S-wave particle motions present obvious elliptical shapes, which also prevents determining event azimuths from S-wave hodogram directly. The measurement results are shown in Table 4.1. As expected, the identified azimuths are highly unstable. If we used the mean value as the event azimuth, as shown by the red dot in Figure 4.6, a large location error (about 38 m) is resulted when using the azimuth determined by P-wave hodogram, which is much larger the error using S-wave splitting analysis. The success of this inversion confirmed the feasibility of estimating event azimuth from S-wave splitting in microseismic data.

Table 4.1: Determined event azimuth from P-wave particle motion analysis method.

Receiver Number	P-wave Hodogram (degree)
12	45
13	76
14	23
15	20
Average	41

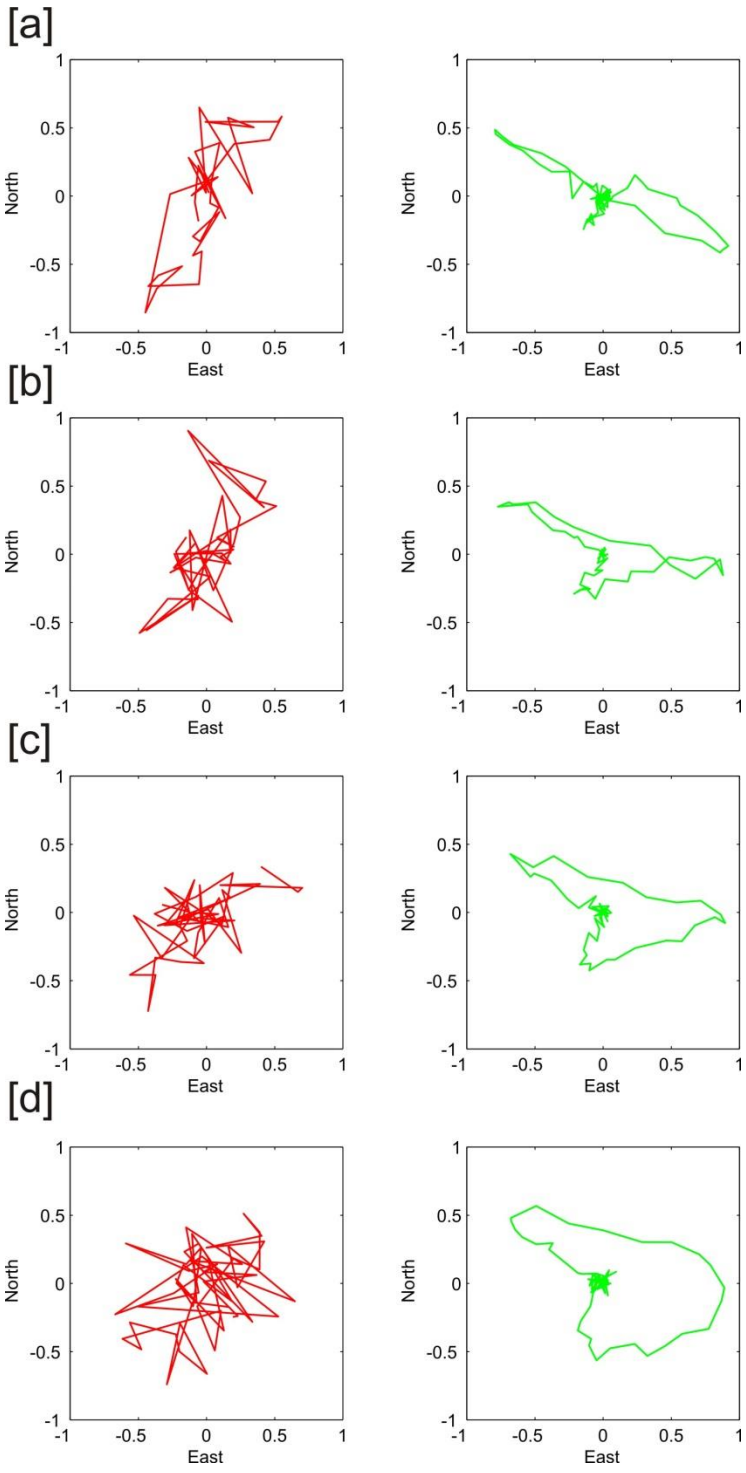

Figure 4.10: P-wave and S-wave particle motions in map view of receiver 12 [a], receiver 13 [b], receiver 14 [c], and receiver 15 [d].

4.3.2 High Noise Case

To test the robustness of the method for higher noise data, we tripled the noise level in the synthetic seismograms (Figure 4.11). The whole P-wave signals are completely buried in noise in this case, and it is impossible to obtain event azimuth from P-wave polarization analysis (Figure 4.13). The SNR of S-wave becomes 8. We ignored the effects of noise on 2D locating and took the same ray inclinations from the previous test. We then performed the same analyses as above to identify the event azimuth and show the results in Figure 4.12. The azimuth of 30° gives the smallest normalized error under the 10° search interval. With a finer search interval of 2°, the best-fit azimuth is 34°, yielding an error of 5° from the true event azimuth. Although this error is slightly larger than that from the low-noise data using the same method it is still better than that from P-wave data in the last test (Figure 4.6). Considering the absence of P-wave information in heavily contaminated microseismic data, the determined azimuth from S-wave-splitting analysis is invaluable. These experiments demonstrate the robustness of estimating event azimuth from S-wave splitting analysis, which is much less sensitive to noise than the P-wave polarization method.

.

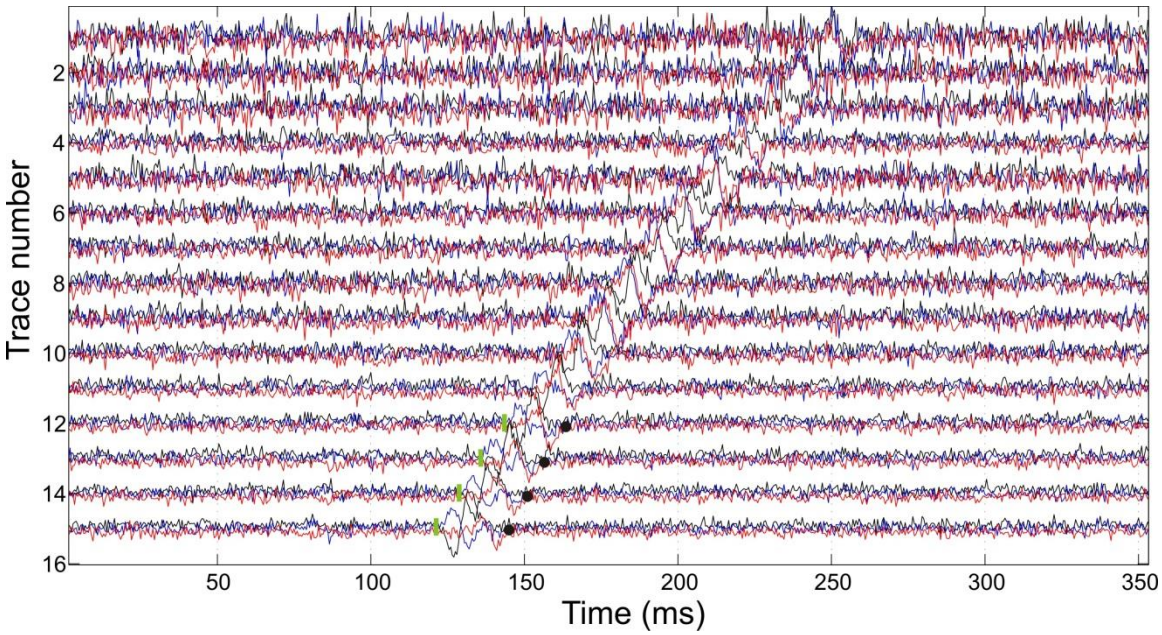

Figure 4.11: Synthetic seismograms with high-level noise. Green bars are manually picked S-wave arrival times. Black dots are manually picked S-wave splitting analysis ending window.

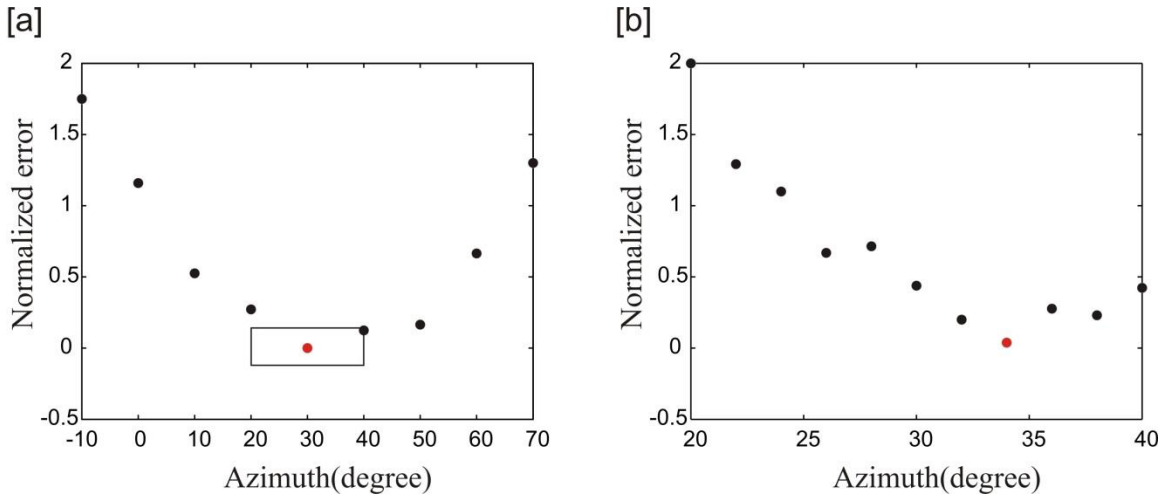

Figure 4.12: The distributions of normalized misfits for high-level-noise data with 10° searching interval [a] and 2° searching interval [b]. Red dots mark the azimuth that gives the smallest misfit.

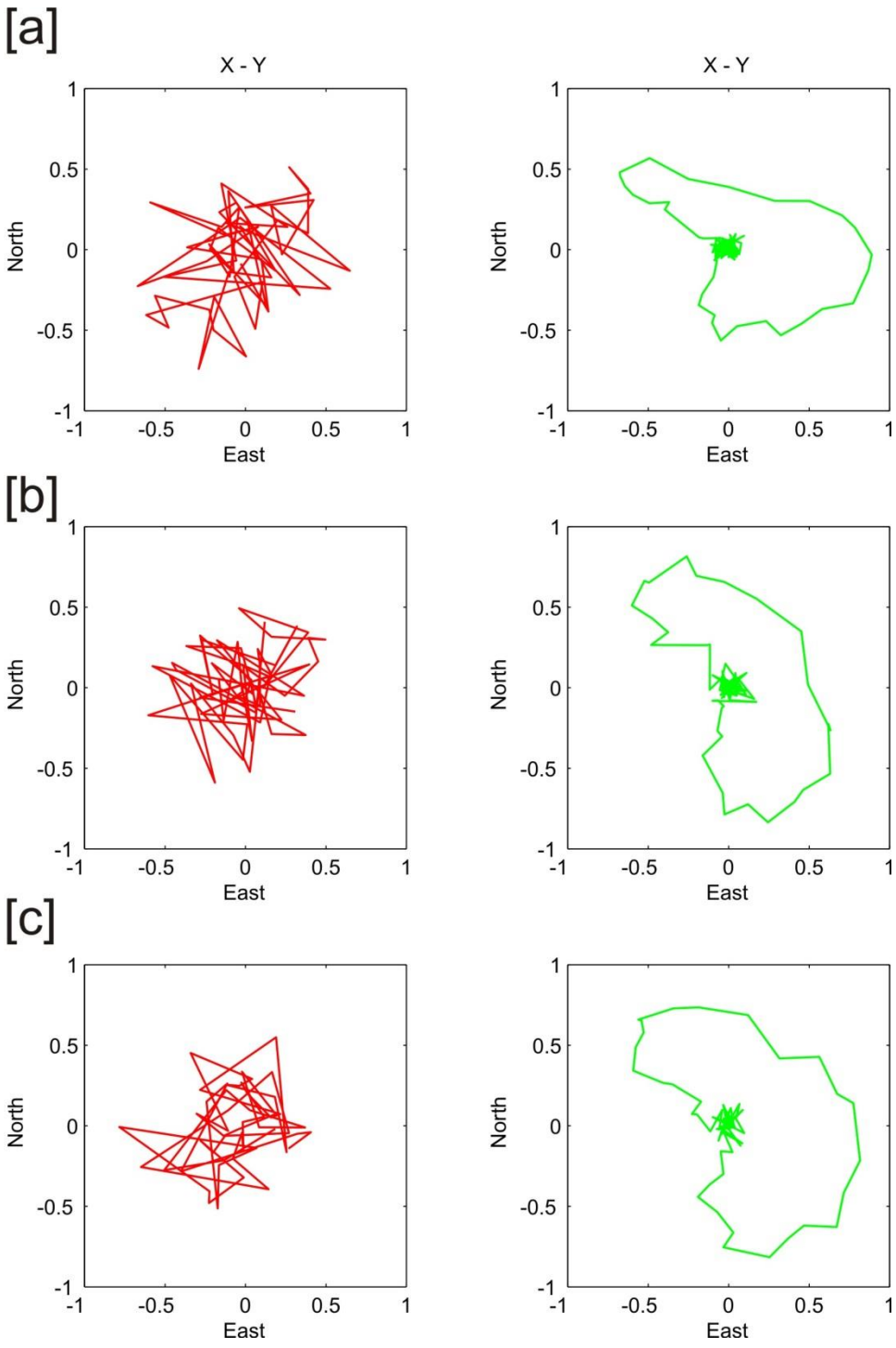

Figure 4.13: P-wave and S-wave particle motions in map view of receiver 12 [a], receiver 13 [b], receiver 14 [c].

4.4 Discussion

Conventional methods of event azimuth determination chiefly rely on P-wave information for single-well monitoring. However, for some microseismic datasets that have no or very weak P-wave signals, there is no standard means to obtain event azimuths. Even if P waves can be recognized for some events, as shown in our synthetic and field data tests, low SNR P-wave data can cause large uncertainties in measured event azimuth, which consequently produces large errors in microseismic event locations.

Our study evidences that S-wave splitting in microseismic data can be used to determine event azimuths. This approach has several advantages. The most important one is the ability to determine event azimuths from S waves, which are much stronger than P waves in typical microseismic data. In addition, our method is less sensitive to the influence of noise. In the synthetic tests, we showed that conventional P-wave polarization analysis suffered large uncertainty problems for noisy data while our method can reliably estimate event azimuths with enough accuracy. Even when P-wave energy is completely absent, this method still provides a reasonable solution for event azimuth.

The efficiency of the S-wave splitting method is affected by the search range and search interval of the azimuth. A large search range allows good azimuthal coverage but increases the computation time. In practice, *a priori* knowledge, such as pre-located events or the locations of perforation shots, would be helpful to narrow down the azimuth search range and to decrease computation time. For the choice of search interval, we suggest using a multi-step strategy by decreasing the value gradually in each step. From

our experience, an interval of 5° is reasonable for real data cases. Too small intervals (1-2°) will not only increase computation time but also improve the difficulty in uniquely determining the azimuth because the misfits at several neighboring angles may not be significantly different. The acceptable error from our method is less than 5° for event azimuth, which is smaller than the error of 10° that is accepted for using P-wave polarization analysis (empirical value provided by a vendor).

Our method using S-wave-splitting data requires determining the inclination angle of the incoming ray, which can be done by 2D location using P- and S-wave arrivals. The errors in the 2D location can affect the inclination angle, which could theoretically cause errors in azimuth determination. However, this error caused by the uncertainty of inclination must be small since the resulting azimuths for real data agree reasonably well with results from using more advanced location method. One obvious limitation of our method is that it cannot work without S-wave splitting data. However, given the general VTI structure in layered sediment rocks (Thomsen, 1986) and downhole monitoring in microseismic acquisition, S-wave splitting is common in microseismic data (Grechka *et al*., 2014; Verdon *et al*., 2009, 2011). Although it might be hard to measure split S-waves at all receivers, it is possible to identify splitting at some receivers for some events. Based on the advantages and limitations of the S-wave splitting method, we recommend using it to determine event azimuth only when the P-wave data are not reliable. This method significantly helps to increase the number of locatable events for single-well monitoring.

4.5 Conclusion

We proposed a new method that determines the azimuths of microseismic events from S-wave-splitting analysis. We have tested the reliability of this method using synthetic microseismic data and found that the method is less sensitive to noise than P-wave polarization analysis. It requires knowing ray inclinations from 2D event locations and the presence of S-wave splitting in microseismic data. The most important feature of this method is that it utilizes only S waves, which are often stronger than P-waves in microseismic data. Our method provides a new way to estimate event azimuth and helps to improve the locations of many events, especially those have weak or noisy P waves.

5 Chapter 5

Determination of Microseismic Event Azimuth from S-Wave Splitting Analysis – Implementation with Field Data

5.1 Introduction

In chapter 4, we discussed the methodology of determining microseismic event azimuths based on S-wave splitting analysis in microseismic data and tested the method using synthetic data. The synthetic tests suggested that the method is feasible for determining event azimuths without the need of P-wave signals. It can give reliable results even for heavily contaminated data. In this chapter, we applied this method to real field data in the Bakken reservoir.

The dataset used in this chapter are from the Bakken reservoir, which is provided by the Hess Corporation and is the same as that discussed in chapter 3. The Bakken formation is a thin shale reservoir overlaid by a thick limestone caprock called Lodegpole (LP). The microseismic data were recorded by six vertical monitoring wells originally (Ob #1, #2, #3, #4, #5 and #6) and five of them (OB # 1-5) were located in the LP. To simulate the single well case, only Ob well 3 (Figure 5.1) was utilized for this test.

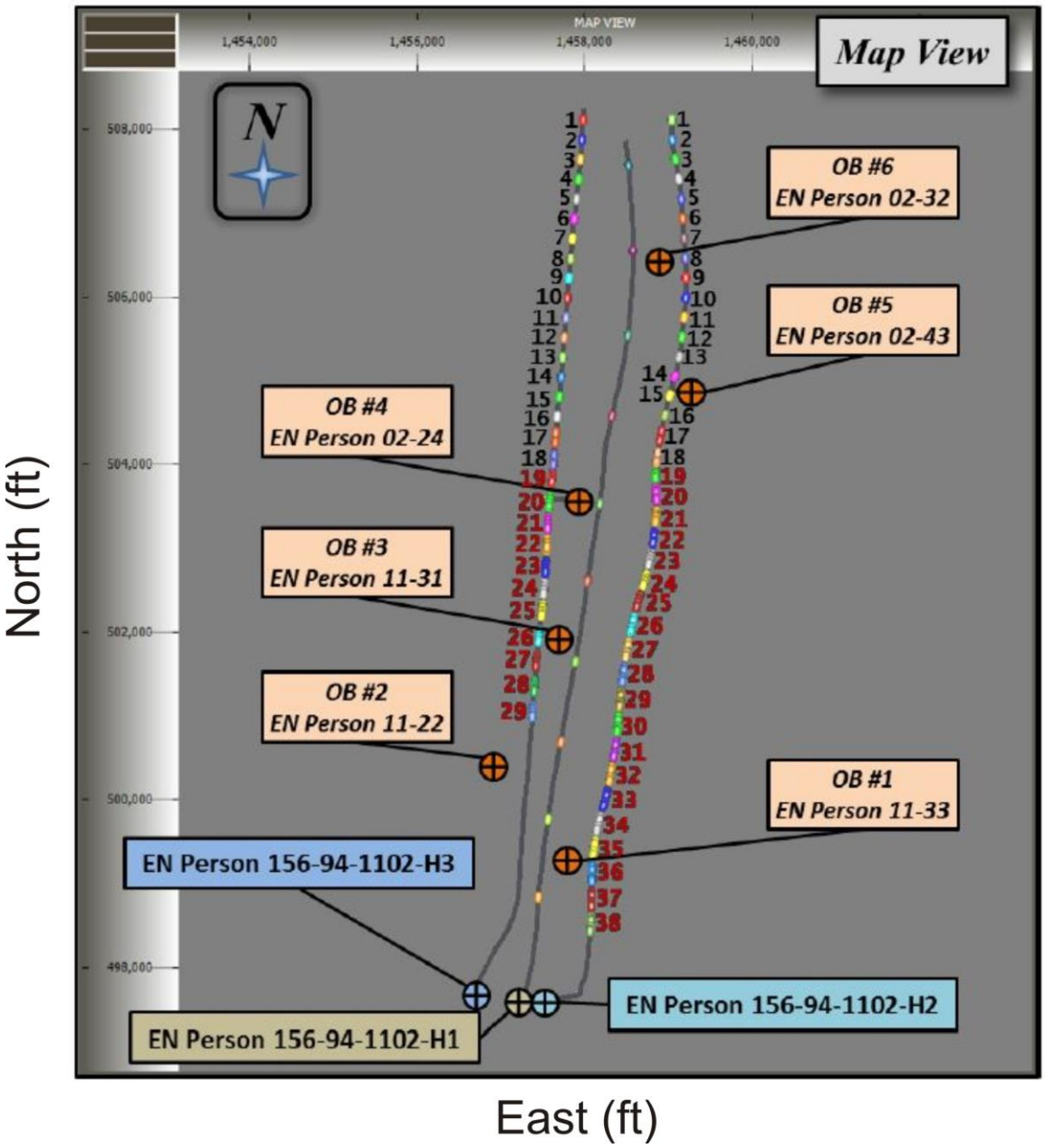

Figure 5.1: Map view of site showing the H3 and H2 treatment wells with the stages color-coded and numbered: the H1 (previously-completed, producing well); and the six observation wells, the EN Person 11-33, 11-22, 11-31, 02-24, 02-43, and 02-32. Stages labeled with black numbers used ball-actuated, sliding sleeves; Stage labeled with red numbers used pump-down plug-and-perforation guns. (Apex report)

5.2 Field data test

Considering limited computational power, only stages 22-23 of H2 well that began from October 13, 2011, 6:32 AM to October 13, 2011, 4:46 PM were considered in this test. As mentioned in Chapter 3, some events that occurred at or near the depth of the treatment wells showed no obvious S-wave splitting due to near vertical ray paths (Figure 3.12). We therefore ignored these types of events. For the events that occurred above the treatment wells, S-wave-splitting was robust and could be used to test this method. As seen in Figure 5.2, we found that at least half of these events do not show obvious P-wave arrivals, which is common for microseismic data. In this case, it was impossible to obtain the event azimuth from P wave data. Our method using S wave information is ideal for determining these event azimuths. Since the purpose in this chapter is to test the feasibility of our method using real data, these events were not considered because no further information can prove the reliability of obtained azimuths.

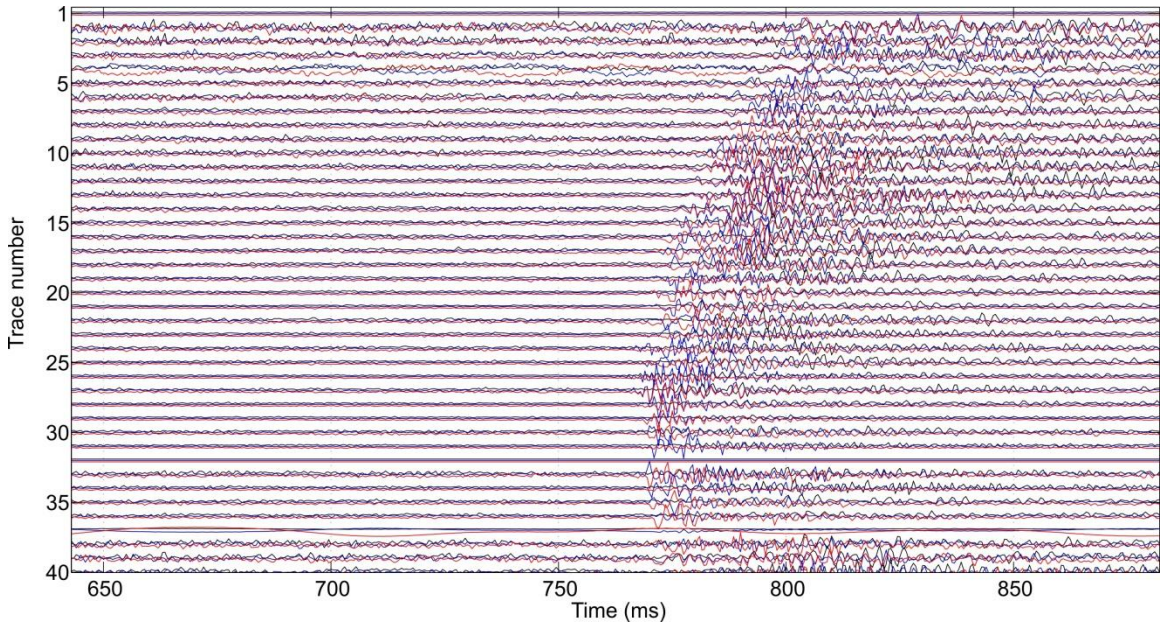

Figure 5.2: Waveforms recorded at well 3 from one microseismic event. Blue, black and red waveforms are for east, north and vertical components, respectively. No clear P-wave arrivals can be recognized.

Then we focused on events that are characterized by recognizable P-wave arrivals. It is unnecessary to process a large number of events for testing the method. 24 representative events were selected for this test. P-wave hodograms were conducted first to determine event azimuths (Table 5.1; Table 5.2). Theoretically, all receivers should give the same results for a given event if azimuthal anisotropy is ignored. The average of these results is used as the final determined event azimuth. 13 of the 24 events are considered reliable (group 1). They are characterized by a high SNR (>6) for P waves and a low standard deviation of determined azimuths (<10°) (Figure 5.3[a]). The remaining events are characterized by a low SNR (<4.5) for P waves and a high standard deviation of determined azimuths (>30°) and are considered unreliable (group 2) (Figure 5.3[b])

because the locations of these events must have large errors due to high uncertainty of event azimuths from P wave data.

Table 5.1: Events azimuths and their standard deviations of group 1. Azimuth is defined from east to north.

No.	Azimuth (°)	Standard Deviation (°)
1	63.6	9.6
2	60.4	6.6
3	61.5	7.2
4	63.2	5.2
5	55.0	2.5
6	63.8	4.5
7	61.1	7.2
8	58.5	3.9
9	52.2	6.8
10	62.3	3.6
11	61.5	1.5
12	57.8	3.4
13	64.1	2.9

Table 5.2: Events azimuths and their standard deviations of group 2. Azimuth is defined from east to north.

No.	Azimuth (°)	Standard Deviation (°)
1	63.6	34.1
2	64.4	33.3
3	70.3	37.5
4	56.2	41.4
5	56.8	41.7
6	54.0	31.1
7	60.1	38.6
8	53.5	30.1
9	69.8	31.4

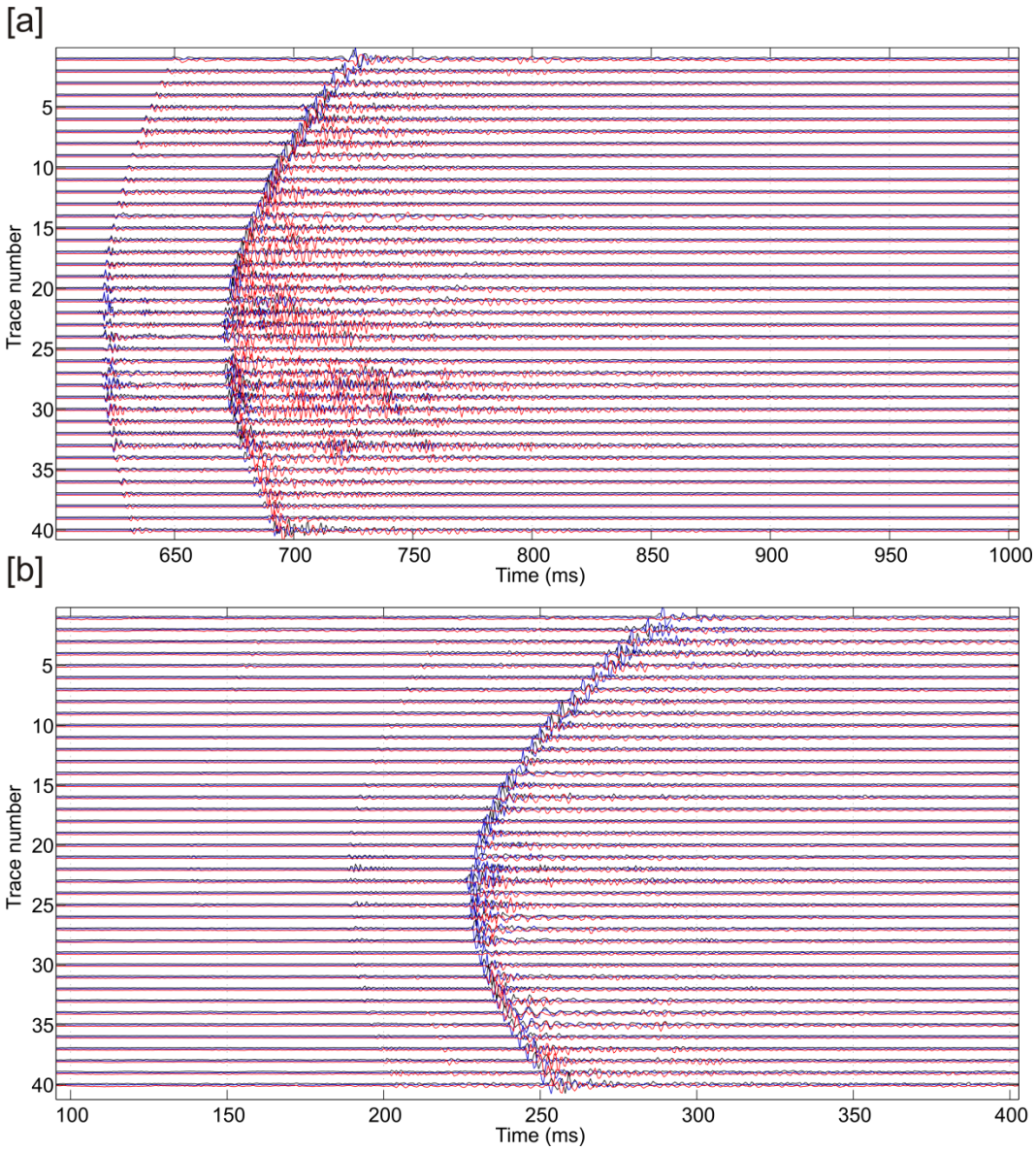

Figure 5.3: Waveforms of a reliable event that has clear P waves [a] and an unreliable event in which P-wave signals are extremely weak [b]. Blue, black and red waveforms are for east, north and vertical components, respectively.

Figure 5.4 shows hodogram analysis results of three receivers from event number 6 of group 1, the reliable events. As expected, P-wave particle motions are linear and align well with the propagation directions of the incident waves. The determined azimuths of all receivers yielded a standard deviation of 4.5°, indicating trustable measurement results for the microseismic events. Figure 5.5 shows examples of hodograms at three receivers derived from an event of unreliable events (group 2). Obviously, these particle motions show significant deviation from the linearity. The determined azimuths of all receivers yielded a standard deviation of 33°. The locations of unreliable events are questionable when using azimuths from P wave polarizations, because of the large uncertainties.

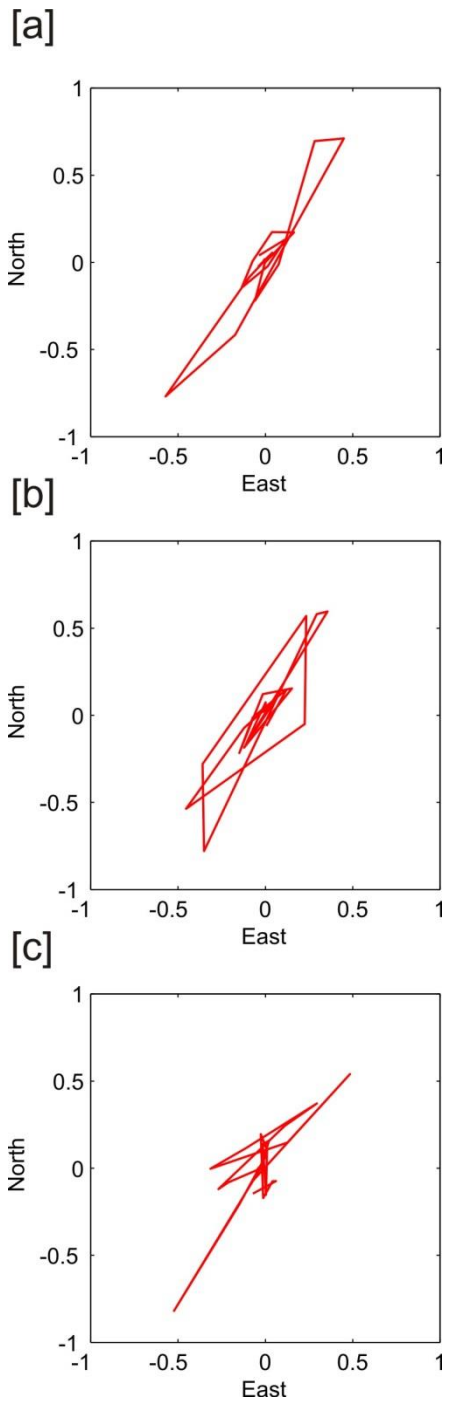

Figure 5.4: P-wave particle motions in map view of receiver 1 [a], receiver 2 [b], receiver 3 [c] of event 6 of reliable events.

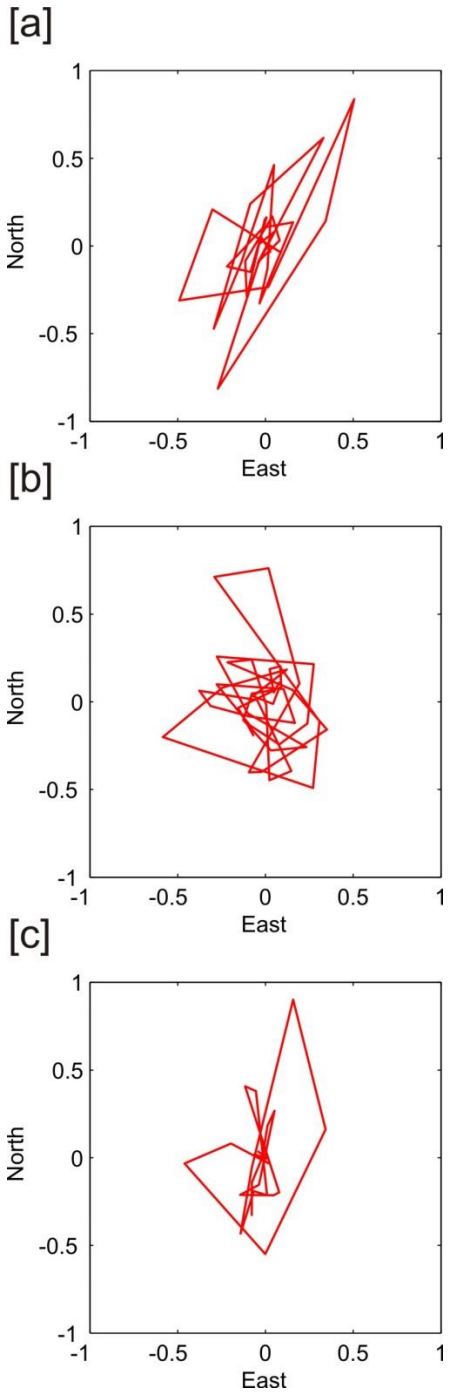

Figure 5.5: P-wave particle motions in map view of receiver 1 [a], receiver 2 [b], receiver 3 [c] of event 2 of unreliable events.

We then applied our method using S-wave splitting data to determine these event azimuths. P- and S-wave arrivals were picked (Figure 5.6) and used to locate the events in 2D by ignoring the azimuth. We used a VTI velocity model calibrated from perforation shots provided by a vendor (Figure 5.7). Inclinations of the incoming rays at each receiver were calculated based on the 2D location results (Table 5.3). For each event, only traces that present clear S-wave splitting were selected and windowed. We utilized these data to search the best event azimuth. The search range was chosen according to the pre-determined azimuth from P-wave hodogram with a search interval of 5°. These parameters were chosen in order to achieve a balance between efficiency and accuracy. Examples of the misfit distribution at different azimuths are displayed in Figure 5.8 for reliable and unreliable events. In both cases, the minimum misfit errors can be clearly separated from the neighboring azimuths.

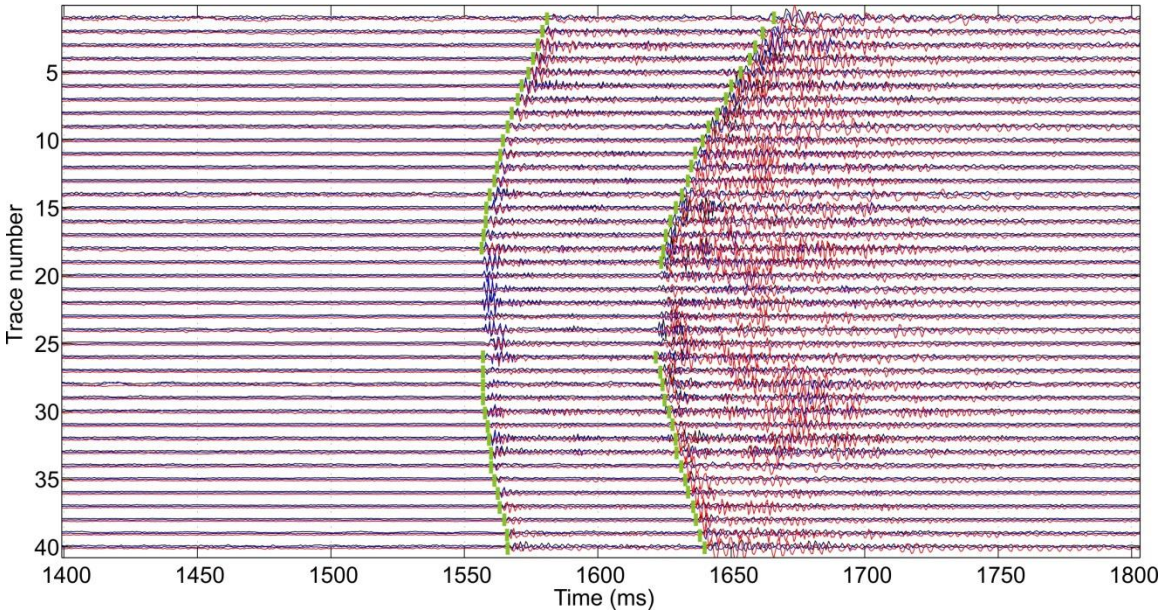

Figure 5.6: An example of arrival time picking (green bars) for 2D locating. Blue, black and red waveforms are for east, north and vertical components, respectively.

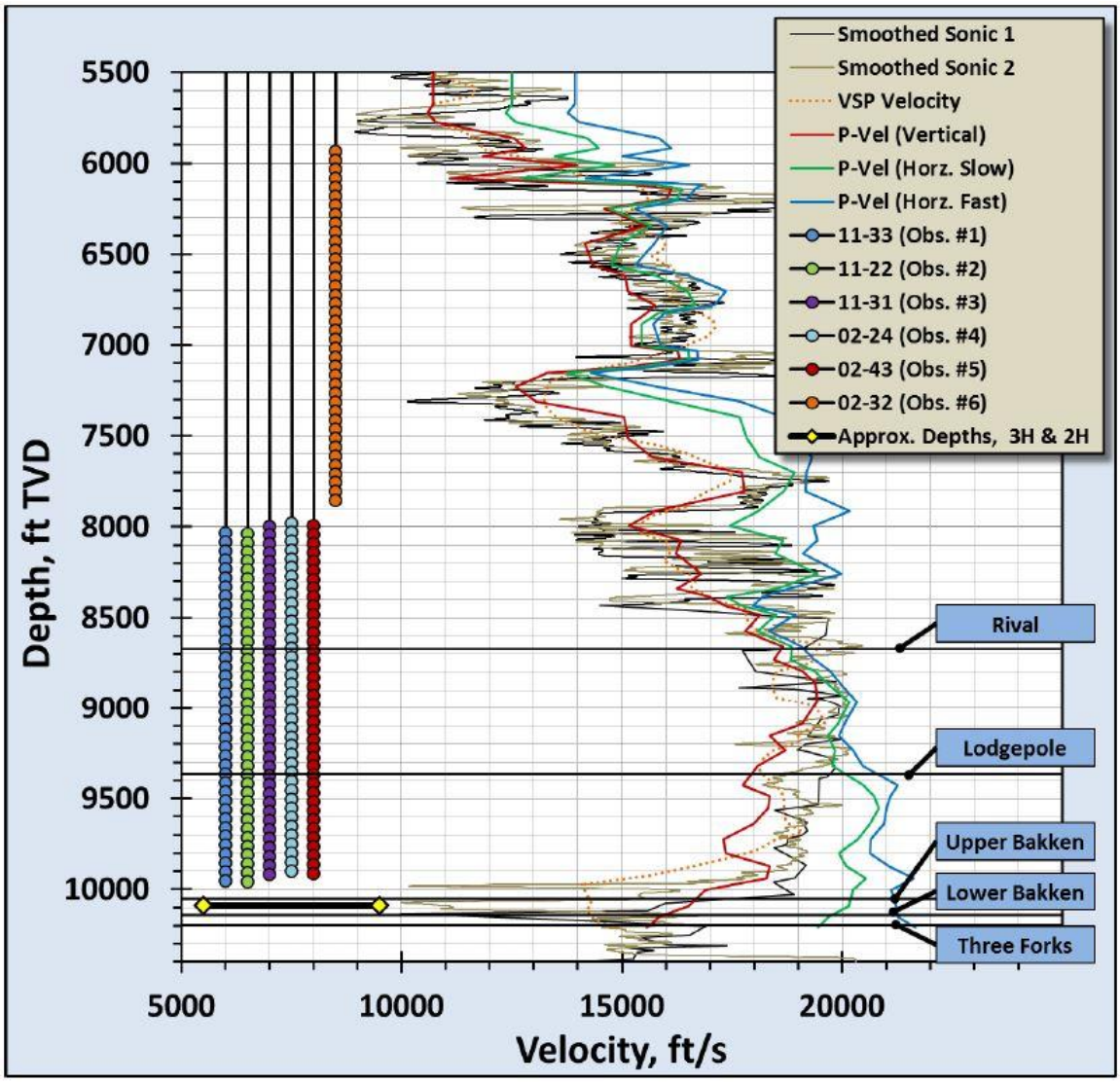

Figure 5.7: The VTI Velocity model used in this study for 2D locating (Apex report).

Table 5.3: Obtained inclinations of traces 6-16 after 2D locating from event 6 in group 1. Inclination is defined from the vertical direction to the horizontal plane.

Trace No.	Inclination (。)
6	60.6
7	61.9
8	63.3
9	64.7
10	66.2
11	67.7
12	69.2
13	70.8
14	72.3
15	74.0
16	75.6

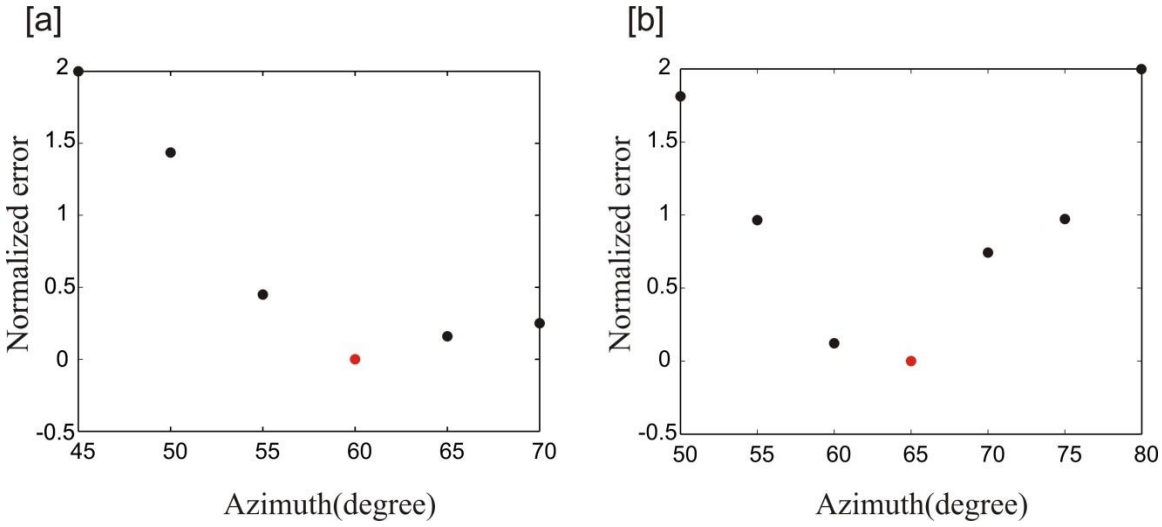

Figure 5.8: Examples of the distributions of normalized misfits for a reliable event [a] and an unreliable event [b]. Red dots mark the azimuth that gives the smallest misfit.

The results of event azimuths from the P-wave and S-wave methods are displayed in Figure 5.9. Azimuths for the events that are more precisely located from two monitoring wells using a method proposed in Chapter 2 are also plotted for comparison. For events with high SNRs, azimuths from S-wave-splitting data correlate well with those from P-wave polarizations and those from previous locations (Figure 5.9[a]). For events with low SNRs, the results from S-wave data show poor correlation with those from P-wave data but still largely agree with the azimuths determined using two monitoring wells (Figure 5.9[b]). These comparisons suggest that event azimuth from P-wave particle motion can be significantly biased by noise. In contrast, event azimuths determined from S-wave-splitting analysis are less sensitive to noise and more reliable.

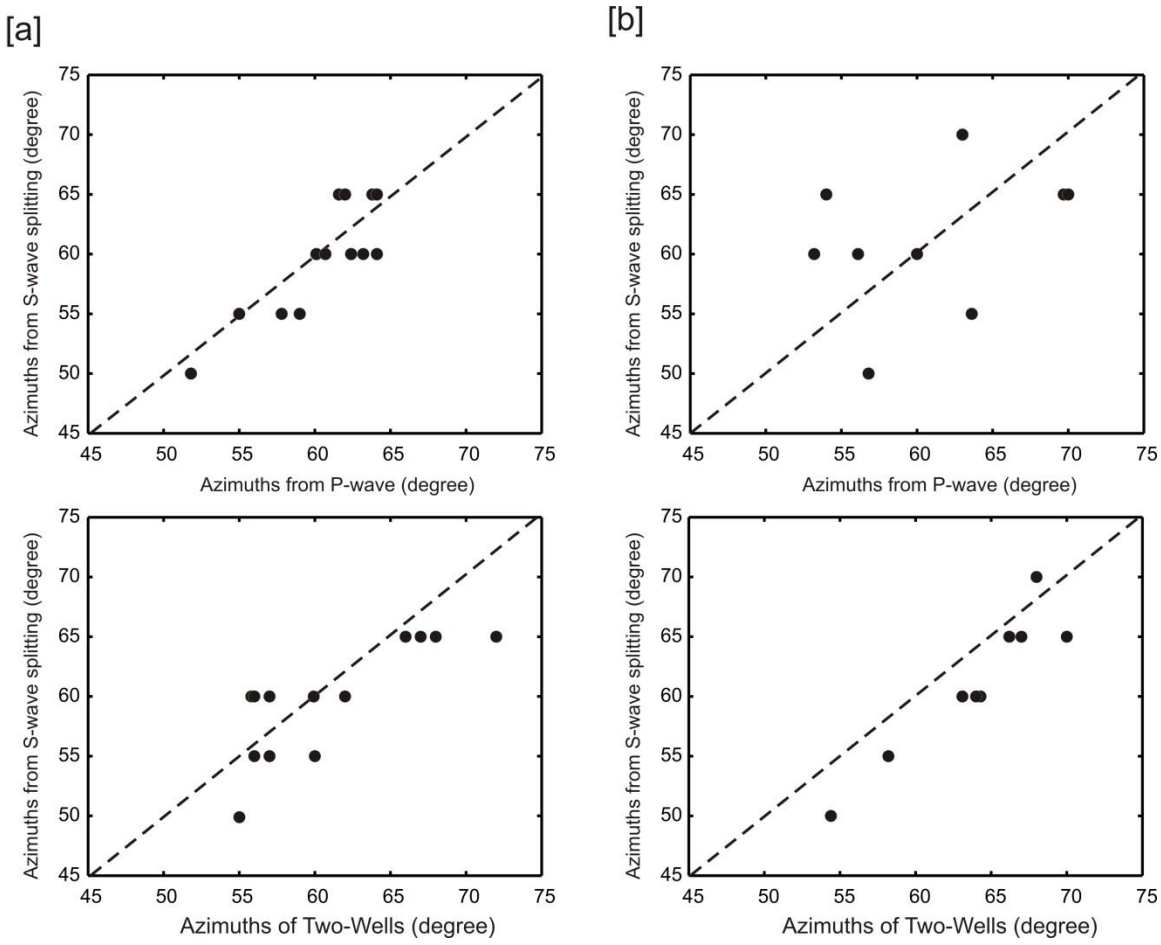

Figure 5.9: Comparison of event azimuths from S-wave splitting analysis with those from P-wave particle motions and with the results from two wells. [a] is for reliable events and [b] is for unreliable events. The dashed line indicates perfect correlation.

5.3 Discussion

Our field data test suggests that it is feasible to use S-wave splitting in microseismic data to determine event azimuths. Conventional azimuth determination methods that only rely on P-wave information require high-quality microseismic data, which cannot be satisfied in some datasets. The dataset we used in this chapter had a large number of events with no or very weak P-wave arrivals. Although these azimuths can still be obtained using P-wave hodograms, azimuths measured from all receivers of a certain event usually showed a very large standard deviation. In this case, the azimuths determined from our method agree well with those from the conventional P-wave method for high-SNR events. For low-SNR events, our method is superior to the P-wave method in matching the azimuths from more precise locations obtained from two monitoring wells.

The efficiency of our method depends on the searching range and interval of the azimuth. To increase the efficiency in data processing, reasonable Azi_{beg}, Azi_{end} and ΔAzi should be selected. We recommend narrowing the search range when a large amount of data need be considered. Such a narrow range can be achieved by pre-located events, the locations of perforation shots or from the poorly determined event azimuths using P-wave hodograms.

Although S-wave-splitting is abundant in this dataset, events occurred near or at the depths of treatment well H2 did not show any obvious S-wave splitting. This is the

biggest limitation of our method. It cannot be used when there is no S-wave splitting in the data.

5.4 Conclusion

We determined the azimuths of microseismic events from S-wave splitting in real microseismic data in the Bakken reservoir. The most important result is that the azimuths determined from our method agree with those from the conventional method when P-wave data have a good SNR and a low standard deviation. But when P-wave data are not in high quality, azimuths from the two methods have large difference. However, our method of S-wave is less sensitive to noise and can produce more reliable measurements for noisy data. One limitation of our method is the null measurements, when no splitting is detected in the data. However, only a few sensors or even one sensor that achieves a successful measurement enables the application of this method.

6 Chapter 6

Conclusion

The main goal of this dissertation is to develop new methods to improve the accuracy of microseismic event locations utilizing S-wave splitting measurements in microseismic data.

In microseismic imaging, it is essential to use the low symmetry anisotropic velocity model that is resulted from layered sediments and vertical natural and man-made fractures. The main obstacle of anisotropic velocity model building is the sparse ray coverage provided by downhole data. To address this challenge, we introduced a new method that utilizes S-wave splitting parameters, which are more sensitive to anisotropy velocity model parameters than common used P- and fast S-wave travel times. This method can be used to determine a medium with strong azimuth anisotropy, from which manually picking slow S-wave arrivals is difficult. The uncertainties of splitting measurements are calculated with the splitting parameters, which are critical in normalizing different data types in forming the objective function of the GA inversion. A joint inversion using both travel times and splitting parameters from two observation wells is presented for a low symmetry anisotropic velocity model and event locations. This method was tested using synthetic waveforms from numerical modeling in an effective homogeneous medium and heterogeneous media. The input locations and velocity models are successfully in both cases. We conclude that adding full S-wave-

splitting data significantly improve constraints on low symmetry anisotropic models from downhole microseismic data.

This joint inversion method was applied to real microseismic data in the Bakken shale. Only two observation wells and a limited number of events were included to simulate the situation of sparse ray coverage. The final located results get rid of the outliners of events that are present from an isotropic model, and the new locations become more linear and geological meaningful. We also obtained a near VTI effective model that is consistent e with the model from VSP analysis in the area. Our experiments have evidenced that adding S-wave splitting parameters makes significant improvement in constraining a low symmetry anisotropic model from downhole microseismic data.

For microseismic surveys using only one monitoring well, a common issue is poorly determined event azimuths, which produce errors on event locations. It is common that P waves have low SNRs in microseismic data, which are not good enough to obtain reliable event azimuths. To address this problem, we presented a new method of determining event azimuths using S-wave splitting in microseismic data. This method utilizes the relationship that the effectiveness of S-wave splitting measurements depends on the coordinate rotation for a given azimuth. We conducted two synthetic tests with different levels of noises. From the test of low noise data, we found that conventional P-wave polarization method produced large heavy uncertainties for event azimuths, while our method using S waves can estimate event azimuths with a much smaller error. This method also performs well for the high noise data, in which P-wave energy was

completely buried by noise and cannot be used. We recommend using this method when P-wave data are noisy or absent for one-well microseismic monitoring.

We also applied this method of determining event azimuths to a real dataset from the Bakken Formation. To simulate one well case, only data from one monitoring well were used. The selected events were divided into two groups, reliable events and unreliable events, based on their SNRs. The azimuths determined from our method agree well with those from the conventional P-wave method for high-SNR events. For low-SNR events, our method is superior to the P-wave method in matching the azimuths from more precise locations obtained from two monitoring wells.

REFERENCES

Bardainne, T., E. Gaucher, F. Cerda, F, and D. Drapeau, 2009, Comparison of picking-based and waveform-based location methods of microseismic events: Application to a fracturing job: 79th Annual International Meeting, SEG, Expanded Abstracts, 1547-1551.

Chambers, K., J.-M Kendall, and O. Barkved, 2010, Investigation of induced microseismicity at Valhall using the Life of Field Seismic array: The Leading Edge, **29**, 290-295.

Eisner, L., M. Thornton, and J. Griffin, 2011, Challenges of microseismic monitoring: SEG Technical Program Expanded Abstracts, 1519-1523.

Fuller, B., L. Engelbrecht, R. Van Dok, and M. Sterling, 2007, Diffraction processing of downhole passive monitoring data to image hydrofrcture location: 77th Annual International Meeting, SEG, Expanded Abstracts, 1297-1301.

Gajewski, D., K. Sommer, C. Vanelle, and R. Patzig, 2009, Influence of models on seismic-event localization: Geophysics, **74**(5), WB 55-WB61.

Gajewski, D., and E. Tessmer, 2005, Reverse modelling of seismic event characterization: Geophysical Journal International, **163**(1), 276-284.

Gambino, S.P., A. Mostaccio, D. Patane, L. Scarfi, and A. Ursino, 2004, High-precision locations of the microseismicity preceding the 2002-2003 Mt. Etna eruption: Geophysical Research Letters, **31**, L18604.

Geiger, L., 1912, Probability method for the determination of earthquake epicenters from the arrival time only: Bull. St. Louis University, **8**, 60–71.

Gharti, H.N., V. Oye, M. Roth and D. Kuhn, 2010, Automated microearthquake location using envelope stacking and robust global optimization, Geophysics, **75**, MA27-MA46.

Got, J.-L., and P.Okubo, 2003, New insights into Kilauea's volcano dynamics brought by large-scale relative relocation of microearthquakes: Journal of Geophysical Research, **108**, 2337-2349.

Grechka, V., 2015, Shear-wave group-velocity surfaces in low-symmetry anisotropic media: Geophysics, **80**(1), C1–C7.

Grechka, V., and S. Yaskevich, 2014, Azimuthal anisotropy in microseismic monitoring: A Bakken case study: Geophysics, **79**(1), KS1-KS12.

Grechka, V., and S. Yaskevich, 2013, Inversion of microseismic data for triclinic velocity models: Geophysical Prospecting, **61**, 1159-1170.

Grechka, V., P. Singh, and I. Das, 2011a, Estimation of effective anisotropy simultaneously with locations of microseismic events: Geophysics, **76**(6), WC141-WC153.

Grechka, V., and A. A. Duchkov, 2011b, Narrow-angle representations of the phase and group velocities and their applications in anisotropic velocity-model building for microseismic monitoring: Geophysics, **76**(6), WC125-WC140.

Haldorsen, J.B.U., N.J. Brooks, and M. Milenkovic, 2013, Locating microseismic sources using migration-based deconvolution, Geophysics, **78**(5), KS73-KS84.

Harrison, P., 1992, Processing of P-SV Surface-Seismic Data: Anisotropy Analysis, Dip Moveout, and Migration: PH.D Dissertation of University of Calgary.

Huang, H., 2016, Estimating seismic anisotropy: fluid substitution theory, 3D-printed inclusion models, and Multi-component 3D VSP in the Bakken Shale: PH.D Dissertation of University of Houston.

Jansky, J., V. Plicka, and L. Eisner, 2010, Feasibility of joint 1D velocity model and event location inversion by the neighborhood algorithm: Geophysical Prospecting, **58**, 229-234.

Juan, I. S., and D.R. Velis, 2013, A robust method for microseismic event detection based on automatic phase pickers: Journal of Applied Geophysics, **99**, 42-50.

Kim, W., and C. E. Baag, 2002, Rapid and accurate two-point ray tracing based on a quadratic equation of takeoff angle in layered media with constant or linearly varying velocity function: Bulletin of Seismological Society of American, **92**, 2251-2263.

Li, A., and C. Chen, 2006, Shear wave splitting beneath the central Tien Shan and tectonic implications: Geophysical Research Letters, **33**, L22303.

Li, A., and R. Detrick, 2003, Azimuthal anisotropy and phase velocity beneath Iceland: implication for plume-ridge interaction: Earth and Planetary Science Letters, **214**, 153-165.

Li, J., C. Li, S.A. Morton, T. Dohmen, K. Katahara, and M.N. Toksoz, 2014, Microseismic joint location and anisotropic velocity inversion for hydraulic fracturing in a tight Bakken reservoir: Geophysics, **79**(5), C111-C122.

Hung, S.-H., and D.W. Forsyth, Modeling anisotropic wave propagation in oceanic inhomogeneous structures using the parallel multidomain pseudo-spectral method, 1998, Geophysical Journal International, **133**, 726-740.

Li, J., H. Zhang, W.J. Rodi, and M.N. Toksoz, 2013, Joint microseismic location and anisotropic tomography using differential arrival times and differential backazimuths: Geophysical Journal International, **195,** 1917-1931.

Maxwell, S.C., 2012, Comparative microseismic interpretation of hydraulic fractures: Canadian Unconventional Resources Conference, SPE 162782.

Maxwell, S. C., L. Bennett, M. Jones, and J. Walsh, 2010, Anisotropic velocity modeling for microseismic processing: Part 1 – Impact of velocity model uncertainty: 80th Annual International Meeting, SEG Expanded Abstracts, 2130-2134.

Padhi, A., and S. Mallick, 2013, Accurate estimation of density from the inversion of multicomponent prestack seismic waveform data using a nondominated sorting genetic algorithm,: The Leading Edge, **32**(1), 94-98.

Pei, D., J.A. Quirein, B.E. Cornish, D. Quinn and N.R. Warpinski, 2009, Velocity calibration for microseismic monitoring: A very fast simulated annealing (VFSA) approach for joint-objective optimization: Geophysics, **74**, WCB47-WCB55.

Plešinger, A., M. Hellweg and D. Seidl, 1986, Interactive high-resolution polarization analysis of broadband seismograms: J. Geophysics, **59**, 129-139.

Sharma, M. D, 2002, Group velocity along general direction in a general anisotropic medium: International Journal of Solids and Structures, **39**, 3277-3288.

Silver, P.G., and W.W. Chan, 1991, Shear wave splitting and subcontinental mantle deformation: Journal of Geophysical Research, **96**(B10), 429-454.

Teanby, N.A., J.-M Kendall and M. Van Der Baan, 2004, Automation of shear-wave splitting measurement using cluster analysis: Bulletin of the Seismological Society of America, **94**, 453-463.

Thomsen, L., 1986, Weak elastic anisotropy: Geophysics, **51**, 1954–1966.

Thurber, C. H., and W. L. Ellsworth, 1980, Rapid solution of ray tracing problem in heterogeneous medium: Bulletin of the Seismological Society of American, **70**, 1137-1148.

Tsvankin, I., and V. Grechka, 2011, Seismology of azimuthally anisotropic media and seismic fracture characterization: SEG Geophysical Reference Series, no. 17.

Verdon, J.P., and J.-M. Kendall, 2011, Detection of multiple fracture sets using observations of shear-wave splitting in microseismic data, Geophysical Prospecting, **59**, 593-608

Verdon, J.P., J.-M. Kendall, and A.Wustefeld, 2009, Imaging fractures and sedimentary fabrics using shear-wave splitting measurements made on passive seismic data: Geophysical Journal International, **179**, 1245-1254.

Vernik, L., and X.Liu, 1997, Velocity anisotropy in shales: A petrophysical study: Geophysics, **62**, 521-532.

Warpinski, N.R., R.B. Sullivan, J.E. Uhl, C.K. Waltman, and S.R. Machovoe, 2005, Improved microseismic fracture mapping using perforation timing measurements for velocity calibration: The Society of Petroleum Engineers Journal, **10**, 14-23.

Waldhauser, F., 2001, HypoDD: A computer program to compute double-difference earthquake location: U.S. Geological Survey, Open-file report 01-113.

Waldhauser, F., and W. L. Ellsworth, 2000, A double-difference earthquake location algorithm: Method and Application to the North Hayward Fault, California: Bulletin of Seismological Society of America, **90**(6), 1353-1368.

Meissner, F.F., 1991, Petroleum geology of the Bakken Formation Williston Basin, North Dakota, and Montana: Presented at Montana Geological Society 24th Annual Conference.

Method and application to the Northern Hayward fault, California: Bulletin of the Seismological Society of America, **90**, 353–1368.

Wesson, R.L., 1971, Travel-time inversion of laterally inhomogeneous crustal velocity model: Bulletin of the Seismological Society of America, **61**, 729-746.

Wuestefeld, A., O. Al-Harrasi, J.P. Verdon, J. Wookey, and J.-M. Kendall, 2010, A strategy for automated analysis of passive microseismic data to image seismic anisotropy and fracture characteristics: Geophysical Prospecting, **58**(5), 755-773.

Yang, Y., and M. D. Zoback, 2014, The role of preexisting fractures and faults during multistage hydraulic fracturing in the Bakken Formation: Interpretation, **2**(3)**,** SG25-SG39.

Fu, Y., Li. A, I. Garrett, and S.-H. Hung, 2012, Waveform modeling of shear wave splitting from anisotropic models in Iceland: Geochemistry, Geophysics, Geosystems, **13**, Q12001.

Zhang, H., S. Sarkar, M.N. Toksoz, H.S. Kuuleli, and F. Al-Kindy, 2009, Passive seismic tomography using induced seismicity at a petroleum field in Oman: Geophysics, **74**(6), WCB57-WCB69.

Zhou, R.L., L. Huang, and J. Rutledge, 2010, Microseismic event location for monitoring CO_2 injection using double-difference tomography: The Leading Edge, **29**, 208-214.